DISS. ETH NO. 23925

Multilayered Oxide Memristive Devices: Interaction of Strain, Interfaces and Electric Transport

A thesis submitted to attain the degree of
DOCTOR OF SCIENCES of ETH ZURICH
(Dr. sc. ETH Zurich)

presented by
SEBASTIAN SCHWEIGER
MSc in Technical Chemistry, Technische Universität Graz
born on 28th of June1986
citizen of Austria

Accepted on the recommendation of:
Prof. Dr. Jennifer L.M. Rupp, examiner
Prof. Dr. Jürgen Janek, co-examiner
Prof. Dr. Thomas Lippert, co-examiner
Prof. Dr. Pietro Gambardella, co-examiner

Zurich, 2016

Acknowledgements

I would like to thank Prof. Jennifer L.M. Rupp for giving me the opportunity to conduct the research project leading to this PhD thesis under her supervision. She provided tremendous support, always had great ideas to advance the research and also helped me to learn a lot for my professional life.

I want to thank Prof. Manfred Fiebig from ETH Zurich, Prof. Pietro Gambardella from ETH Zurich, Prof. Jürgen Janek from the University of Giessen and Prof. Thomas Lippert from the Paul Scherrer Institute for the careful examination of this thesis.

Many thanks go to the Electrochemical Materials Team, not only for interesting discussions and scientific support and input, but also for offering their friendship and enjoying many nice hours together. Felix Messerschmitt is thanked for being the best officemate conceivable. Particular thanks go to William Bowman for his support with TEM imaging and analysis and Yanuo Shi for the support with FIB and optical profilometry. Reto Pfenninger is to be particularly mentioned for helping me with the purchase of the Raman microscopy system. Josephine Baer is thanked for her swift and comprehensive support with administrative issues.

Also I would like to thank my students Thomas Geldmacher, Christoph Murer, Reto Pfenninger, Maximilian Jansen and Andre Schmidt for their invaluable contributions to this thesis.

I am also very grateful to my collaborators, Prof. Ulrich Aschauer, Prof. Christoph Müller, Prof. Peter Crozier, Dr. Markus Kubicek, Dr. Qasim Imtiaz, Dr. Nan Yang, Alexander Bork and Peter Kocher. Also, I wanted to thank Kirstin Casdorff and Jana Segmehl for the joint organization of the Raman microscopy workshop. Assistance by the FIRST cleanroom, the D-MATL mechanical workshop and SCOPE-M staff is kindly acknowledged. Dr. M. Süess is thanked for fruitful discussions. Prof. R. Spolenak is thanked for use of the Raman microscopy facility and Prof. R. Nesper and Dr. M. Wörle for using the XRD instrument.

Acknowledgements

Zachary Lapin is thanked for proofreading this thesis, scientific discussions and his friendship. My friends and family, and particularly my beloved wife Nicole, are highly thanked for their love and support.

Summary

In the last decade, *oxide-based memristive devices* have emerged as a high-potential memory technology for computations beyond the binary era. They offer to become a prominent exponent of storage-class memories that combines the fast response of memories such as DRAM while also being non-volatile and integrable into high-density storage applications, and with reasonable economics. Ultimately, memristive devices store information through various addressable resistance states and are switched under high electric fields with voltage pulses at the ns-scale. Usually memristive devices consist of a metal-oxide-metal sandwich structure and considerable efforts are underway to vary microstructural features that alter the oxide and device response.

Replacing the switching oxide layer with structured materials offers many exciting new possibilities for tailoring the resistive properties of memristive memories. Over the last years, interface engineering has been used to deliberately impose strain through lattice mismatched layers. While this technology is still in its infancy, it offers exciting new possibilities for tailoring device properties

Specifically, it is still unclear how strain acts on ionic and mixed ionic/electronic conducting oxides at ambient conditions under high local electric field strength. In this thesis a new idea is presented for the first time which is the concept of making a strained memristive heterostructure device based on solid state ion conducting oxides is presented for the first time. The hypothesis is that strain at oxide interfaces in engineered multilayer structures can be used to alter mixed ionic-electronic properties at a much larger scale than classic solid solution doping approaches. Ultimately, the hypothesis is tested and the first strained memristive ionic-electronic devices based on heterostructure oxides are demonstrated.

Part I, the *General Introduction*, introduces the basics of the memristive effect and how memristive devices work.

The underlying principles of lattice mismatch induced interfacial strain are discussed in the context of its application for modulating ionic and electronic charge transport in oxide film multilayers. At the end, materials properties and defect chemical aspects are discussed for the envisioned material structures, their fabrication and integration into novel strained memristor prototype devices. Challenges, risks and the future potential are carefully concluded.

Part II is devoted to obtaining a basic understanding of the multilayered material system $Gd_{0.1}Ce_{0.9}O_{2-\delta}/Er_2O_3$. The system is designed to display compressive strain in the ionic conductor along the charge carrier flow direction. A new microfabrication route had to be developed to achieve this device type, so-called microdots. Contacting strategies were reviewed and a suitable contacting strategy was established for this type of device. This was a prerequisite as heterostructures are traditionally measured with top contacts or side-pasted contacts which bear the risk that not all strained oxide heterolayer interfaces are effectively measured. Importantly, it formed the base for making the first strained multilayer memristors in the following chapters; the sideways contacting at a low electrode distance, as presented here, is needed later to efficiently operate the device at high electric field strengths.

Part III makes and tests the strained memristive oxide heterostructure devices for the very first time. One emphasis of the chapter is to explore technically how to use "Raman mapping" to probe for strained heterolayer oxide structure near order changes in the ionic bonding in integrated device structures. We modulate the monolayers down to nm scale and systematically show how the anisotropy increases in the cubic heterolayer fast conductor by spectroscopic vibrational changes, DFT computation and HR-TEM. The fundamental understanding gained here forms the basis to show a systematic tuning of the strain state at the fast ion conductor phase ceria of the multilayer oxide building block. This allows us to modify the strain-modulated memristive response in the strained memristors. This work presents a new concept to alter the current-voltage profiles in the first strained memristor devices and may be further

explored for commercial integration and miniaturization in follow-up work.

Part IV addresses the question formed by a simple observation made in this study: Why do totally symmetrically aligned memristive oxide devices, in terms of their electrodes and switching oxide, show asymmetric hysteretic curves in their current-voltage profiles?

For this, memristive devices with symmetrically aligned electrodes are made. Importantly, through electroforming at different polarities, we introduce an artificial "electrochemical" symmetry break in the current-voltage profiles and in the charge carrier distribution profiles. This allows us to study the influence of asymmetry induced by bias on the memristive response and to look closer at the electrochemical response and defect chemistry. This differs substantially to classic resistive switching set-ups in cross-plane geometries where *e.g.* atmosphere access and defects are by design different for the electrode/air and electrode/substrate film interfaces; only by creating the experimental scenario using sideways-contacted microdots sufficiently high electric field strength could be realized to operate switching in-plane to study solely the impact of electroforming on switching. We confirmed that electroforming at different polarities results in current-voltage profiles exactly mirrored at zero volts. This is an important finding which implicates future oxide and contacting designs for memristors on bit and multi-bit structures for application memories and non-binary computing applications for neuromorphics.

Finally, *Part V*, gives a general conclusion of this thesis, reflects on discussions in the field based on the published work and gives a perspective for a future continuation of the work for research and application.

Zusammenfassung

Im letzten Jahrzehnt haben sich Oxid-basierte memristive Elemente als neu aufkommende Alternative mit grossem Potential für zuükünftige digitale Speichertechnologien etabliert. Sie kombinieren die Vorteile von schnellen Arbeits- und zurzeit relativ langsamen Massenspeichern und sind gleichzeitig kostengünstig herzustellen. Memristive Elemente speichern Information als verschiedene Widerstandszustände und werden unter hohen elektrischen Feldern mittel ns-Spannungspulsen zwischen den verschiedenen Zuständen geschaltet. Memristive Elemente bestehen üblicherweise aus einer Metall-Oxid-Metall Struktur. Es gibt grosse Bemühungen durch Änderung der Mikrostruktur die Eigenschaften des Materials und des Speicherelements zu verbessern.

Die Strukturierung des Oxids bietet viele Möglichkeiten zur Optimierung der Materialkomponenten der memristiven Speicher. In den letzten Jahren hat die Kontrolle von Grenzflächeneigenschaften durch Einbringung von Gitterfehlanpassungen zunehmend an Aufmerksamkeit gewonnen um Verspannungen in den Materialien einzuführen. Obgleich diese Technologie noch in den Kinderschuhen steckt, hat sie grosses Potential um Materialeigenschaften für verschiedene Anwendungen masszuschneidern. Die genaue Auswirkung von Verspannungen auf die ionische und gemischt ionisch-elektronische Leitfähigkeit in Oxiden unter hohen elektrischen Feldstärken bei Raumtemperatur ist bis jetzt unklar.

In dieser Dissertation wird das neue Konzept eines resistiven Speichers mit verspannten ionenleitenden Festkörpern erstmals vorgestellt. Dabei wird der Effekt genutzt, dass bei niedrigen Temperaturen fehlpassungsinduzierte Gitterverspannungen an Grenzflächen die grösste Auswirkung auf die Modulation der elektrischen Leitfähigkeit haben. Aus diesem Grund ist dies ein besonders vielversprechender neuer Ansatz für innovative funktionale Speicherbauteile, welche bei Raumtemperatur oder leicht erhöhten Temperaturen zum Einsatz kommen. Das Ziel dieser Arbeit besteht darin, erstmals verspannte Bauteile in einem Oxid-Multilagen Design zu entwickeln, ihre strukturbedingten

Transporteigenschaften zu erforschen, und deren Funktionalität als neuen Typ von memristiven Speichern erfolgreich zu demonstrieren.

Teil I, die Einleitung, behandelt die Grundlagen des memristiven Effekts sowie memristiver Speicherelemente und ihrer Anwendung. Ferner werden die grundlegenden Basiskonzepte für verspannte Oxidfunktionsbausteine als aktive Elemente neuartiger memristiver Speicher erläutert. Die wesentlichen Aspekte von fehlpassungsinduzierten Gitterverspannungen und deren Verwendung zur Modulation des Ladungsträgertransports in Multilagen-basierten Oxidschichten werden diskutiert. Es werden ausserdem die Auswahl der Materialien, deren Defektchemie und Herstellung für die Idee der neuen verspannten Speicherelemente behandelt.

Teil II ist dem grundlegenden Verständnis des Multilagen-Materialsystems $Gd_{0.1}Ce_{0.9}O_{2-\delta}/Er_2O_3$ gewidmet. Bei Verwendung dieses Materialpaars entsteht entlang des Ladungsträgerflusses eine kompressive Verspannung im Ionenleiter, dem Ceroxid. Eine neue Mikrofabrikationsroute wurde entwickelt um so-genannte Mikropunkte herzustellen welche als integrale Bestandteile charakterisiert werden, und in den weiteren Kapiteln dieser Arbeit als aktive Speicherschaltelemente dienen werden. Hierzu wurden verschiedene Kontaktierungsstrategien geprüft und anschliessend eine neue geeignete Art zur Kontaktierung von Mikropunkten mit Multilagenkomponenten entwickelt. Dies war eine Voraussetzung um den Ladungstransport an den nanoskopischen Grenzflächen der verspannten Multilagen zu messen. Zudem konnten erst durch diesen neuen Entwicklungsschritt verspannte memristive Elemente hergestellt werden, da diese, um als memristiver Speicher bei gleichzeitiger lateraler Elektrodenanordnung betrieben werden zu können, grosse elektrische Feldstärken benötigen. Die Kontaktierung über Seitenflächen ist hierbei wichtig um die verspannten Elemente später effizient als Speicher betreiben zu können.

Teil III zeigt die erstmalige erfolgreiche Fabrikation und anschliessende Charakterisierung von verspannten memristiven Oxidelementen als neue memristive Speicher. Die einzelnen Schichten der Multilagen werden bis auf einige nm in ihrer Dicke verkleinert. Durch hochauflösende

Transmissionselektronenmikroskopid und Raman-Mikroskopie wird gezeigt, wie sich die Anisotropie und der Verspannungsgrad in den Kristallgittern der Multilagenphasen entwickeln. Bildgebende Raman-Rasterung wird hier verwendet um die Speicherelemente auf ihre chemische Zusammensetzung zu untersuchen und kleinste Veränderungen im Spannungsgrad der Multilagenkomponenten zu detektieren. Die Raman Daten werden mittels DFT Berechnungen ausgewertet. Diese gewonnenen Ergebnisse bilden den Grundstein für eine systematische Modulation der Verspannungen der ionenleitenden Ceroxid Phase für die Gestaltung von verschiedenen verspannten Speicherelementen. Durch diesen neuen Ansatz können die memristiven Eigenschaften der Speicherelemente relativ zum Verspannungsrad der Oxidmultilagen bestimmt werden. Es wird ein erfolgreiches Konzept zur kontrollierten Modulation der memristiven Strom-Spannungs-Kennlinien über den initial eingebrachten Verspannungsgrad vorgestellt, das zur weiteren Miniaturisierung und kommerziellen Verwendung weiterentwickelt werden könnte.

Teil IV behandelt eine Frage die durch eine Beobachtung im Rahmen dieser Arbeit aufkam: Warum zeigen symmetrische Speicherelemente asymmetrische hysteretische Strom-Spannungs-Kennlinien?

Um dieser Frage nachzugehen, wurden memristive Speicherelemente hergestellt, welche symmetrisch in Bezug auf die Anordnung ihrer Elektroden, der Oxid-Mikrostruktur sowie der Austauschreaktionen mit der Atmosphäre sind. Anschliessend wird durch Elektroformierung bei verschieden angelegten Polaritäten ein künstlicher „elektrochemischer" Symmetriebruch in der Defektverteilung erzeugt. So können die Auswirkungen von Asymmetrie auf die memristive Antwort untersucht werden. Dies unterscheidet sich gravierend von klassischen resistiven Schaltern in vertikaler Geometrie, zum Beispiel in Bezug auf die Interaktion mit der Atmosphäre oder in unterschiedlichen Defektcharakteristika an den Grenzflächen der oberen und unteren Elektrode. Nur durch eine horizontale Probengeometrie, unter Verwendung von seitlich angebrachten Elektroden, können ausreichende elektrische Feldstärken erreicht werden um den Einfluss von

verschiedenen Elektroformierungsstrategien auf das resistive Schalten zu untersuchen.

In diesem Teil kann durch Elektroformierung bei unterschiedlichen Polaritäten die Spiegelung der Strom-Spannungs-Kennlinie bei null Volt bewiesen werden. Diese Erkenntnisse können zur Verbesserung zukünftiger oxidbasierter Speicherelemente beitragen, unter anderem für nicht-binäres Rechnen und neuromorphe Anwendungen.

Teil V diskutiert die gewonnen Erkenntnisse dieser Arbeit und reflektiert die Implikationen der hier vorgestellten Ergebnisse auf die Literatur. Schliesslich werden Anregungen für zukünftige Forschung und Entwicklung der in dieser Dissertation vorgestellten Grundlagen-Ergebnisse, sowie für die neuen verspannten memristiven Speicherelemente gegeben.

Table of Contents

PART I
General Introduction

Contents of this thesis chapter are to-be-submitted partially as an invited book Chapter 4.3 entitled as
Future Emerging Technologies based on MetOx Interfaces: MeO-Strain Interface Memristors
in the book
Metal Oxide-based Thin Film Structures: Formation, Characterization and Application of Interface-based Phenomena
by Sebastian Schweiger and Jennifer L.M. Rupp
edited by Nini Pryds for Elsevier Science & Technology Books, 2017.

Together with additional material parts of this chapter are in preparation as a focus review paper entitled
Engineering Strain for Future Multilayer Architectures in new Resistive Switching Memory and Computing Devices – A review
by Sebastian Schweiger, William J. Bowman, Peter Crozier and Jennifer L.M. Rupp to ACS Nano, 2016.

1   Memristive Devices: Status and Challenges

Modern societies face an increased demand of computational power accompanied by a call for energy efficiency[1,2]. This demand for faster computers with more functionality is leveraged by the increasing digitalization of our daily lives. Many aspects of modern life are controlled by computers and mobile devices have gained enormous popularity and functionality. Over the last years and decades, many new possibilities for science[3], industry[4], public administration[5] and communication[6] have been enabled by this increase in computer performance. In the future, applications such as large-scale simulations, internet of things or e-government will improve our quality of life but will also continue to drive the demand for more and faster computing with additional functionalities that are not possible with binary computing.

Until now, one could rely on a yearly increase of computer performance based on device scaling. This is called Moore's law and it states that every two years the number of transistors per area doubles[7,8]; therefore, also the performance rises considerably because the component density per chip area will increase. Another consequence of Moore's law is the significant trend to decrease the cost-per-function with increasing transistor density, supporting the proliferation of consumer and industrial electronics and other digital devices.

However, the semiconductor industry is approaching the limits of traditional semiconductor technology and this imposes several challenges. On one hand, the physical limits of device miniaturization are reached. Current fabrication technologies, like photolithography, are exhausted and at near-atomic dimensions further scaling is impossible[9] not to mention that detrimental quantum effects start playing a role[10]. On the other hand, the capital costs for research and development, as well as fabrication, increase exponentially and further downscaling becomes economically unfeasible. Here, new ways of further improving the computational power are needed.

Another major issue that the microelectronics industry is facing is the need to decrease power consumption. This is important for both large

scale computing operations, such as data centers, that use unsustainably large amounts of power and mobile consumer electronics, that need to conserve battery power. Also, high power consumption leads to a large heat dissipation, which limits the parallel use of components, meaning that large parts of a chip remain unused. This phenomenon is called dark silicon and is a major thermal design constraint in modern semiconductor applications[11-13]. New and innovative approaches and unconventional thinking are required to tackle these challenges[14,15].

To meet the demands for digital applications, one approach focuses on new design geometries, *e.g.* vertical 3D stacking, which will increase the number of components per square unit. But so far, all these devices are conventional and based on binary logic states. Another vision is to utilize more states in computing than 2, which can be utilized within in multi-state computing or quantum computing. One approach proposed by the semiconductor industry is called "More than Moore", which describes the incorporation of added, also non-digital, functionalities. This diversification enables devices that provide additional value, but do not necessarily scale according to Moore's law, *e.g.* sensors, actuators or passive components.

A third concept is to introduce new devices, that will allow a transition away from conventional CMOS to so-called "beyond CMOS" technologies. Very promising new types of devices that emerged recently are memristive nanodevices, also called memristors or resistive switches. The vision of using devices based on the modulation of resistance as computer memories was already discussed in the 1960s[16], but the concept only got considerable attention as the device was connected to the mathematical concept of the fourth circuit element[17,18] that was already described in theory in the early 1970s[19]. One of the prerequisites that enabled the technology of memristive devices was the progress in thin film technology that allowed reaching sufficiently high electric field strengths at moderate biases (potential per length unit)[20-22], which is of paramount importance for this device class. Due to these technological prerequisites that were established, a major increase in research activities

was observable and also industry started to consider memristive devices as an emerging technology.

Memristive devices are based on an electric insulator sandwiched between two electrodes, see Figure 1.1a. If such devices are subject to a sufficiently high electric field, they display a hysteretic current-voltage profile, see Figure 1.1b. This phenomenon of a voltage-history depended resistance to modify the hysteresis of a current-voltage profile is called "resistive switching" or "memristance". Two different resistance states can be defined as OFF (binary 0) or ON (binary 1) and these states can be used to store digital information. When a certain threshold voltage, called V_{set}, is exceeded, the device changes its resistance state. When a voltage of opposite polarity is applied, called V_{reset}, the device is set back to its initial state. The read process is carried out at a lower voltage to avoid any change of the resistance state of the device. When different polarities are necessary to change the resistance state, it is called bipolar switching. There are also so-called unipolar switches, where the set voltage is higher than the reset voltage and the reset current is higher than the current compliance (current limit) during the set process, *i.e.* only one polarity is needed to operate the device.
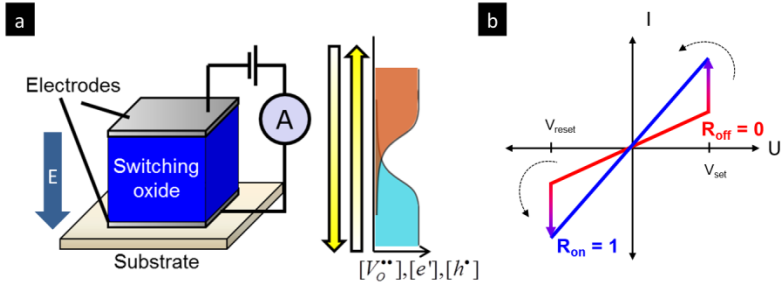
Figure 1.1: Basic concepts of memristive devices a) Metal-insulator-metal sandwich structure of a memristive device. The distribution and concentration of charge carriers such as oxygen ionic vacancies, electrons or holes over the device govern the resistive switching process. b) Current-voltage profile of a memristive device, exemplified for a bipolar resistive switch. Two different resistance states (R_{off}/R_{on}) can be defined and used to store information.

A plethora of underlying physical effects can be source of such memristive phenomena. Resistive switching memories can be classified based on their assumed switching mechanism[22]: Electrochemical metallization systems are based on the formation of metallic filaments through the insulating switching layer. For this type of memristive system one active electrode must be made of a non-noble metal, which can be *e.g.* Ag[23] or Cu[24]. The metal of the active electrode then gets oxidized and migrates to the other electrode through the oxide structure, where it gets reduced and starts to form a metallic filament. Once this filament has reached the first electrode, it has created a low resistance metallic pathway, which sets the device to the low resistance ON state. Once the polarity is switched, the filament gets dissolved electrochemically, whereby the resistance is increased, returning the device back into its initial state.

Another class are valence change memories. Those are mostly metal oxide systems with metallic electrodes which are not easily and reversibly reduced or oxidized. For these systems, very often the switching layer has at least one transition metal or rare earth sublattice that can undergo redox reactions, allowing considerable changes in the local oxygen

nonstoichiometry. Many mechanism leading to resistive switching in such material systems have been proposed, relying for example on formation of conductive filaments over oxygen and other defects, interfacial type reactions or local changes in charge carrier density upon bias in the oxide component of the switch, Figure 1.1a. A number of great reviews giving an excellent overview are available; see reviews by the Waser group[22], Mohammad group[25] or Ielmini[26]. Depending on the material system and the mechanism a so-called preforming or electroforming process might be necessary for valence change memories. For example, the first formation of filaments can be carried out during electroforming, which is very often at higher voltages, currents or longer durations than the targeted operation condition as memristive memory.

The semiconducting or insulating switching phase for the resistive switches, also referred to as memristors, can be made of different materials; however, most materials are oxides. Many of them are commonly used as high-κ dielectric gate oxides in transistors. This ensures easy integration into semiconductor fabrication[27] and CMOS-compatibility[28]. The most progressed application envisioned for memristive devices is the use as non-volatile digital memory[29], although other analogous applications are also being researched, *e.g.* artificial neural networks[30,31]. Memristive memories are very competitive compared to other emerging memory technologies, see Table 1.1. They are ns-scale fast, non-volatile memories with low power consumption in the pJ range and have the potential to replace both DRAM and Flash memories by merging their distinct advantages. Another very promising new memory technology are spin-transfer torque magnetic random-access memories (STT-RAMs). They are fast, non-volatile and low power consumption memories, with the advantage that their switching process does not involve any mass transport, which has positive impact on the endurance[32]. However, disadvantages are they require very complex material stacks in their fabrication and that the maximum achievable R_{off}/R_{on} ratio is very limited[33].

Furthermore, their low power consumption might help to mitigate the problem of insufficient heat dissipation (dark silicon) in the future[34]. Most

memristive devices that are currently investigated are made of simple metal-insulator-metal sandwich structures, with the insulator very often being one of the commonly used gate oxides, *e.g.* HfO_2[35], $SrTiO_3$[36] or TiO_2[18]. There are only very limited options to design the material for the switching oxide, for instance extrinsic doping is limited by the low solubility limits of dopants and the stability range, such as in titania or titanates[37,38]. Based on this observation, this leaves plenty of opportunities to explore novel and unconventional avenues for modulating the switching material in order to establish new design criteria. In the following, we introduce interfacial strain-engineering as a new and very promising way of tuning material properties beyond the current scope of classic extrinsic doping in alternative oxide systems. In conclusion, this thesis explores first concepts on multilayer strain modulation for resistive switches as a potential new device prototype.

Table 1.1: Comparison of current and emerging memory technologies[34,39-42]. This table also highlights the potential of various emerging memory technologies. Not every property of the emerging memory technologies is realized in a single device.

	Oxide based RRAM (Memristor)	Phase change memories (PCM)	Spin-transfer torque magnetic random-access memory (STTRAM)	Dynamic random-access memory (DRAM)	Flash memory
	Emerging technologies			*Commercialized technologies*	
Energy per bit (ns)	2	100	0.02	2	0.01
Read time (ns)	10	10	10	10	80
Write time (ns)	10	100	10	10	$2x10^5$
Retention	non-volatile	non-volatile	non-volatile	volatile	non-volatile
Endurance (cycles)	10^{12}	10^{12}	$>10^{12}$	10^{16}	10^5

2   Multilayers and Strain at Interfaces

In the last decade the use of interface engineering to generate additional functionalities and to modulate properties has gained considerable attention due to major advancements in thin film technologies for fabrication and characterization at the micro- and nano-scale. For instance, it was found that heterostructures and interfaces at very small scales can have many unprecedented properties at very small scale, *e.g.* superconductivity[43], magnetism[44], previously unknown optical properties[45] or ionic conductivity modulation [46]. These properties stem from a variety of physical effects, *e.g.* space charge effects and/or strain at the interface which alter two important characteristics: (i.) the local interfacial ionic near order positions and (ii.) the local charge carrier density within the oxide volume, *i.e.* the number of available and mobile defects. The change in near order alters actively the ionic migration hopping distances and energies. Compared to previous decades, where a lot of research was dedicated towards the optimization of microstructures and the influence of doping[47], this opens completely new ways of designing and enhancing materials. Amongst those, strain engineering is anticipated to be a very promising research direction which has a wider implication. It has the potential for some systems to alter the ionic carrier transport to a greater extent than what may potentially be achieved through classic extrinsic doping in many of those oxide systems. The concept of strain engineering is already being successfully employed in the semiconductor industry for electronics, for example in electronic conducting transistors utilizing strained silicon to enhance the electronic mobility[48] and in heteroepitaxy for monolithic integration of new materials onto Si wafers[49].

Strain can be either compressive or tensile. For the case of compressive strain, the lattice constant is reduced and the atoms/ions are closer together than in the relaxed bulk state. For tensile strain, the lattice constant is expanded, and the atoms/ions are further apart, see the schematic of Figure 2.1a and b. It was confirmed in experimental studies by the groups of Janek[50,51] and Hertz[52,53], and computational studies by the groups of Yildiz[54] and De Souza[55,56] that tensile strain in oxides often

9

increases the oxygen ionic conductivity when probed at higher temperature (usually > 500K). In contrast, compressive strain decreases oxygen ionic conductivity for classic ionic conductors when imposed on zirconia or ceria based crystal lattices[46,57-59].
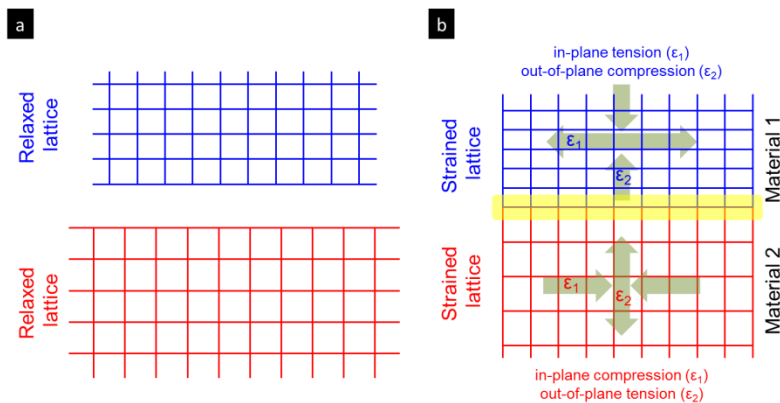
Figure 2.1: Relaxed and strained lattice states. a) Relaxed lattice states. The lattice constants display bulk conductivity values, e.g. for oxygen ions migrating. b) Epitaxial or textured thin film growth. The two material phases are in contact with each other, whereby one material is compressively strained in-plane while the second material is tensely strained in-plane. Strain of the opposite sign is predominant in out-of-plane direction.

Many applications require fast oxygen ionic conductivity at low temperatures[60]. Enhancing the ionic conduction was a key goal of research groups, since it is of outstanding importance for many technologies, like sensors[61,62], energy storage and conversion systems[60,63] and information systems[21,22].

To introduce strain in a controlled fashion, two different designs are utilized[46]. One is the deposition of a single thin film on a substrate, where the strain is defined by the lattice mismatch between the thin film material and the substrate. The other approach is a multilayer design, where two materials are stacked consecutively in an $(A\text{-}B\text{-}A\text{-}B)_n$ manner. In this case the interfacial mismatch is defined by the lattice constants of the two thin film multilayer constituents. The latter design approach has the advantage

that the total volume is not limited. In a single thin film the strain relaxation gives a limit for the amount of material that can be under strain. In the multilayer approach a new strain field is generated at each interface; therefore, the total strained volume can be controlled through the number of consecutive monolayers defined in a given oxide building block.

In the year 2000, the group of Maier firstly used the concept of heterolayers to modulate ionic transport, exemplified for the material system BaF_2/CaF_2[64]. They showed that increasing the number of layers, while maintaining a constant total film thickness, allowed the modulation of the conductivity of the system by impressive ~2 orders of magnitude. They explained the conductivity change with a space charge model, where the space charge extends throughout the whole sample when the interfacial density is increased and forms a continuous zone with a different charge transport behavior. In 2005, another work on a multilayer-based system was published by Azad et al.[65], where an oxide-conductor based on a gadolinia-doped ceria/zirconia stack was investigated and a modulation of the conductivity with increasing number of interfaces at constant total film thickness is being observed. The concept of modulating ionic conductivity through interfacial strain gained an additional boost when Garcia-Barriocanal et al.[66] reported on the material couple yttria-stabilized zirconia (YSZ)/$SrTiO_3$ (STO) for multilayer structures. They reported an eight orders of magnitude increase of conductivity and a decrease of activation energy by $\Delta 0.5$ eV for a modulation of interfacial strain of up to 7%. These results were attributed to large tensile strain in the system, although the interpretation of the observed results has been debated[67,68].

In literature there is a debate about the influence of strain on conductivity. Some studies show a big change in conductivity with respect to strain as exemplified a computational study carried out in the system perovskite, $KTaO_3$ and Yttria-stabilized zirconia by Li et al.[69]. Depending on the lattice strain they were able to calculate a decrease of the activation energy of up to $\Delta 0.33$ eV for zirconia. They estimated the ionic conduction to be up to more than seven orders of magnitude higher than

for unstrained bulk zirconia. Other studies predict a more moderate but still significant change in oxygen ionic conductivity, such as in the computational work by Kushima *et al.* from the Yildiz group[54]. They compute a maximum enhancement of 6.8×10^3 at 4% tensile strain. Similar results were obtained by De Souza *et al.*[55]. Tarancon *et al.*[70] confirmed that the maximum conductivity enhancement of 1.5 orders of magnitude can be obtained for a strain value of ~3% for the material system of yttria stabilized zirconia, being in agreement with earlier predictions of the Yildiz team[54].

In contrast, the experimental study by Pergolesi, Traversa and Kilner[71] didn't find any conductivity modulation through strain when investigating a yttria stabilized zirconia/ceria multilayer system. Recent work by Fluri and Pergolesi[72] with the oxide $Ce_{0.85}Sm_{0.15}O_{2-\delta}$ has demonstrated small conductivity and activation energy changes, but for rather small strain values for up to 0.35%. Their work focused on showcasing the usefulness of novel diagnostic methods for growth mode analysis and strain determination.

This large disparity in results triggered great interest in classifying the studies available and trying to understand where these differences originate, see section 4 for an additional discussion on selected prime aspects. Since many different material systems and design approaches have been used, this is not trivial. Korte *et al.*[57] have conducted a comprehensive literature review and classified the experimental data on an interfacially strained system in three different categories.

- Strain controlled oxide systems that usually are made of extrinsic conductors (heavily doped systems)[51,73-79]. Heavily doped oxides (like gadolinium-doped ceria or yttria-stabilized zirconia) have very high concentrations of charge carriers and rather small space charge regions due to the small Debye length present[80].
- Surface controlled systems that consist of a single extrinsic oxide conductor with the conducting phase exposed to the atmosphere[65,81-86].

- Space charge controlled systems, employing intrinsic conductors, *i.e.* not extrinsically doped materials as constituents[64,87-89], usually in a multilayer stack design.

In the first group, the strain controlled systems; the total conductivity modulation is rather small compared to the other groups. Since these systems have negligible small space charge regions, the conductivity modulation comes either purely from strain effects or from misfit dislocation. The thin film microstructure, *e.g.* grain boundary density, can also play a role.

In the second group, the surface controlled systems; the conductivity modulation is usually higher, since transport along solid-gas interfaces is faster[57]. This can be due to a higher energy of interfacial species, but also due to a decreased number of bonds for each atom/ion.

The last group, space charge controlled systems, displays an increase in conductivity through interfacial engineering that is higher than in the strain and surface controlled group, which stems from the fact that the initial (bulk) ionic conductivity of the materials used is rather low and the conductivity increase in the space charge regions is relatively high.

2.1 Growth of Oriented Thin Films and Description of the Interfacial States

To get well-defined interfacial states in a multilayer, it is necessary to grow samples with a good crystalline quality and with a certain preferred orientation. Usually a single-crystalline substrate with a suitable crystal structure and orientation is chosen as substrate for the thin film deposition. Depending on the deposition method and parameters, amorphous, polycrystalline or fully epitaxial samples can be obtained. In amorphous samples, there is no far-range order although some systems display near-range order, *e.g.* glass[90]. Polycrystalline samples have long range order, but consist of crystallites (grains) with different sizes and orientations. Apart from the grains, a second phase, termed grain boundaries, exists in polycrystalline materials. The size of the grains, and

as a consequence, the grain to grain-boundary ratio is heavily dependent on the processing conditions. Grain boundaries usually tend to decrease the ionic conductivity[91] and are zones of structural disorder[92]. Epitaxial films, on the other hand, are single crystalline and display no grain boundaries.

Interfaces, as they exist in heterostructures, can be coherent, semi-coherent or incoherent[51,93,94]. If the mismatch between the substrate and thin film is below a certain threshold, the interface between substrate and film (and subsequently between the two different multilayer constituents) grows coherently, see Figure 2.2a. This requires the 2 crystal lattices to match well, with respect to the orientation and the atomic spacing. The small mismatch between two materials can be accommodated through elastic strain and there is no discontinuation of the crystalline lattice. If the lattice mismatch exceeds a certain threshold, a semicoherent interface will be created, see Figure 2.2b. In this case, a part of the lattice mismatch and the corresponding strain will be accommodated by dislocations, which can also be arranged in a continuous array. For an incoherent interface, see Figure 2.2c, one can observe a disordered structure at the interface.
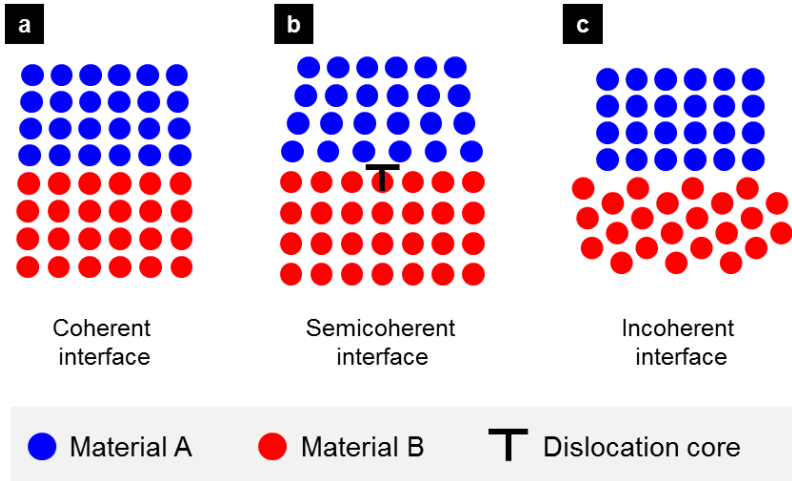
Figure 2.2: Types of Interfaces: a) Coherent interface. The lattices of the two phases are continuous. b) Semicoherent interface. Dislocations at the phase boundary are created. c) Incoherent interface. The interface is a zone of structural disorder.

Incoherent interfaces are, by definition, ill-defined and should be avoided. This can be done through the choice of appropriate substrates, thin film materials and processing conditions. . The critical properties include the material lattice parameters, crystallography and growth directions. For a fundamental description see the work carried out by Janek's group[50,51,57,73-75,79,95], who were among the first in the field to carefully describe experimentally such strained oxide ionic transfer multilayer structures.

Strain fields are generated in mismatched interfacial zones. This can be uniaxial strain, where stress is acting only in one space direction, as is usually the case for one-dimensional systems or systems that were particularly designed for such purposes[96]. Interfacial strain in thin film systems usually is a biaxial strain. This means, the lattice is distorted in a controlled manner through oriented growth in *xy* direction (also called in-plane), parallel to the substrate surface. The lattice is also distorted in *z* direction (out-of-plane), perpendicular to the surface of the substrate, see Figure 2.3a for spatial directions. The degree of out-of-plane distortion

depends on the elastic mechanical properties, *e.g.* Young's modulus. For instance, if the lattice is under tensile in-plane strain, one can expect compression in the out-of-plane direction[97] and *vice versa*. The last case is isotropic strain, where the stress is acting simultaneously and with the same magnitude for all spatial directions.

In a multilayer thin film system we have two adjacent crystalline phases and both can undergo elastic deformation. The mismatch of the two phases relative to each other can be described by the following equation:

$$f = \frac{a_2 - a_1}{a_1} \qquad\qquad\qquad \textit{Equation 2.1.1}$$

Where *f* is the lattice mismatch and a_1 and a_2 are the lattice constants of the two materials, here denoted material 1 and material 2. The unit cells can also grow on each other with a certain commensurability, *e.g.* one big unit cell can grow on two small ones, if seen in side-view. The interfacial mismatch *f* will be in any case approximately equally distributed as strain on both materials, see Equation 2.1.2.

$$f \approx \frac{1}{2}\varepsilon_1 \approx -\frac{1}{2}\varepsilon_2 \qquad\qquad\qquad \textit{Equation 2.1.2}$$

where ε_1 and ε_2 are the tensile and compressive interfacial strains in the materials 1 and 2. They are predominantly present in the *xy*-plane at the interfacial boundaries and may relax at the grain boundaries within each material. The strain is the highest directly at interfaces and relaxes if the distance to the interface is increased[98,99]. Since we are considering multilayers, if the film thickness is sufficiently thin the strain fields originating start to overlap and the total strained volume is increased and reaches a maximum, reaching a maximum and yielding fully strained phases.

The microstructure of PLD grown thin film usually consists of many columnar crystallites[100] that form a dense film, see Figure 2.3a. This implies that grain boundaries are present in polycrystalline films deposited by PLD. Grain boundaries tend to decrease oxygen ionic conductivity for many fluorite-crystal lattice oxides, and may counteract strain-induced conductivity effects, particularly conductivity

enhancement introduced through tensile strain (*e.g.* zirconia, ceria). Modulation of the conductivity through strain is primarily occurring at the interfaces, where the strain fields originate. The charge transport is parallel to the interfacial boundaries and the conductivity is tuned through the strain modulated interfaces, see Figure 2.3b.
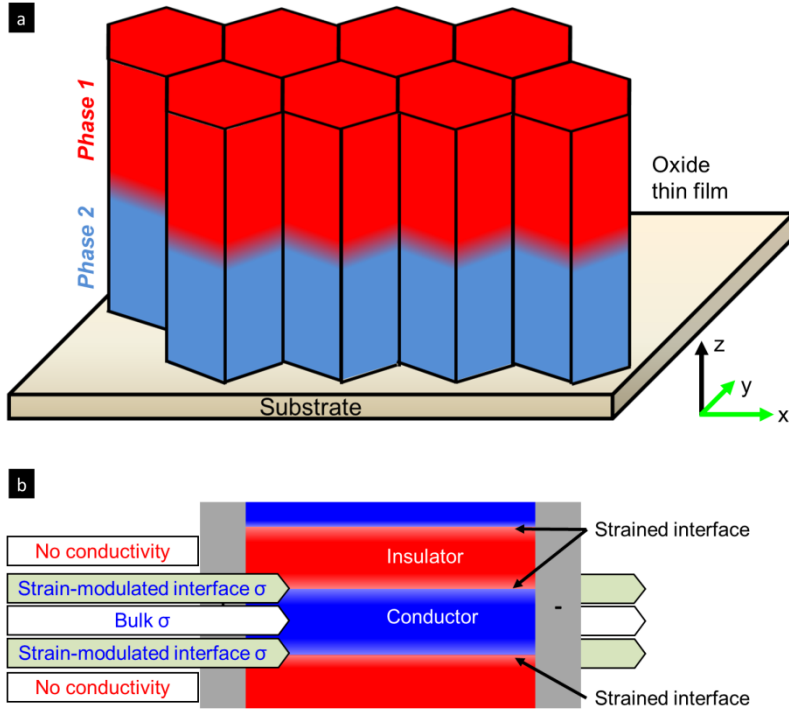
Figure 2.3: Texture and interface of the multilayer thin films a) Columnar microstructure after PLD deposition. If the interface between phase 1 and phase 2 is coherent, then both thin film materials form a continuous lattice in z-direction. In x-y plane grain boundaries are present. b) The conduction is parallel to the interfaces. Interfacial strain modulates the oxygen ionic conductivity along the x-y in-plane direction; therefore, it is beneficial to have sideways attached electrodes. No current flows through the insulator; it only serves the purpose to impose strain in the conductor.

2.1.1 Disorder at Interfaces

At interfaces intermixing or segregation can occur, leading to inhomogeneous distribution of ions close to the phase boundaries. This can also lead to the formation of new phases, may influence strain fields and alter space charge zones. These mixing/segregation processes are diffusion controlled and therefore more pronounced at elevated

temperatures. If one uses deposition methods that work at elevated temperatures, intermixing and segregation have to be considered.

Space charge zones can form at interfaces[101]. This describes the enrichment or depletion of charge carriers at the interfacial boundary region. If one charge carrier species is enriched in one phase, the charge carrier type with opposite charge will be enriched in the bordering interfacial region. An enrichment of charge carriers can lead to an increase of interfacial conductivity. In contrast, charge carrier depletion slows down the charge transport as compared to the bulk conductivity. The extent of space charge zones is usually in the range of the Debye length of the material.

The defect density at interfaces can also change. It was found that tensile lattice strain decreases the formation energy of oxygen vacancies in ceria[102,103], increasing the defect density in strained systems. Similar results were found for ceria with roughly 4% Gd doping[104]. Dislocations might also be responsible for an increase in defect density, although they can also impede charge carrier mobility[105].

The gas/solid interface (surface) of the multilayer thin film stack is of great interest, especially for applications like solid oxide fuel cells, where the triple phase boundaries are of paramount importance. The groups of Yildiz[106,107] and Fleig[99] have extensively investigated oxygen exchange kinetics and diffusion in oxides at surfaces under strain with various methods, *e.g.* ^{18}O tracer experiments, X-ray photoelectron spectroscopy (XPS) and scanning tunneling microscopy (STM). It was found that tensile strain dramatically improves the oxygen exchange kinetics and is a promising strategy for tuning the performance of solid oxide fuel cell cathodes (often perovskite compounds). Another interesting idea was followed by the group of Pryds, where they used highly coherent interfaces of erbia-stabilized Bi_2O_3 and gadolinia-doped ceria in a multilayer to increase the stability of the desired fast conducting cubic fluorite δ phase of Bi_2O_3, which resulted in exceptionally high conductivity multilayer film compounds.

2.1.2 Misfit Dislocations

If the elastic, misfit induced strain at the interface exceeds a certain threshold value, the materials start to release strain though the formation of misfit dislocations. There are two types of misfit dislocation, screw and edge dislocations, but many dislocations that are found in oxide materials have mixed characteristics[108].

Misfit dislocations also create their own strain fields, which can be the source of other effects inducing additional disorder, *e.g.* cation segregation, see also Sun *et al.*[109]. Dislocations also influence transport properties. For instance in metals they tend to decrease the resistivity, but Metlenko *et al.*[110] found that dislocations do not necessarily increase the diffusion in oxides, as they exemplified for $SrTiO_3$.

During commensurate (hetero)epitaxial growth, dislocations can form when a certain critical thickness is exceeded. Very recently, the group of Chueh *et al.*[111] have demonstrated experimentally that CeO_2 films can be coherently strained with film thicknesses of up to 2.7 nm, even at high misfits of ~5%. They proposed a model where a ceria film continues to grow in a 3D-island mode, which allows for additional strain relaxation. As a result the critical thickness for the formation of dislocations is much larger than expected in the reported films.

In another work by Sheth *et al.*[112], it was found that the substrate choice has a considerable impact on the formation of dislocations. High densities of dislocations were found in Pr-doped ceria on YSZ, while films grown on sapphire showed only a small dislocation count.

2.2 Characterization of Strain at Heterolayer Interfaces

Understanding the details of an interfacial state requires a careful and thorough experimental characterization. Various methods can be applied, each one having its distinct advantages and disadvantages.

2.2.1 X-Ray Diffraction based Techniques

One method that is commonly applied is X-Ray diffraction (XRD). XRD is useful because it allows conclusions about the spacing of the crystal lattices, and therefore gives some information about the lattice mismatches, to be directly drawn from experimental data. Conventional XRD using the Bragg-Brentano configuration yields information about the out-of-plane lattice spacing; however, a distortion in out-of-plane direction can give some hints about the total 3D strain states.

Reciprocal space mapping (RSM) is an X-ray diffraction technique that gives information about the in-plane and out-of-plane components of the lattice investigated; particularly well suited for thin films and multilayer structures. A peak that contains information about both spatial directions has to be selected, *e.g. hkl* = 113. In reciprocal space, strain will yield a shift of the Bragg reflections of the reciprocal lattice points relative to the substrate's peaks. One limitation of this technique is the spatial resolution. The spot size for micro XRD is usually 10 microns or bigger with commonly available equipment. For the strain investigation in small scale micro and nanodevices it would be necessary to go to a synchrotron light source, where sub-micron spatial resolution can be obtained.

X-ray diffraction based techniques are the most widely used methods to extract lattice strain information, *e.g.* Bragg-Brentano measurements by the group of Hertz[113], reciprocal space mapping by Lippert and Pergolesi[72] or by Sanna *et al.*[76]. These methods yield much information and are easily accessible in many labs.

2.2.2 Raman Spectroscopy Techniques suited for Area and Phase Analysis

While XRD relies on the measurement of cations position, Raman spectroscopy allows us to measure direct anion-cation interactions and therefore, allows us to also get insights into the defect chemistry. Furthermore, it constitutes an alternative way of investigating strain through the application of micro Raman spectroscopy[114].

Raman spectroscopy is a type of vibrational spectroscopy, where vibrations in the samples are optically induced. A laser excitation is scattered by the sample, resulting in both elastically and inelastically scattered light. The elastically scattered light as the same wavelength as the laser and is termed Rayleigh scattered. The inelastically scattered light leaves the sample with a different wavelength and can come from a variety of different processes. In this case we will focus on Stokes' scattered Raman light.

In Raman scattering, an energy shift contains information about the vibrational modes of the system under investigation. The vibrational modes of a system are heavily dependent on the symmetry and bonding conditions. For instance, if a material system has a cubic *fcc* structure like ceria (space group $fm\bar{3}m$) we can expect one single active Raman mode related to the breathing O-Ce-O bond, since all space directions are equivalent. If a system is under strain, this so-called degeneracy is lifted since not all spatial directions are equivalent, see section 2.1. In this case, we can observe a peak splitting of the Raman mode to an in-plane and out-of-plane mode. This concept has been applied, for example, to strained silicon[115], but is still rarely investigated for oxides and needs further attention from a technical point of view. Importantly, the observed shift of the Raman mode is related to the strain value. Since the bonds are stretched and compressed their vibrational frequency changes, with a redshift (shift to a smaller wavenumber) under tensile strain and a blueshift (shift to a larger wavenumber) under compressive strain. The magnitude of the shift can also be directly related to the magnitude of strain. There are several ways of calibrating the frequency shift to a real strain value. One can use experimental values obtained through applying pressure with a diamond anvil cell and use these strain-shift-coefficients to estimate the strain in the system. The other option is to use simulations, *e.g.* DFT calculations, to establish a correlation between strain and Raman shift. The third option is to solve a secular equation relating the frequency shifts to strain, as detailed in Ref.[115]; however, this requires knowledge of the phonon deformation potentials, which are only known for a few material systems and not trivial to obtain.

A pioneering work using Raman microscopy to map the strain in oxide heterostructures was published by the Kreisel group[114]. They demonstrated the application of Raman microscopy with many different excitation wavelengths to investigate an oxide heterostructure and probe the strain within individual layers using optical effects, *e.g.* absorption or resonance effects. Through this wavelength-dependent approach the different monolayer (phase) contributions of the oxide multilayer could clearly be maximized in the vibrational coupling with the Raman light, and a multilayer with four different oxide phases was characterized at best to our current knowledge.

One major advantage of Raman microscopy is the spatial resolution, which is, depending on the excitation wavelength and the microscope optics used, in the range of a few 100 nm. Importantly, this spatial resolution can be used for mapping and is much smaller than what can conventionally be achieved through XRD lab techniques. For mapping, the laser is moved across the sample and creates a distribution map of the chemistry of the sample. This can be for example used to investigate the spatial distribution of chemical species in oxide-based microdevices.

Both XRD and Raman microscopy are non-destructive techniques and can also be applied for process control, although one has to be careful that the excitation laser in Raman microscopy does not induce changes due to heating of the oxide material or imaging artifacts like fluorescence disturbing the measurements (note that such effects are known for zirconia oxygen ionic conductor depending on the incoming wavelength).

2.2.3 Transmission Electron Microscopy

Transmission electron microscopy (TEM) can also be used to investigate thin films. This technique has some striking advantages over the previously mentioned techniques. One is that it can be used for imaging, so one can directly observe the heterostructure layers. Diffraction analysis can also be used to study the crystallographic relations at very small scales. The other techniques usually study the full extent of the thin film, but with TEM the single constituents of the multilayer thin film stack can be studied. A major disadvantage is that samples must be transparent for

electrons, *i.e.* they need to be very thin. Such thin samples, so-called TEM lamellas, can be prepared through the site-specific ablation with a focused ion beam (FIB) and subsequent lift-out. Another option besides ion etching is mechanical polishing of the sample to the desired thickness. Very often a final thinning step employing ion milling is necessary.

2.2.4 Wafer Curvature Measurement and in-situ Growth Analysis with Multi-Beam Optical Stress Sensors

Novel methodologies to gain a deeper understanding of film growth and strain evolution are also developed, as exemplified by Fluri *et al.*[72] in the Lippert team. They show the strength of a combined multi-beam optical stress sensor (MOSS) and reflection high-energy electron diffraction (RHEED) investigation. The measurement of stress with MOSS uses the principle that the deposition of a stressed thin film bends the substrate, and the resulting, so-called wafer curvature can be analyzed using Stoney's equation[116]. MOSS works through the projection of a regular array of laser spots onto the substrate and measuring the evolution of the relative distances between the spots, yielding the wafer curvature. RHEED uses an electron beam at very small angles and the resulting diffraction pattern can be correlated to the growth modes of the thin films, *e.g.* island-type or layer-by-layer mode.

Thorough characterization of the samples is very important, since it is hard to predict the interfacial states by the design of the experiments. All methods are independent and complementary and a combination of these methods will yield the most complete picture of the interfacial states and is focused on in the thesis from a technical perspective.

2.3 Conductivity Modulation through Multilayer Interfaces

In order to modulate the defect and charge transport characteristics of a multilayer system the two multilayer constituents have to be chosen carefully. Both phases are under strain, whereby the first one is supposed to have increased electrical conductivity under tensile strain, and the

second one is expected to display decreased conductivity under compressive strain. One possible approach is to choose one phase to be an electric insulator, while the other one is a semiconducting phase. In that case the insulating phase only serves the purpose to impose strain on the conductor phase. If the relative difference of the conductivities is big enough, one can use a model to describe the conductivity that only takes one strain contribution into account namely the strain-modulated conductivity of the conductor, into account, Figure 2.3.

The total conductivity of a material, in this case the conducting phase of the multilayer, is a sum of the ionic and electronic conductivity, Equation 2.3.1.

$$\sigma_{total} = \sigma_{electronic} + \sigma_{ionic} \qquad \qquad \textit{Equation 2.3.1}$$

The charge carriers involved can be either electrons or holes for electronic conductivity ($\sigma_{electronic}$) and for the present material systems either oxygen ions or oxygen vacancies for the ionic conductivity (σ_{ionic}), depending on the defect chemical model used. In general, the conductivity is governed by the number and the mobility of charge carriers, as displayed in Equation 2.3.2 and Equation 2.3.3 for the electronic and ionic conductivity, respectively;

$$\sigma_{electronic} = e_0 n_e v_e \qquad \qquad \textit{Equation 2.3.2}$$

$$\sigma_{ionic} = q n_i v_i \qquad \qquad \textit{Equation 2.3.3}$$

where e_0 is the electron charge, n_e is the number of electronic charge carriers and v_e is the mobility of the electronic charge carriers. q represents the ionic charge, n_i and v_i are the number of ionic charge carriers and the ionic mobility, respectively. This means a conductivity modulation through multilayer interfacial influences has to be mediated through a change of the charge carrier density or the charge carrier mobility, respectively. For the case of oxygen vacancy conductivity, the ionic conductivity can be written as

$$\sigma_{ionic} = (2q)[V_O^{\cdot\cdot}]v_i \qquad\qquad \textit{Equation 2.3.4}$$

where $[V_O^{\cdot\cdot}]$ represents the concentration of oxygen vacancies. The ionic conductivity of a doped fluorite structure (where one can assume a fixed number of charge carriers) can be rewritten as

$$\sigma_{ionic} = (2q)[V_O^{\cdot\cdot}]\frac{v_{0i}}{T} exp\left(-\frac{\Delta H_{mig}}{k_B T}\right) \qquad\qquad \textit{Equation 2.3.5}$$

ΔH_{mig} stands for the migration enthalpy and k_B for the Boltzmann constant. We can merge the ionic charge, the charge carrier density and the pre-exponential ionic mobility, v_{0i}, factor into one expression and rewrite Equation 2.3.5 as

$$\sigma_{ionic} = \frac{A_0}{T} exp\left(\frac{-\Delta H_{mig}}{k_B T}\right). \qquad\qquad \textit{Equation 2.3.6}$$

where A_0 is a preexponential factor that contains, for instance, the concentration and charge of the charge carriers or the jump distance. Those shouldn't be modified substantially by strain, leaving migration enthalpy as quantity that is modulated by interfacial strain.

For biaxial strain, the migration enthalpy can be expressed as

$$\Delta H_{mig} = \Delta E_{mig} - \frac{2}{3}\sigma_{xx}\Delta V_{mig} \qquad\qquad \textit{Equation 2.3.7}$$

where ΔE_{mig} is the migration energy, σ_{xx} is the biaxial strain and ΔV_{mig} is the migration volume. The biaxial strain σ_{xx} can be defined as

$$\sigma_{xx} = 3B\frac{1-2v}{1-v}\frac{a-a_\varepsilon}{a_\varepsilon}. \qquad\qquad \textit{Equation 2.3.8}$$

B stands for the bulk modulus, v for Poisson's ratio and a and a_ε for the unstrained and strained lattice constants, respectively. ΔV_{mig} is the migration volume, and can be defined as follows:

$$\Delta V_{mig} = \frac{\partial \Delta G_{mig}}{\partial p_{eff}} \qquad\qquad \textit{Equation 2.3.9}$$

ΔG_{mig} is the Gibb's free energy of migration and p_{eff} the applied pressure.

2.4   Thin Film Deposition

The deposition method has large impact on the final state of the interface. For ceramics, several methods for thin film deposition are established. Spray pyrolysis has the disadvantage of crack or pore formation in the films since the precursors are sprayed with organic solvents that require thermal post-treatment[117]. The as-deposited films are often in an amorphous state whereby the crystallization kinetics and defect formation are challenging to control[118].

Deposition methods that are better suited to meet the requirements are vacuum based physical vapor deposition techniques. Sputtering and pulsed laser deposition (PLD) are commonly employed for the growth of dense thin films and can also be done non-thermally. Molecular beam epitaxy is a technique that allows the growth of atomically smooth films, but requires expensive equipment. Another option that allows the growth of monolayers is the vacuum based atomic layer deposition (ALD). Two of the most used methods for thin film deposition are PLD and sputtering. PLD offers some distinct advantages over sputtering[119]:

- Almost every species of condensed matter can be deposited.
- Even for complex systems the desired stoichiometry can be transferred to the substrate.
- The porosity can be controlled through the partial pressure during deposition, which is particularly important to create dense films for electric applications.

However, one major limitation of PLD is the limited area homogeneity during deposition, resulting in scalability challenges for mass production.

The basic working principle of PLD is that in a vacuum chamber a laser is directed onto a ceramic target that has the desired chemical composition, see Figure 2.4. Very often the targets are polycrystalline. The laser beam creates a plasma of the to-be deposited material, which is then directed onto a substrate. During this deposition phase, a working gas has to be introduced, to attain the correct stoichiometry. For most oxides O_2 is used.

The substrate onto which the film is grown can be heated. For textured or epitaxial growth it is normally required to heat the substrate.
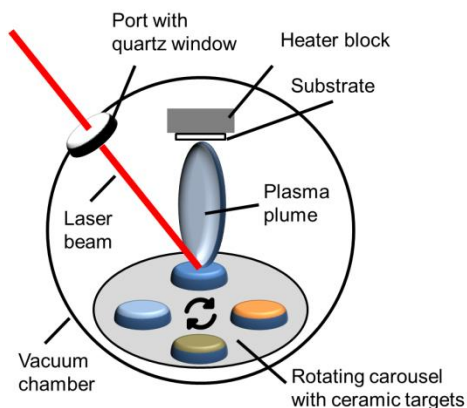
Figure 2.4: Working principle of a PLD system. A laser beam is directed through a quartz window into a vacuum chamber onto a ceramic target. A plasma plume is created and the material is deposited through the plasma onto a heatable substrate. The deposition process of oxides is usually carried out in an oxygen atmosphere.

The target materials required can be prepared from powders through classic solid state ceramics synthesis and processing. Also, the powder constituents for target preparation can for example be synthesized from the nitrates using Pechini synthesis. Conventionally, the powder is then pressed, preferably also isostatically, and subsequently sintered to obtain dense pellets as PLD targets.

3 Materials and Defect Chemical Models for Multilayers

In this work, a multilayer design is being employed which is composed of three constituents: the substrate, the conductor and the insulator. The conductor transports all the charge carriers, which will be modulated through strain, while the insulator only serves the purpose to impose strain on the conductor. The substrate is the platform on which the device will be grown.

## 3.1 Material for the conducting phase of the Multilayer

Gadolinia-doped cerium oxide with a doping concentration of 10% was selected as conductor for the multilayers. It has a simple face-centered cubic fluorite type structure with the chemical formula $R_xCe_{1-x}O_{2-\delta}$, where R represents trivalent doping cations It is a very well characterized model system and its defect chemistry is well understood. Besides that, it has some distinct advantages over other ionic conductors. Doped and undoped ceria have considerable phase stability over a wide range of temperature and atmospheres[120]. If ceria is being reduced, it compensates the negative charge by introducing additional oxygen vacancies, see Equation 3.1.1 for representation in Kröger-Vink notation[121].

$$2Ce_{Ce}^x + O_O^x = \frac{1}{2}O_2(gas) + V_O^{\cdot\cdot} + 2Ce_{Ce}' \qquad \textit{Equation 3.1.1}$$
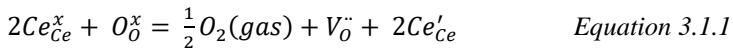
Extrinsic doping is often used to establish a well-controlled defect concentration, *e.g.* through addition of trivalent dopants such as Gd_2O_3, see Equation 3.1.2.

$$Gd_2O_3 \rightarrow 2Gd_{Ce}' + V_O^{\cdot\cdot} + 3O_O^x \qquad \textit{Equation 3.1.2}$$

Using doped ceria allows for good control over the number of defects in the system. Different trivalent dopants can be applied, and depending on the cation radius, a different maximum ionic conductivity can be obtained, with Gd^{3+} and Sm^{3+} yielding the largest enhancement of ionic conductivity[122]. There is also an optimum dopant concentration for the highest oxygen ionic conductivity for a given solid solution. An increased

density of defects leads to rising of the conductivity, but above a certain threshold, of around 10 to 15 mol% trivalent doping in ceria, the conductivity is reduced due to defect clustering of oxygen vacancies with the dopant cation, see Ref.[120] for details.

Ceria is described as a mixed ionic-electronic conductor, with oxygen ionic and n-type conductivity. However, without extrinsic doping the ionic conductivity is negligible for most applications[123].

Besides doping with trivalent cations, further reduction of ceria can introduce additional defect in the form of excess electrons, which can raises the electronic conductivity through the increased defect density. A reduction to Ce_2O_3, where the Ce_2O_3 unit cell can be constructed by 8 CeO2 unit cells[124], for example the band gap by impressive $\sim \Delta 1 eV$[125,126].

3.2 Material for the insulating phase of a Multilayer

The insulating phase needs to be cubic, same as the conductor phase, to ensure epitaxial growth or good commensurability of the multilayers. It should have a lattice constant that is close to the lattice constant of $Gd_{0.1}Ce_{0.9}O_{2-\delta}$ to stay in the elastic strain regime and to obtain coherent interfaces. The insulator needs to have a phase stability that is comparable to the conductor and no intermixing should occur. Most importantly, its electric conductivity should be several orders of magnitude below the conductivity of the conductor to ensure that all current flows through the conductor of the multilayer in a defined and describable manner.

Most rare earth sesquioxides are suitable candidates to serve as the insulating multilayer phase. For the present work it was carefully analyzed that among the sesquioxides Er_2O_3 is a good candidate with respect to the above-mentioned requirements. It can induce a coherent interface based on lattice mismatch to the ceria-based second phase, and is an inactive electric conductor. For a more detailed lattice mismatch analysis of various material couples we refer to our analysis of considered materials in Table 3.1.

Based on careful literature review we were the first to make $Gd_{0.1}Ce_{0.9}O_{2-\delta}$/$Er_2O_3$ multilayers, based upon the best mismatch conditions and the conducting properies of $Gd_{0.1}Ce_{0.9}O_{2-\delta}$ and the insulating properties of Er_2O_3. The Raman signatures of both materials were also considered to facilitate probing *via* Raman spectroscopy later.

Table 3.1: Calculated lattice mismatches for various material couples. The numbers in the second line of the first column display the lattice constant. All materials are cubic. The labels (P), (S) and (F) stand for perovskite, sesquioxides and fluorite structure. Materials highlighted in red were considered as conductor phase, materials in purple were considered as insulating phase. A negative sign indicates that the material in the first row is under compression, e.g. the mismatch for the couple $Er_2O_3/Gd_{0.1}Ce_{0.9}O_{2-\delta}$ is calculated towards $Gd_{0.1}Ce_{0.9}O_{2-\delta}$. Values that are highlighted in yellow indicate film growth in an one-to-two commensurability. The data displayed is based in crystallographic data from the Inorganic Crystal Structure Database[127].

	$SrTiO_3$ (P) 0.3905	$SrTiO_3$ (45°) (P) 0.5523	Sc_2O_3 (S) 0.9850	Lu_2O_3 (S) 1.039	Gd_2O_3 (S) 1.0809	Er_2O_3 (S) 1.0547	$Gd_{0.1}Ce_{0.9}O_{2-\delta}$ (F) 0.5418	$Y_{0.1}Zr_{0.9}O_{2-\delta}$ (F) 0.5141	Y_2O_3 (S) 1.0604
$SrTiO_3$	0.00	-29.30	-20.71	-24.83	-27.75	-25.97	-27.93	-24.04	-26.35
$SrTiO_3$ (45°)		0.00	21.65	11.88	4.29	8.98	1.90	6.92	8.00
Sc_2O_3			0.00	-5.48	-9.74	-7.11	-10.01	-4.39	-7.65
Lu_2O_3				0.00	-4.03	-1.54	-4.29	1.04	-2.06
Gd_2O_3					0.00	2.40	-0.25	4.88	1.90
Er_2O_3						0.00	-2.74	2.51	-0.54
$Gd_{0.1}Ce_{0.9}O_{2-\delta}$							0.00	5.11	2.14
$Y_{0.1}Zr_{0.9}O_{2-\delta}$								0.00	3.04
Y_2O_3									0.00

3.3 Material Selection for Strained Multilayers - Electronic Contributions to the Total Conductivity

In addition to ionic contributions, the material's electronic contributions to the overall conductivity need to be carefully considered. Er_2O_3 is an electronic and ionic insulator, like most rare earth oxides, except for praseodymium and terbium oxide, which exhibit some semiconducting properties[128]. Doped ceria is a predominant ionic conductor under most environmental conditions (intermediate to high oxygen partial pressure range); therefore, it is also commonly used as solid state electrolyte, *e.g.* in solid oxide fuel cell applications[60]. However, in thin films, interfacial effects can lead to a chemical reduction and thereby induce electronic conductivity. An O^{18} tracer experiment was carried out for the systems YSZ/Sc_2O_3[95] and YSZ/Y_2O_3[74]. It was found that the change in conductivities is equal or less than the change in diffusivities, leading to the conclusion that the contribution of electronic conductivity to the total conductivity is negligible, since only ionic transport is measured in a diffusion experiment.

A fully reduced interface of ceria was found by Song *et al.*[129] for the material system ceria/YSZ but no conductivity measurements were carried out in this study. Another study by Cavallaro *et al.*[68] revealed electronic conductivity by oxygen partial pressure dependent measurements for the material system $SrTiO_3/YSZ$. It is to be concluded that studies looking at the ionic *vs.* electronic contributions for strained multilayers are still rare in the field and require attention. When describing systems that operate under conditions where defect chemical models are not well established, *e.g.* at room temperature and under high electric fields, one should also take potential electronic contributions into account.

Ruiz-Trejo and Maier have found that in single crystalline samples of reduced, gadolinia-doped ceria at low temperature (room temperature to 110°C), the electronic conductivity is orders of magnitude larger than ionic conductivity[130]. The same holds for reduced, polycrystalline gadolinia-doped ceria in the temperature range of 25 °C to 100 °C[131].

3.4 Substrate

The method of sample preparation requires a substrate onto which the thin films are going to be deposited. The substrate has to fulfill many criteria:

- It needs to be electrically insulating.
- It has to provide the necessary crystallographic prerequisites for textured growth.
- It has to have a thermal expansion coefficient close to the thin film materials to allow deposition at elevated temperatures.
- There should be no interdiffusion between the materials.
- The substrate material shouldn't diffuse into the deposited thin films.
- CMOS compatibility is advantageous.
- Preferably, it should be inexpensive.

A commonly used substrate is sapphire, which fulfills almost all of the abovementioned criteria. The only criterion that is not covered is good CMOS compatibility, since the semiconductor industry is heavily dominated by silicon. The other option would be the use of silicon, but the requirements of electric insulation and crystallographic compatibility would require the coating of the silicon surface with several buffer layers, *e.g.* TiN for lattice constant matching.

4   Controversy

Analyzing the experimental and computational work on interfacial strain in the field of solid state ionics there is controversy about the influence of strain on conductivity. Some studies report colossal changes of ionic or total conductivity with respect to strain imposed in a multilayer structure, others report negligible changes. Differences in materials, sample design, microstructure and fabrication methods could be responsible for this disparity in results, but we want to summarize some of the results:

The review paper by Korte *et al.*[57] organized experimental studies with respect to sample design and has proposed to classify them in 3 classes, being strain controlled, surface controlled and space charge controlled systems, see section 2 for additional information. They also provide a comprehensive theoretical treatment. Concluding, they find that strain influences ionic conductivity at maximum by one order of magnitude. Blocking effects of grain boundaries might counteract an enhancement of the ionic conductivity; therefore, only samples of a similar microstructure can be safely compared.

One study investigating the influence of microstructure on layered systems was carried out by Pan *et al.*[132]. The authors deposited 2 sets of 20% Sm-doped ceria/Al_2O_3 multilayer systems. One was deposited at room temperature, so-called "non-textured" and one was deposited at high temperature, so-called "textured". The non-textured samples had a high density of randomly oriented grain boundaries while the textured samples showed a columnar microstructure. It was found that in the non-textured samples an increase of conductivity could be observed with an increasing density of interfaces and the opposite behavior was observed for the textured samples. They attribute this behavior to the fact that disordered, interfacial regions have a lower conductivity than the textured bulk and therefore, a higher number of interfaces decreases the total conductivity. The opposite trend is observable for the non-textured case, where they attributed the increase in total conductivity with increasing number of interfaces to an increased portion of high defect density regions and fast oxygen ionic pathways.

However, it has to be mentioned that no strain was observed in this study. This is probably caused by the use of polycrystalline substrates. Comprehensive studies connecting interfacial lattice strain and microstructure are still missing. The group of Janek discussed the effect of a columnar microstructure with grain boundaries on strained interfaces[74], but not every work published in the field looks at microstructural features, making comparisons between the works challenging.

It is also very important to consider the electrical contacting strategies used to measure electric transport in the strained multilayers. One strategy is sideways contacting, where the electrodes are placed at the sides of the thin film or multilayer stack. This bears the advantage that the electrodes can capture all internal interfaces. However, it has to be kept in mind that the interfaces are nanoscopic and the contacting method should be suitable. The other option is contacting through top electrodes, which might have the disadvantage that the electric field lines do not penetrate through the whole film. Also, the interface between the different materials in a multilayer system might block charge carriers. An advantage of the top electrode configuration is that it is easy to fabricate.

Some works have also discussed the influence of extended defects, *i.e.* dislocations. It was found that dislocations in oxides are not fast conduction pathways; another finding was that formation of defects is preferred at dislocations[110]. They are easy to reduce, but do not enhance oxygen ionic mobility[105]. However, no systematic investigation has been carried out so far. No widely accepted model to capture all these factors and use it to explain interfacial effects on conductivity for ionic materials has been proposed. Also not all factors that play a role, *e.g.* microstructure, have been investigated and disclosed in the published literature.

5   Aim and Outline of the Thesis

The aim of the thesis is to design and investigate strained ionically conducting multilayer oxide structures as constituents for novel strained memristive devices. The hypothesis is that strain at the interfaces of the multilayers can be actively used to alter ionic and/or electronic charge carrier in a conductive phase constituent over a wide range. These considerations are used to influence the current-voltage profile in own designed and operated memristive device bits.

It was previously shown, experimentally, that strain modulation of the ionic conductivity of fluorite structure oxides is particularly pronounced at lower temperature, hence it was deemed to be a promising approach to use interfacial strain as a design tool for the room temperature application of microelectronics. So far, only very limited material design tools have been applied in the fabrication of memristive devices and novel ways to control relevant properties, like charge carrier mobility, distribution and density. These are focused to affect memristance in a systematic manner through this thesis.

In this work, the material system $Gd_{0.1}Ce_{0.9}O_{2-\delta}/Er_2O_3$ was selected as model material system for strained multilayers as potential new strained memristive devices:

Part II aims at obtaining a fundamental understanding of the multilayered material system $Gd_{0.1}Ce_{0.9}O_{2-\delta}/Er_2O_3$, with the conductive $Gd_{0.1}Ce_{0.9}O_{2-\delta}$ phase being under compressive strain. New microfabrication routes to make microdots out of multilayers and detailed Raman microscopy for strain analysis are explored for this novel device type. Contacting strategies were reviewed and a suitable sideways attached metal electrode contacting strategy established for this type of microdot multilayer device. This allows capturing and modulating of real strain states at a small electrode separation.

Part III builds up on the achievements presented in part II. A considerable decrease in microdot device size is demonstrated. This is a requirement for operation as new memristive devices, since a high electric field strength is necessary. The interfacial strain states are probed with HR-

TEM and Raman microscopy. Raman microscopy is also used to obtain chemical device maps of the microdots and DFT computations are employed to analyze the data obtained through Raman microscopy. The effect of the multilayer-modulated strained interfaces on the current-voltage response was investigated with cyclic voltammetry. It was found that the ionic and the electronic conductivities are modulated by strain and interfacial effects. This part successfully demonstrated a new concept that can be employed for the modulation of the R_{off}/R_{on} ratio and the persistence of the system and ultimately a new type of strained memristive device for memory and computing architectures.

Part IV tries to answer a very fundamental question, which arose in the course of this thesis: Why do memristive oxide devices with a totally symmetrically aligned electrode/oxide/electrode unit, show non-linearity and asymmetry in their hysteretic current-voltage response?

Memristive devices with symmetrically aligned electrodes are fabricated where we successfully define both electrode interfaces as similar, which is important for the available defects at the interfaces and within the oxide compound; this was only possible by this unique symmetric in-plane multilayer dot architecture as at the same time small electrode distances need to be granted to allow resistive switching. Through making such model resistive switching structures with symmetric electrode-substrate and electrode-air interfaces one can study the pure effect that electroforming at different polarities has on resistive switching. Here, an artificial "electrochemical" symmetry break is introduced to learn how the switching is modulated with respect to polarity and magnitude. Studying the influence of asymmetry on the memristive response in more detail allows us to look closer on the electrochemical response and defect chemistry. This thesis chapter confirms that electroforming at different polarities yields current-voltage profiles with an exact mirror plane at zero volt. This is an exciting finding that has impact on future designs of memristors for bit and multi-bit structure applications employed for memories and higher non-binary computing architectures.

Part V summarizes the findings of this thesis, reflects on discussions in the literature and proposes a path for a future continuation of this work.

PART II

A Microdot Multilayer Oxide Device: Let Us Tune the Strain-Ionic Transport Interaction

6 Abstract

In this paper, we present a strategy to use interfacial strain in multilayer heterostructures to tune their resistive response and ionic transport as active component in an oxide-based multilayer micro-dot device on chip. For this, fabrication of strained multilayer micro-dot devices with sideways attached electrodes is reported with the material system $Gd_{0.1}Ce_{0.9}O_{2-\delta}/Er_2O_3$. The fast ionic conducting $Gd_{0.1}Ce_{0.9}O_{2-\delta}$ single layers are altered in lattice strain by the electrically insulating erbia phases of a micro-dot. The strain activated volume of the $Gd_{0.1}Ce_{0.9}O_{2-\delta}$ is investigated by changing the number of individual layers from 1 to 60 while keeping the micro-dot at a constant thickness, *i.e.* the proportion of strained volume was systematically varied. Electric measurements showed that the activation energy of the devices could be altered by $\Delta 0.31$ eV by changing the compressive strain of a micro-dot ceria-based phase by more than 1.16%. The electric conductivity data is analyzed and interpreted with a strain volume model and defect thermodynamics. Additionally, an equivalent circuit model is presented for sideways contacted multilayer micro-dots. We give a proof-of-concept for micro-dot contacting to capture real strain-ionic transport effects and reveal that for classic top-electrode contacting the effect is nil, highlighting the need for sideways electric contacting on a nanoscopic scale. The near-order ionic transport interaction is supported by Raman spectroscopy measurements. These were conducted and analyzed together with fully relaxed single thin film samples. Strain states are described relative to the strain activated volumes of $Gd_{0.1}Ce_{0.9}O_{2-\delta}$ in the micro-dot multilayer. These findings reveal that strain engineering in microfabricated devices allows altering the ionic conduction over a wide range beyond classic doping strategies for single films. The reported fabrication route and concept of strained multilayer micro-dots is a promising path for applying strained multilayer oxides as active new building blocks relevant for a broad range of micro-electrochemical devices, *e.g.* resistive switching memory prototypes, resistive or electrochemical sensors, or as active catalytic solid state surface components for micro-fuel cells or all-solid-state batteries.

7   Introduction

Lattice strain engineering is being discussed as a new route for tuning material and device properties in metal oxide films through the manipulation of mass and charge transport. Such films could be employed to improve contemporary metal oxide based devices for next generation energy storage and conversion or for new memristive memory and logic devices. For example, the field of nanoionics considers the fabrication and control of ionic and electronic migration by internal interfaces in heterostructures as a promising alternative to classic doping in metal oxides. This is realized by thin film heterostructures where a conventional metal oxide is replaced by repetitions of two oxide materials of varying electric transport and band structure characteristics. At each oxide film's interface variations in the interatomic distances, space charge, and local chemistry result. Since these are artificial thin film structures, size effects (defined by the total volume of the strained or space charged interface regions) provide a new degree of freedom in tuning the resistive and capacitive contributions. The range through which these parameters can be varied is also far broader than can be achieved for a single metal oxide; in particular because of the difference in the electronic structure at the interface which influences all mobile defects, namely electrons, holes, oxygen vacancies and ions. Classic examples of purely ionic (or mixed ionic electronic) conducting *heterostructures* are metal oxide films composed of an *insulating metal oxide* such as $SrTiO_3$, Al_2O_3, or RE_2O_3 with RE=Y, Sc or Lu, and an *ionic conductor* such as doped CeO_2 or ZrO_2[50,51,65,66,75,79]. The total ionic conductivity, which predominantly originates from the small band gap oxide phase (*i.e.* the ceria or zirconia-based phase), depends on the ionic defect migration and association energies and its oxygen vacancy concentration. These can be actively tuned through the imposed compressive or tensile strain of the insulating phase on the ionic conducting phase. Local variations in the near cationic-anionic order such as changed bond strengths as well as bond breaking and re-formation may happen at a strained interface.

The first computational studies revealed that strain at interfaces influences the migration energy barrier for oxygen diffusion[133-135]. First experiments by Sata[64] gave a proof-of-concept for conductivity engineering using

artificial BaF_2/CaF_2 heterostructures. Azad *et al*[65] showed an increase in the ionic conductivity of one order of magnitude for gadolinia-doped ceria/zirconia heterostructures with an increasing number of interfaces from two to sixteen at a constant film thickness (for 350°C). This was confirmed by a recent study of Sanna[76] reporting a one order of magnitude increase in ionic conductivity and a decrease in activation energy by $\Delta 0.33$ eV when increasing the number of interfaces from 1 to 19 at constant total film thickness. Garcia-Barriocanal even reported a strong increase of conductivity by eight orders of magnitude for the heterostructure $SrTiO_3$/Yttria-stabilized Zirconia (YSZ)[66]. This work triggered great interest in the field; however, the results have been debated[67,136]. Yildiz[54] and De Souza[137] concluded from computational results that the increase of conductivity due to strain in a $SrTiO_3$/YSZ heterostructure reaches a theoretical limit at 3 to 4 orders of magnitude. Systematic manipulation of compressive *vs.* tensile strain imposed on conducting YSZ phases for heterostructures composed of the materials Y_2O_3/YSZ, Ca-stabilized-Zirconia/Al_2O_3, Sc_2O_3/YSZ and Lu_2O_3/YSZ was thoroughly investigated in model experiments by Janek, Korte and co-workers[50,51,73-75,79]. It was reported that variation of the lattice misfits up to 3% tensile strain acting on the YSZ phase of the heterostructure substantially increased ionic conductivity; whereas the opposite trend (a respective decrease of conductivity) was measurable for -4% of compressive strain.

It can be concluded that several reports highlight the potential to change the transport properties in ionic-conducting heterostructures over a broader range when compared to single constituent materials. It is important to note that classic extrinsic doping in ionic conductors hardly modifies the overall ionic conductivity of zirconia or ceria by more than one to two orders of magnitude, for details see Rupp[138,139] and Omar[140]. Despite the promises of the first results the fundamental issue is how much the ionic conductivity of a fluorite-type oxide can be altered through lattice strain in a heterostructure. The hope for a new generation of electrochemical micro-devices stems from the ability to manipulate the strain-ionic transport interaction in metal oxide heterostructures. Nevertheless, up to now electrochemical micro-devices; *e.g.* fuel cells, sensors, batteries or memristive switches[141] which use strained metal

oxides as functional building blocks simply do not exist. In order to implement ionic heterostructures in commercial applications, an understanding of the strain-related near order changes and ionic transport are a basic requirement. New microfabrication routes to efficiently access the strain modulated resistive and capacitive volumes of the ionic conducting phases in the heterostructures need to be envisioned for new micro-device prototypes and are discussed throughout this work.

7.1   What is Critical for Electric Contacting Strategies on Ionic Heterostructures?

The questions requiring attention in order to implement strained ionic heterostructures as functional materials in micro-device concern both the *control over the near order interfacial states* and *new device fabrication routes* to access the strained oxide volume's resistive and capacitive contributions for measurements.

Near order interfacial states of strained ionic heterostructures; First, there is a debate on the magnitude of ionic conductivity enhancement for compressively and tensely strained ceria- and zirconia phases in heterostructures in literature. In some cases a strong increase is observed whereas in others no effect is measured for a similarly strained heterostructure oxide material and volume, see Santiso and Burriel[142] or Kilner[136] for details. In this sense, we believe that a critical aspect in comparison of the experimental results is *the electrode arrangement and fabrication relative to the strained volume fractions and interfaces of the heterostructure oxides*. Conventionally, electric transport/capacitance is measured in a 2- or 4-point electrode arrangement. Some authors apply the electrodes towards the sides of a grown multilayer on a single crystalline substrate *via* paste and wire macroscopically[51,81,85]. In that case the electric field lines are *along* the interface (parallel to the internal interfaces). Nevertheless it remains within the uncertainty whether all strained volume fractions of the heterostructure (down to a few nm in single layer thicknesses) are effectively contacted by this rather macroscopic contacting method. In other cases electrodes were deposited by metal sputtering *on top* of the heterostructure[71,143,144]. It is important to

note that here the electrodes are applied *parallel* to the strained interface. For the case that one heterostructure phase dominates in fast ionic conduction the electric field lines may be completely restricted to the top single layer and blocked at the insulating phase. Regardless of the effective strain acting on the ionic conducting phase, only the closest ionic conducting single layer to the electrode may contribute to the overall transport and the biggest fraction of the strained volumes would be missed in its contribution to total conduction.

Second, calculations of strain at the ionic heterostructure interfaces are based on classic long-range cationic structure determination tools like XRD[76] or electron microscopy[145] where anionic lattice positions are calculated but not physically measured. Interestingly, Korte measures inconsistencies in the remaining lattice strain of a single layer with respect to its thickness by XRD[51]. The authors concluded that the effective strained volumes contribute to the total oxygen ionic transport measured, however, structural modulations at the interface could not be resolved by XRD.

Our emphasis is on introduction of Raman spectroscopy as a new tool for systematically investigating changes in anion-cation bond strength with respect to strained volume fractions in ionic heterostructures. The anion-cation bonds are crucial for the ease of oxygen ionic hopping and can even directly be correlated in Raman spectroscopy *via* computational tools, *e.g.* DFT[139], to changes in migration and association energies. Recently, Raman spectroscopic studies on strain-transport interaction were reported for single metal oxide films with ionic bonds, *i.e.* for ceria[139] or $LaCoO_{3-\delta}$[146]. Raman spectroscopy is also commonly used to characterize strain states in covalently bonded semiconductors like Si[115], GaN[147], or graphene[148]. However to the best of our knowledge Raman spectroscopy studies on ionic conducting heterostructures are still missing in the field.

7.2 First Electrochemical Microdevices based on Strained Ionic Heterostructures?

To date the fundamentals of strained heterostructures have not been elucidated for electrochemical micro-devices. In particular, resistive and capacitive contributions could be altered and triggered over broader ranges and carrier diffusivities and device switch times for different states may be accessed over broader ranges than with classic materials. Interestingly, the majority of reports in the field envision heterostructures as new fast conductive electrolyte materials for micro-solid oxide fuel cells[60,142,149] operating at intermediate temperatures ($\approx$400°C). But, if we carefully analyze literature one can conclude that the difference in conductivity and diffusion coefficient modulation with respect to strain substantially increases for decreasing operation temperature of the device (see *e.g.* Ref.[54] for a computational study and for experimental evidence Refs.[51,79,85]). Therefore, we shift our focus to the new area of memristive information memories and logics and suggest implementing ionic heterostructures as new building blocks for modulating resistive/capacitive contributions of the switches through manipulating the interfacial lattice strain (operating at room temperature), see Ref.[141]. Such devices generally consist of a metal / metal oxide / metal structure. It is imperative to operate the resistive switch with electrodes at small distances, since high local electric field strengths (of the order of $> 10^6$ V/m) are required to observe non-linear hysteretic current-voltage profiles[150].

We suggest replacing the current state-of-the-art single phase metal oxide building block with a multilayer heterostructure made of two metal oxides (*A* and *B*) stacked in a repetitive manner (*i.e. A-(B-A)ₙ-B*) with strained internal interfaces for new types of redox-based resistive switches[141]. The memristive and hysteretic current-voltage characteristics depend on carrier flux. Different resistances can be assigned to binary (or multilevel) states which can be used for digital information storage in new memory devices[39]. Oxide-based resistive switches are a promising alternative to Dynamic Random-Access Memory (DRAM) and non-volatile flash memory used in today's computing and portable data storage devices due

to increased ns-speed operation and low write voltages. These resistive switches could also be used as logic devices and even allow for stacking of multi-terminal cross-bar arrays which is superior to classic transistor based lateral stack concepts[21,22,28,151-153]. In the present paper strain engineering of oxide multilayers is suggested as new strategy to manipulate the properties of metal oxide films. The first strategies to realize such devices in the micro-scale are demonstrated and discussed. Through this approach resistive and capacitive properties of the multilayer oxide can be manipulated by far more than with classic doping in single films. For this, the two metal oxides $Gd_{0.1}Ce_{0.9}O_{2-\delta}$ and Er_2O_3 as constituents of the sideways contacted multilayer micro-dots were selected for implementation as the first future strained resistive switching prototypes. $Gd_{0.1}Ce_{0.9}O_{2-\delta}$ was chosen, since it is a well-studied model material under strain as single phase. In addition, first reports on non-strained ceria-based resistive memories have been reported[154-159]. One may also highlight that the new structuring concept of the heterostructure micro-dots may also be implemented in other electrochemical chip devices such as resistive sensors or catalytic active surface electrodes for batteries or fuel cells.

To this end, we develop a micro-dot device structure for which we establish a new fabrication route to allow for "sideways" and micron-scale contacting of strained multilayer $Gd_{0.1}Ce_{0.9}O_{2-\delta}/Er_2O_3$ dots. Unlike traditional means for varying the resistive characteristics of the metal oxide film by doping, we demonstrate in this study that large changes in the resistive characteristics can be obtained by tuning the interfacial multilayer lattice strain of micron-sized dots in a micro-electrochemical device. Through a variation of the number of multilayer interfaces and the single layer thickness, compressive strain is imposed on the ionic conducting ceria-based phase by the electrically insulating phase of erbia. Lattice strain states are measured for the $Gd_{0.1}Ce_{0.9}O_{2-\delta}$ and Er_2O_3 layers within the heterostructures conventionally by XRD and also by Raman spectroscopy as a new approach for characterizing the near order *via* bond strength changes down to single layer thickness of several nm for heterostructures. We discuss the role of compressive lattice strain, and near order changes with decreasing single layer thicknesses ranging from

275 nm down to *3 nm* ($Gd_{0.1}Ce_{0.9}O_{2-\delta}$) and *7 nm* ($Er_2O_3$) on ionic conductivity for $Gd_{0.1}Ce_{0.9}O_{2-\delta}$ /Er_2O_3 multilayer oxide dots. Furthermore, we elucidate the importance of the newly proposed contacting strategy at micro-distances (*vs.* conventional top electrodes) for strained ionic conducting multilayers over the sides of the micro-device. We also give a proof-of-concept for the electrode design to capture real strain effects in transport. This work presents the first strain-resistance modulation characteristics of heterostructure oxide dots in a micro-device on a chip and provides a basis for a new type of resistive switch.

8   Methods

8.1   Material Synthesis

$Gd_{0.1}Ce_{0.9}O_{2-\delta}$ and Er_2O_3 *single thin films* and *multilayer thin films* composed of the two oxide materials were synthesized in this study.

The thin films were deposited on round single crystalline, double-side polished (0001)-oriented sapphire substrates (Stettler company, Switzerland) by pulsed laser deposition (PLD, Surface Technologies, Germany; KrF excimer laser, 248 nm). Deposition was established at *60 mJ* per pulse at a repetition rate of *10 Hz* for a substrate to target distance of *8.5 cm*. After reaching a background pressure of *$4x10^{-6}$* mbar, the films were deposited at *700°C* and *0.0267 mbar* O_2 pressure. In this study a constant film thickness of *275 nm* was aimed for all samples (single films and multilayers). This corresponds to *14000* pulses for the $Gd_{0.1}Ce_{0.9}O_{2-\delta}$ single film sample, *21000* pulses for the multilayer heterostructure samples and *26000* pulses for the Er_2O_3 single film sample. Subsequent profilometer measurements Dektak XT Advanced profilometer (Bruker, Germany) and SEM cross-sectional analysis were used to verify the constant film thickness within an error of 10% throughout this study. For the multilayer PLD depositions repetitions of $Gd_{0.1}Ce_{0.9}O_{2-\delta}$ and Er_2O_3 single layers were deposited on the sapphire substrates. The single layer thickness of either $Gd_{0.1}Ce_{0.9}O_{2-\delta}$ or Er_2O_3 was varied from *280 (255)* to *7 (3) nm* while the overall film thickness was kept at constant *275 nm*. As a consequence, the number of $Gd_{0.1}Ce_{0.9}O_{2-\delta}/Er_2O_3$ interfaces varied from *5* to *59* within the films; corresponding to a number of single layers of 6 to 60 in the multilayer structures, also denoted as *$(Gd_{0.1}Ce_{0.9}O_{2-\delta}/Er_2O_3)x3$* to *$(Gd_{0.1}Ce_{0.9}O_{2-\delta}/Er_2O_3)x30$*. Substrates were always cleaned in an ultrasound bath with acetone, isopropanol and deionized water prior to film deposition.

Ceramic targets for the pulsed laser deposition, $Gd_{0.1}Ce_{0.9}O_{2-\delta}$ (Praxair, Woodinville, WA) and Er_2O_3 (Sigma-Aldrich, Switzerland), were processed from powders. The targets were uniaxially and then isostatically pressed (*440 bars* for *2 min*) from powder, heated to *1650°C* (Er_2O_3) / *1400°C* ($Gd_{0.1}Ce_{0.9}O_{2-\delta}$) at *5°C/min*, isothermally held for *24h*

(Er_2O_3) / *4h* ($Gd_{0.1}Ce_{0.9}O_{2-\delta}$) and then cooled at *5°C/min* to room temperature. The target phases were characterized by X-ray Diffraction (Bruker D8, $Cu_{K\alpha}$).

8.2 Micro-device and Electrode Preparation - Lithography and Microfabrication

In this experimental part sideways attached electrodes were designed and microprocessed to measure conduction properties along the strained multilayer interfaces for small electrode distances of 15 microns, see Fig. 6. Two challenges had to be considered in the planning: First, multilayers with variable number of interfaces had to be etched under an angle of roughly 80° towards the substrate to subsequently deposit metal electrodes that contact all single layers and strained interfaces over the sides of the micro-device. Next, a 2nd lithography step was required to allow for electrode depositions at 15 microns distance and an overlap of roughly 2 microns between the top of the multilayer film and its side flank. It is to be noted that we report a new micropatterning route for the fabrication of sideways electric contacting of strained multilayer oxides with small scale micro-electrodes.

In the following we detail the experimental fabrication steps for the small-scale "side-plane" micro-electrodes, see schematic in Fig. 6. All steps were carried in an ISO class 4 cleanroom. Multilayer thin films on sapphire samples (Fig. 6a) were subjected in a first step to the shaping of the side flanks and top film area. For this, a foil mask (Selba, Switzerland) and AZ 1518 positive photoresist (Microchemicals, Germany) were used in a 1st photolithography step: the photoresist was spin-coated onto the sample surface at a rotation speed of 4000 RPM for 30 seconds and baked at 100° C for 120 seconds. The samples were then aligned (Karl-Suss MJB3 mask aligner) and exposed through a foil lithography mask to broadband ultraviolet light with a dose of 74 mJ/cm^2 (Fig. 6b). The pattern was developed using MIF 726 developer (Microchemicals, Germany). After the first pattern of regularly distributed photoresist islands was made on the samples the ceramic thin film was dry-etched using argon ion (Ar^+) sputtering (Oxford Instruments

Plasmalab 80) (Fig. 6c). Subsequently, the remaining photoresists was removed using acetone. In order to get well defined electrodes a 2nd photolithography step similar to the first one was done using AZ nLOF 2070 (1:0.4) negative photoresist (Microchemicals, Germany) The samples were spinned at a speed of 4750 RPM for 45 sec, then softbaked at 110°C for 90 sec. The second photoresist pattern was aligned over the ceramic micro-dots by visual alignment overlapping 2 microns with the help of alignment marks. Then they were exposed to a light dose of 210 mJ/cm^2 and subsequently the photoresists was subject to another heating step at 110°C for 180 sec (Fig. 6d). Finally the pattern was developed using the MIF 726 developer.

In the last step metal electrodes constituting of Ti 25nm/Pt 150 nm were deposited *via* electron beam evaporator (Plassys MEB 550, France). Ultimately, the samples were soaked in acetone until the remaining photoresist was stripped off, as determined by visual inspection. The height profile of the micro-dot island was investigated by optical surface profilometry (Sensofar Plu neox, Spain).
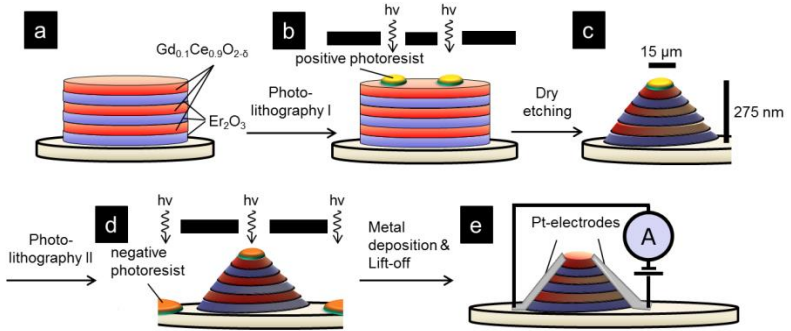
Figure 8.1: Schematic thin film and microfabrication process flow for $Gd_{0.1}Ce_{0.9}O_{2-\delta}/Er_2O_3$ multilayer micro-dots. a) Laser ablated multilayer thin film on an oriented sapphire substrate. b) A pattern of photoresist dots was structured on the surface (1st positive photolithography step). c) Ar^+ sputtering was applied to 3D-shape the multilayer thin films. d) Photoresist pattern for electrodes are shaped (2nd negative photolithography step) e) Pt metal contacts deposition on the side walls of the single and multilayer thin films. The dimensions are not to scale.

8.3   Chemical and Structural characterization

The as-deposited single and multilayer films were characterized by X-ray Diffraction (Bruker D8) at a *Cu K_α* wavelength. Raman spectroscopy was performed using a confocal WITec CRM200 Raman microscope instrument equipped with a 532 nm wavelength laser for excitation and a spectral resolution of 0.7 cm^{-1}. Fitting was done by OriginPro 9.1 using a Gaussian function. The error of the fit ranges from 0.14 to 0.017%. One fit is depicted exemplarily in Fig. 3b. Materials were characterized with a scanning electron microscope (SEM, LEO 1530, Germany) to analyze the microstructures.

8.4   Electric characterization

DC 4-point electric conductivity measurements *of the thin film micro-device structures* were performed in air using the Keithley 2601B multimeter for kinetic measurements with applied DC voltage amplitude

of *1 V*. The *thin film* micro device structures were contacted with tungsten microprobe tips in a custom fabricated microprobe station (Everbeing, Taiwan and Electrochemical Materials ETH Zurich, Switzerland) with a sealed air atmosphere environment, equipped with stereomicroscopy. The temperature was varied during the measurements between room temperature and 585°C at heating/cooling rates of *5°C/min*. To get kinetic reference data measurements were done on bulk pellets contacted by Pt paste and wire in a tube furnace. The temperature range was from room temperature to 1000°C with heating/cooling rates of *5°C/min*.

9   Results and Discussion

9.1   Fabrication of Strained Oxide Micro-Devices on a Chip

Microscopy images and schematics of the micro-device structures consisting of strained multilayer $Gd_{0.1}Ce_{0.9}O_{2-\delta}$ /Er_2O_3 thin film dots with pairs of sideways Pt contacts arranged in an array are presented in Figure 9.1. The light microscopy top-view shows the successfully fabricated array of Pt electrode pairs contacting a strained multilayer erbia/gadolinia-doped ceria dot at low magnification (Figure 9.1a). At higher magnification, a free etched erbia/gadolinia-doped ceria multilayer dot structure is visible as a square shaped area with an edge length of ~15 μm in interference colors arranged between two Pt electrodes (Figure 9.1b). Laterally resolved Raman spectroscopy was used to verify that the structured multilayer films were completely free-etched dots with no remains on the substrate. For this, the characteristic vibrational modes with respect to the spot on the chip were analyzed as detailed in Supporting information 23.1. A requirement of this work is to deposit and shape Pt micro-electrode pairs which allow for electric contacting of each multilayer film island structure along all of its strained interfaces and at short electrode distances, see schematic in Figure 9.1c. For this, a regular pattern of Pt electrodes was deposited onto the free-etched multilayer film islands. The Pt electrodes overlap the island so that the metal contacts the multilayer thin film island at its sloping side walls (Figure 9.1b: schematic, Figure 9.1d: 3D optical profiles). A SEM image of the multilayer film's cross-sections is shown in Figure 9.1e. For the image recorded with the backscatter detector the different single layer phases of the multilayer oxide film can be visualized by their difference in atomic mass. Here, bright contrast refers to the more strongly backscattered electrons of the heavy erbium-oxide single layers and darker ones to the lighter ceria single layers. The selected multilayer shows a thin film with *290 nm* in total film thickness and a set of 3 bilayers of $Gd_{0.1}Ce_{0.9}O_{2-\delta}$ and Er_2O_3 (*i.e.* the number of $Gd_{0.1}Ce_{0.9}O_{2-\delta}$/$Er_2O_3$ interfaces is 5). A single layer thickness of *~35 nm* of Er_2O_3 and *62 nm* of $Gd_{0.1}Ce_{0.9}O_{2-\delta}$ can be

determined from the cross-section and is in good agreement with the intended pulsed laser deposition processing conditions of 32 nm and 64 nm for Er_2O_3 and $Gd_{0.1}Ce_{0.9}O_{2-\delta}$, respectively. All films deposited throughout the study revealed comparable film thicknesses within an error of ±10% and revealed continuous and dense film microstructures.

In this part, we present a first new strategy to prepare *sideways contacted multilayer oxide thin film dot arrays* to measure along the strained interfaces for small electrode distances of *≤ 15 microns*. This differs to classic contacting strategies for ionic conducting and strained multilayer oxides in the sense that top in-plane electrode measurements have been avoided and electrode distances were reduced by more than 2 orders of magnitude.

In the following, the crystallographic structures, near order and bond length (representative of bond strength) and ionic conductivity characteristics of $Gd_{0.1}Ce_{0.9}O_{2-\delta}/Er_2O_3$ multilayers and single films are presented as a function of number of interfaces and lattice strain. The role of the interfacial lattice strain and its interaction volume on the ionic conductivity of the fast conducting $Gd_{0.1}Ce_{0.9}O_{2-\delta}$ phase is next investigated for the multilayer dot micro-device structures.
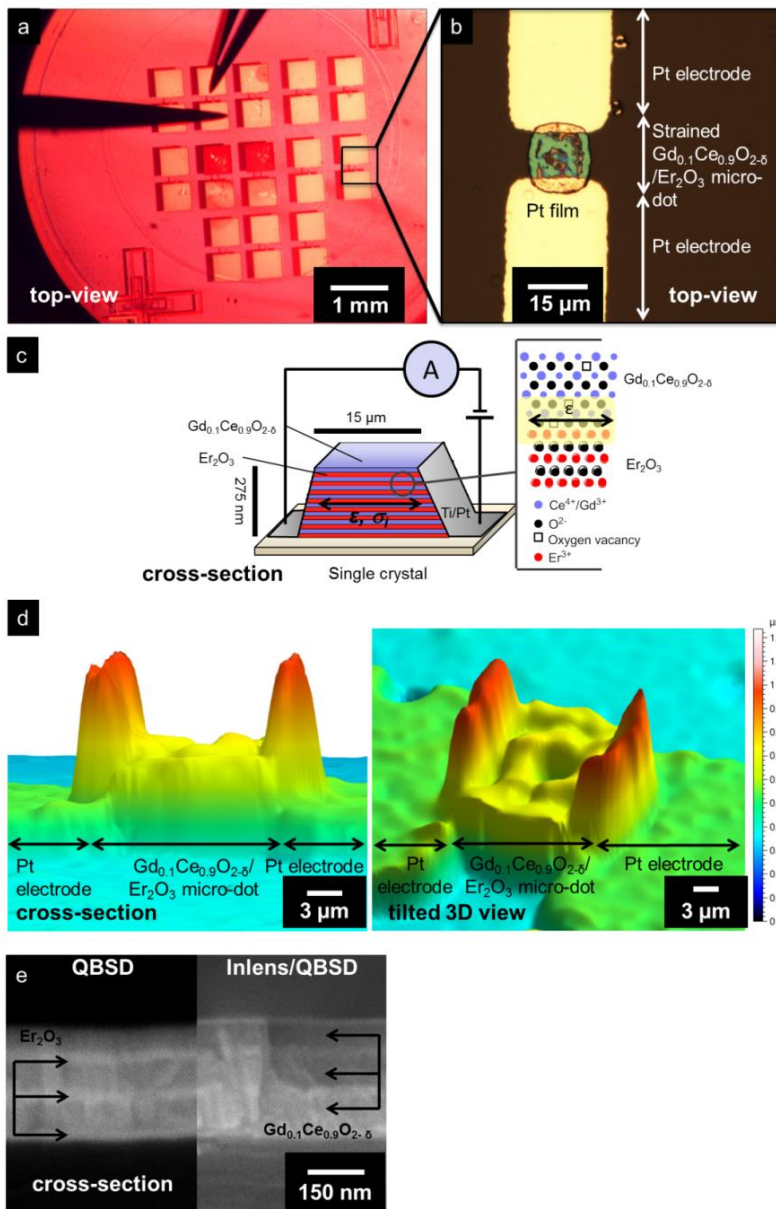
Figure 9.1: Microscope view-graphs of strained $Gd_{0.1}Ce_{0.9}O_{2-\delta}/Er_2O_3$ multilayer micro-dots and arrays on chip.a) Top view low magnification light microscopy image of an electrode array contacting through the sides islands of $Gd_{0.1}Ce_{0.9}O_{2-\delta}/Er_2O_3$ multilayer micro-dots on chip. Tungsten needles were used for electric contacting of the Pt-side contacts. b) High magnification light microscopy image of Pt electrodes contacting a structured multilayer thin film dot (top view). c) Schematic view graphic of a strained multilayer $Gd_{0.1}Ce_{0.9}O_{2-\delta}/Er_2O_3$ heterostructure. The electrodes that are attached to the side walls of the structure allow measuring the conductivity parallel to the strained $Gd_{0.1}Ce_{0.9}O_{2-\delta}/Er_2O_3$ interfaces. d) Side view and tilted 3D view for a micro-dot arranged between two metal electrodes by optical surface profilometry. Here, the scale bar refers to the horizontal width (aspect ratio is not to scale). The color bar indicates the measured heights. e) SEM cross-sectional view of a $Gd_{0.1}Ce_{0.9}O_{2-\delta}/Er_2O_3$ multilayer in a micro-dot. The left side shows a QBSD image and the right side shows a 50% QBSD and 50% In-lens detector image. In the QBSD image the bright contrast phase refers to the Er_2O_3 (heavy mass) and the dark one to the $Gd_{0.1}Ce_{0.9}O_{2-\delta}$ (light mass).

9.2 Lattice Structure and Strain State of the $Gd_{0.1}Ce_{0.9}O_{2-\delta}$/$Er_2O_3$ Multilayer Thin Films

The X-ray diffraction patterns of the single Er_2O_3 and $Gd_{0.1}Ce_{0.9}O_{2-\delta}$ films and of $Gd_{0.1}Ce_{0.9}O_{2-\delta}$/Er2O3 multilayer thin films with a varying number of thin films interfaces from 5 to 59 [($Gd_{0.1}Ce_{0.9}O_{2-\delta}$/ Er_2O_3)x30] are displayed in Figure 9.2. Detailed information on the XRD scans is available in Supplementary information 23.2. The diffractograms of the reference single film samples of Er_2O_3 and $Gd_{0.1}Ce_{0.9}O_{2-\delta}$ show single peaks for the first and second order; being the orientations (111) and (222) for $Gd_{0.1}Ce_{0.9}O_{2-\delta}$ and (222) and (444) for Er_2O_3, Figure 9.2a. The $Gd_{0.1}Ce_{0.9}O_{2-\delta}$ single film reveals a cubic fluorite structure with a measured lattice parameter of 0.5430 nm, Figure 9.2b. The (111) orientations observed for the $Gd_{0.1}Ce_{0.9}O_{2-\delta}$ films are in agreement with literature[118,160]. A cubic bixbyite structure with a lattice parameter of 1.061 nm was determined for the Er_2O_3 single film. The single film phases and structure types agree with own processed and measured reference ceramic pellets (see Supplementary information 23.3). Further, this is in agreement with literature, see for details on $Gd_{0.1}Ce_{0.9}O_{2-\delta}$ Ref.[140,161] and for Er_2O_3 Ref.[162]. It can be concluded that the two materials grow in a 1:2 commensurability in lateral view: The orientation of the (0001) sapphire imposes biaxial texture on the single film compounds. The XRD patterns of the single films are compared to multilayer films of $Gd_{0.1}Ce_{0.9}O_{2-\delta}$/$Er_2O_3$ with varying numbers of interfaces from 5 to 59 and a decreasing single layer thickness from 280 to 7 nm (255 to 3 nm for Er_2O_3). The total thickness of the multilayers was kept constant at approximately 275 nm. All multilayer thin films show the (111) $Gd_{0.1}Ce_{0.9}O_{2-\delta}$ and (222) Er_2O_3 signature peaks as well as their higher orders. Hence, a successful orientation and biaxial texturing of the individual single layers in the multilayer towards the (0001) sapphire substrate can be concluded. We observe this independently on the number of interfaces and down to a single layer thickness of *18 nm*. Based on the diffraction data in growth direction we conclude that the best match for the multilayer growth of the thin film materials is realized in the (111) and (222) orientation for $Gd_{0.1}Ce_{0.9}O_{2-\delta}$ and Er_2O_3 according to the trifold symmetry of the (0001) direction of the (0001) sapphire substrate. Hence,

out of geometrical considerations the trifold symmetry of the (111) plane of Er_2O_3 should correspond to the best match with the trifold symmetry with a *4:3* lattice spacing commensurability in the multilayer.

In general, we observe systematic shifts of the (111) $Gd_{0.1}Ce_{0.9}O_{2-\delta}$ peak towards lower and for the (222) Er_2O_3 peak towards higher diffraction angle with increasing number of multilayer interfaces from 5 to 13. For higher numbers of multilayer interfaces, erbia and gadolinia-doped ceria (111) and (222) peaks overlap as the shifting progresses (resp. for single layer thicknesses *18 nm*), Figure 9.2a. We interpret this as characteristic features of superlattices with the mean structure peaks surrounded by satellite peaks, in agreement with Refs.[163,164]. Similar observations have been made in earlier studies on ionic heterostructures of ceria / 8 mol% yttria-stabilized zirconia by Pergolesi[71] for single layer thicknesses of *9 nm*. The angular positions of the satellite peaks were used to calculate the bilayer thickness, according to the following equation[71]:

$$\Lambda = \lambda/(sin_{\theta+1} - sin_{\theta-1}) \hspace{3cm} Equation\ 9.2.1$$

where Λ is the bilayer thickness and $sin_{\theta+1}$ and $sin_{\theta-1}$ are the positions of the first-order satellite peaks of the superlattice. The resulting $Gd_{0.1}Ce_{0.9}O_{2-\delta}/Er_2O_3$ bilayer thickness is $\Lambda_{Gd_{0.1}Ce_{0.9}O_{2-\delta}/Er_2O_3} = 10$ nm, which is in very good agreement with the profilometer measurements.

In Figure 9.2b the out-of-plane lattice constants are shown calculated out of clearly resolved Bragg reflections of the multilayers with 5 to 13 interfaces. The lattice constant of $Gd_{0.1}Ce_{0.9}O_{2-\delta}$ is increased as the thickness of the individual layers is decreased while the lattice constant of Er_2O_3 is decreased for a decreasing thickness of the individual layers. The values of these out-of-plane lattice constants are in good agreement with the lattice constants reported in literature[165,166]. The out-of-plane lattice constants show an expansion of the lattice for $Gd_{0.1}Ce_{0.9}O_{2-\delta}$ and a compression of the Er_2O_3 lattice, and reverse behavior can be expected for the in-plane lattice strain. This means it can be expected that the unit cells relax the strain that is imposed on them along the in-plane-direction in the out-of-plane-direction[167].
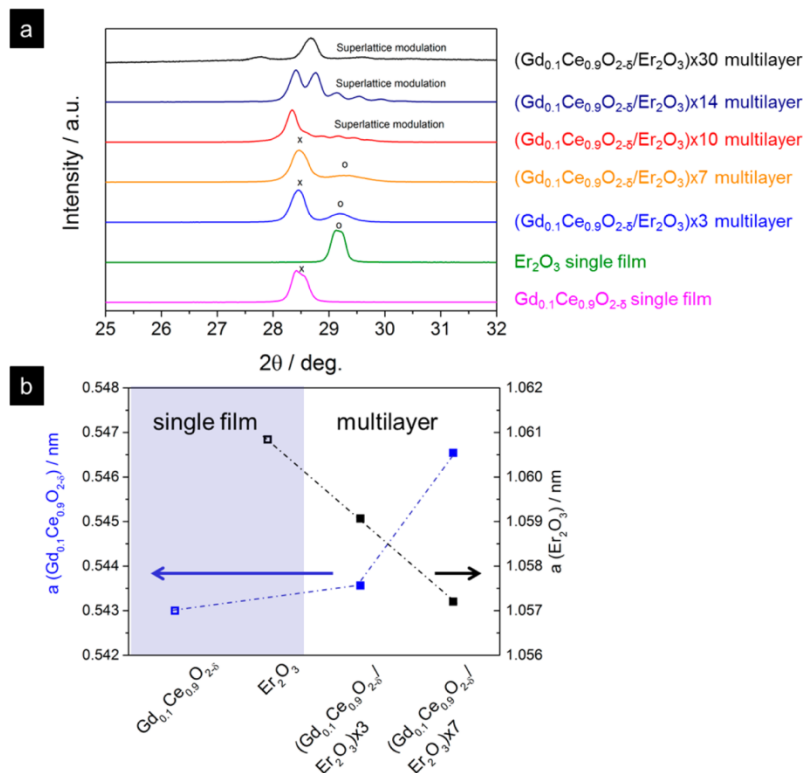
Figure 9.2: XRD measurements of the Er_2O_3 and $Gd_{0.1}Ce_{0.9}O_{2-\delta}$ single thin films and multilayer thin films. a) The diffractograms show clearly crystalline and textured thin films. The samples with high number of interfaces, 10 to 30 bilayers (19 to 59 $Gd_{0.1}Ce_{0.9}O_{2-\delta}/Er_2O_3$ interfaces), and show additional satellite peaks, indicating superlattice modulation. The sign (x) refers to $Gd_{0.1}Ce_{0.9}O_{2-\delta}$[52] and the sign (o) refers to Er_2O_3.[53] b) Comparison of the out-of-plane lattice parameters with respect to the number of interfaces for the $Gd_{0.1}Ce_{0.9}O_{2-\delta}$ and Er_2O_3 single films and the multilayer thin films for $(Gd_{0.1}Ce_{0.9}O_{2-\delta}/Er_2O_3)x3$ and $(Gd_{0.1}Ce_{0.9}O_{2-\delta}/Er_2O_3)x7$. Total film thickness was kept constant at 275 nm.

9.3 Implications of the Lattice Strain on Cationic-Anionic Near Order in the Multilayers

We investigated the near-order and bond strength characteristics of the single films and multilayers *via* Raman spectroscopy. This allows direct probing of the *Ce–O* bond and is therefore very sensitive to changes in the bonding environment. Literature review shows that for the case of Er_2O_3 data is available on single crystalline material[168,169], however, reports on thin film erbia are missing. More data is available for $Gd_{0.1}Ce_{0.9}O_{2-\delta}$ pellets. Nevertheless reports on thin films are still scarce[139,170,171]. First work on the implication of lattice strain on the gadolinia-doped ceria Raman near order has been recently published[139]. Very recently, Kreisel[114] reported the use of Raman spectroscopy as a probing tool to characterize the strain states of four oxide films for varying penetration depth. It is surprising that Raman near order-strain studies are still lacking for thin films based on metal oxides, despite their established use for covalently bonded materials under strain[147,148]. In Figure 9.3, spectra for the *single thin films* and *$Gd_{0.1}Ce_{0.9}O_{2-\delta}$/$Er_2O_3$ multilayers* are displayed. The reader is referred to Table 9.1 for Raman mode assignments.

Single film spectra reveal the following characteristics: The spectrum of the $Gd_{0.1}Ce_{0.9}O_{2-\delta}$ single film sample shows one single peak at about *463 cm^{-1}*, Figure 9.3a. This peak can be assigned to the F_{2g} mode in accordance to literature on similar materials processed as macrocrystalline ceramics. This is further consistent with recent reports on Raman characteristics of $Gd_{0.2}Ce_{0.8}O_{2-\delta}$ PLD thin films[139,172,173]. The spectrum of the Er_2O_3 single thin film reveals 8 measurable Raman active modes. Latter Raman peaks can clearly be assigned to the coupled F_g+A_g and F_g modes[168] of erbia and other rare earth bixbyite structures (Sm_2O_3, Dy_2O_3, Mn_2O_3, Sc_2O_3, In_2O_3)[174], Figure 9.3a and Table 9.1. We also compare and confirm through own macrocrystalline doped ceramic standards the assigned peaks for the single thin films (see Supplementary Information 23.4). Both single thin film samples, erbia and doped ceria, show additional peaks assigned as "*s*" originating from the sapphire substrate.

Multilayer $Gd_{0.1}Ce_{0.9}O_{2-\delta}$/$Er_2O_3$ films are also displayed relative to their number of interfaces for their Raman characteristics in Fig. 3a. All multilayers investigated exhibited additional peaks compared to the single

films. However, all multilayer spectra are very similar with the same number of peaks independent on the number of single layers. Therefore relative changes between these spectra were investigated in detail.

A peak at about *455 cm^{-1}* can be observed that could be the F_{2g} mode of the $Gd_{0.1}Ce_{0.9}O_{2-\delta}$ component. All other peaks (at higher wavenumbers, *i.e. > 460 cm^{-1}*) are tentatively assigned to the F_g or other modes of the Er_2O_3 phase. The peak at *~500 to ~510 cm^{-1}* appears to be a double peak as observable in earlier studies on strained GaN[147], which is attributed to strain- or orientation-induced mode splitting. However, the peaks are broadened ($FWHM_{singlefilm} = 28$ cm^{-1}) due the nano-crystalline morphology of the films, and so it remains unclear exactly how many lines are in the region ranging from ~400 to 600 cm^{-1} and to which Raman modes they correspond. Furthermore, the modes of the sub-10nm layers are likely shifted due to phonon confinement effects. Therefore, direct comparison of the peak position of the single film and multilayer spectra is not possible without extensive simulations. However, from careful analysis of the multilayer sample Raman spectra we can observe a systematic trend within the multilayer samples. To obtain the superposed Raman peak signatures of the multilayers, we apply Gaussian fit algorithms. The fit of the superposed Raman signatures is exemplarily shown for a sample of the 19 interfaces $Gd_{0.1}Ce_{0.9}O_{2-\delta}/Er_2O_3$ multilayer sample (Figure 9.3b). For the peak fitting algorithm the peak width was left as a free parameter due to the fact that peaks of different materials and morphologies were fitted and that the peaks could not be assigned beyond doubt. A schematic of the measurement principle is shown in Fig. 3c. Here, the principles of XRD and Raman are compared and related to the state at the interface and lattice strain tensor components measured. Dilatational lattice strain can act in three directions of space, denoted ε_{11}, ε_{22} and ε_{33}. The vectors ε_{11} and ε_{22} form the plane along the multilayer interface of the two adjacent materials with ε_{33} as the out-of-plane component being perpendicular to it. Using Raman confocal microscopy in first approximation the direction parallel to the incident beam is measured (neglecting crystal orientation, the numerical aperture of the objective and the refractive index of the sample). In the backscatter configuration the incident excitation beam is perpendicular to the surface and, hence in a cubic crystal with $\varepsilon_{33} \parallel$ <001> the measured direction is

directly proportional to the ε_{33} direction (Figure 9.3c). However, in the generalized case Raman spectroscopy is sensitive to all modes with eigenvector components parallel to the beam, which are related to in-plane strain components *via* the out-of-plane component ε_{33} and the stiffness tensor c_{ij}. In the present work, the <111> out-of-plane texture invokes a mixing of modes with out-of-plane components. Consequently, a mode splitting would be expected, but due to the broad line-width of our films, the resulting spectra rather show an additional broadening and shift due to strain[175]. The overall shift of the assigned F_{2g} line is recorded by fitting and qualitatively interpreted as strain shift.

The same strain tensor component (ε_{33}) is accessed for XRD in Bragg-Brentano configuration. In Fig. 3d we summarize the change of Raman shift within the $Gd_{0.1}Ce_{0.9}O_{2-\delta}/Er_2O_3$ multilayer samples. The peaks chosen for analysis were the F_{2g} line (tentative assignment) of $Gd_{0.1}Ce_{0.9}O_{2-\delta}$ at ~455cm^{-1} and the F_g line at *~520 cm^{-1}* for Er_2O_3. The following observations can be made:

Increasing the number of interfaces and decreasing the single layer thickness of the multilayers results in Raman peak shifts within the compressively-strained ceria and tensely strained erbia $| \varepsilon_{11} \times \varepsilon_{22} |$ planes: For an increasing number of interfaces the F_{2g} Raman mode of ceria blue-shifts by *1.3 cm^{-1}* (for increase from 5 to 59 interfaces). At the same time, the Raman erbia F_g mode red-shifts by *1.5 cm^{-1}*. Using this strain-induced shift one can use the data provided by high-pressure studies[176] to estimate the strain in the heterostructure[175], although we would like to note that strain in thin films cannot be directly compared to hydrostatic pressure. Regarding the elastic modulus used for the calculations one can use the bulk values for gadolinia-doped ceria[177,178], resulting in change of the strain value of ~0.1%. But Kossoy[179] reported that the elastic modulus of thin films is more than one order of magnitude smaller than the value observed in bulk samples, resulting in change of the strain value of ~1.16% within the multilayer samples. For future discussions we will refer to the value estimated with the thin film elastic modulus.

We interpret this finding as lattice strain originating from the interfaces and relaxing over the thickness of each single layer. Therefore, thinner individual layers lead to increased strain at the heterointerfaces. This

occurs for increased volume fractions of strained single layers when increasing the interface numbers within the multilayered samples. This is in agreement with the data obtained by XRD.

Such behavior was predicted for the Yttria-stabilized zirconia system in density functional theory (DFT) and nudged elastic band (NEB) computational studies[54]. Earlier experimental studies reported the cationic order (measured by XRD) to be inconsistent on the single layer thickness or number of interfaces within the experimental error[51] whereas in the present case the trends are consistent within the $Gd_{0.1}Ce_{0.9}O_{2-\delta}$ /Er_2O_3 multilayer samples. Obtaining absolute values of the strain-induced Raman line shifts by comparing the Raman spectra of the multilayer samples with the samples of the single films was not possible due to the restrictions mentioned above.

Using this knowledge and data obtained by a high-pressure Raman study and general Raman theory a strain shift increasing the compressive in-plane strain in the $Gd_{0.1}Ce_{0.9}O_{2-\delta}$ and an increasing tensile in-plane shift for Er_2O_3 can be deduced.

In the given multilayer systems a decrease of single layer thickness of the $Gd_{0.1}Ce_{0.9}O_{2-\delta}$ phase increases the overall strained volume and the magnitude of strain as reported in the structural near order investigations, Figure 9.3. Through the following we study how the lattice strain affects the activation energy of conductivity for the multilayer micro-dots.
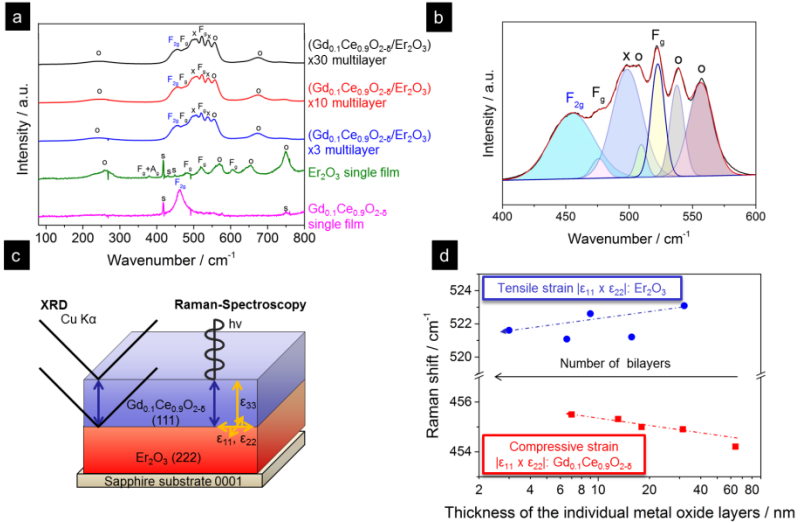
Figure 9.3: Near order Raman analysis of the Er_2O_3 and $Gd_{0.1}Ce_{0.9}O_{2-\delta}$ single thin films and multilayer thin films. a) Raman spectra of the $Gd_{0.1}Ce_{0.9}O_{2-\delta}$ and Er_2O_3 single and multilayer thin films. The blue index indicates the F_{2g} mode of $Gd_{0.1}Ce_{0.9}O_{2-\delta}$ and the black F_g labels Er_2O_3. The (x) indicates unknown peaks, (o) identified ones to similar bixbyite structures. The peak assignments of the multilayer samples are tentative assignments. b) Example of a Gaussian fit for the Raman spectra of a $(Gd_{0.1}Ce_{0.9}O_{2-\delta}/Er_2O_3)x10$ multilayer sample (tentative assignments). c) Schematic view of the XRD and Raman measurement directions relative to the strained multilayer interface. The individual contributions of strain are shown by orange arrows. d) Relative Raman wavenumber shift within multilayers film samples with respect to the individual metal oxide single layer thickness within Er_2O_3 and $Gd_{0.1}Ce_{0.9}O_{2-\delta}$ multilayers. The line of Er_2O_3 at ~520 cm^{-1} is shown in blue, the line at ~455 cm^{-1} of $Gd_{0.1}Ce_{0.9}O_{2-\delta}$ is shown in red. These peaks were used for data analysis. The in-plane strain is tensile for Er_2O_3 and compressive for $Gd_{0.1}Ce_{0.9}O_{2-\delta}$. The change of near order is measurable with increasing number of multilayers and strain at the interface. Total film thickness was kept constant at 275 nm.

Table 9.1: Assignment of the observed Raman peaks. The peak positions are indicated in the first column and the peaks are assigned to Raman modes, if possible. Otherwise the peaks are matched with Raman spectra of Rare earth oxides that crystallize in bixbyite structure.

Peak (app.) / cm^{-1}	GDC pellet	Er_2O_3 pellet	GDC single film	Er_2O_3 single film	Assignment	Ref
230		x		x	Match w. Sc_2O_3	[174]
250		x		x	Match w. Sm_2O_3	[174]
380		x		x	$F_g + A_g$	[168]
465	x		x		F_{2g} of GDC	[172]
480		x		x	F_g of Er_2O_3	[168]
520		x		x	F_g of Dy_2O_3	[168]
560		x		x	Match w. Mn_2O_3	[174]
600		x		x	F_g of Er_2O_3	[168]
660		x		x	Match w. Mn_2O_3	[66]
750		x		x	Match w. Sm_2O_3	[66]

9.4 Impact of Lattice Strain on Electric Transport Characteristics of $Gd_{0.1}Ce_{0.9}O_{2-\delta}$/$Er_2O_3$ Multilayer for Side-Plane Contacted Micro-Dot Device

The temperature dependence of conductivity was analyzed in Arrhenius plots for sideways contacted single and multilayer dots with respect to the strain activated volumes of the conductor, as shown in Figure 9.4a. The $Gd_{0.1}Ce_{0.9}O_{2-\delta}$ *single film* shows the highest conductivity with an activation energy of 0.75 eV in accordance with Refs.[138,139,180]. Increasing the number of $Gd_{0.1}Ce_{0.9}O_{2-\delta}$/$Er_2O_3$ interfaces and reducing the single layer thickness (down to 7 nm) for the small band gap $Gd_{0.1}Ce_{0.9}O_{2-\delta}$ results in an increase of ionic activation energy. The activation energy of conductivity is increased from 0.75 eV for the single film to 1.06 eV for the 59 interfaces sample, a change of activation energy $\Delta E_a = \Delta 0.31$ eV for ~1.16% compressive strain imposed by the erbia phase of the multilayer on the $Gd_{0.1}Ce_{0.9}O_{2-\delta}$, Figure 9.4b and c. This trend is consistent throughout all multilayer samples. We attribute the increase in activation energy of ionic migration for the imposed compressive strain of erbia to the increased pressure acting on the strain activated volumes on the $Gd_{0.1}Ce_{0.9}O_{2-\delta}$ in consistency with Equation 9.5.7 - Equation 9.5.9. This corresponds to a change in enthalpy of oxygen migration of 0.31 eV for the strained $Gd_{0.1}Ce_{0.9}O_{2-\delta}$ phases of the multilayer according to the model expressed in Equation 9.5.9. Further, the inset of Figure 9.4b shows the contacting strategy necessary to obtain measured data along the strained $|\ \varepsilon_{11} \ x \ \varepsilon_{22}\ |$ $Gd_{0.1}Ce_{0.9}O_{2-\delta}$ layers. Figure 9.4c displays the decrease of ionic conductivity while minimizing the thickness of the individual $Gd_{0.1}Ce_{0.9}O_{2-\delta}$ single layers and maximizing the strain volume for the ceria-phase. It can be concluded that a clear impact of the compressively strained volumes of the small band gap conductor on its ionic transport is reported for sideways contacted micro-dot structures. Accordingly, we summarize in Figure 9.4d that all strained ceria-based single layers contribute to the overall transport of the micro-dot structures through the pathways P1+P3 outlined in the circuit model. The insulating wide band gap erbia single layers of the dot do not contribute with the path ways P2+P4, but act as strain modulators of the ceria-phase for the micro-dot.
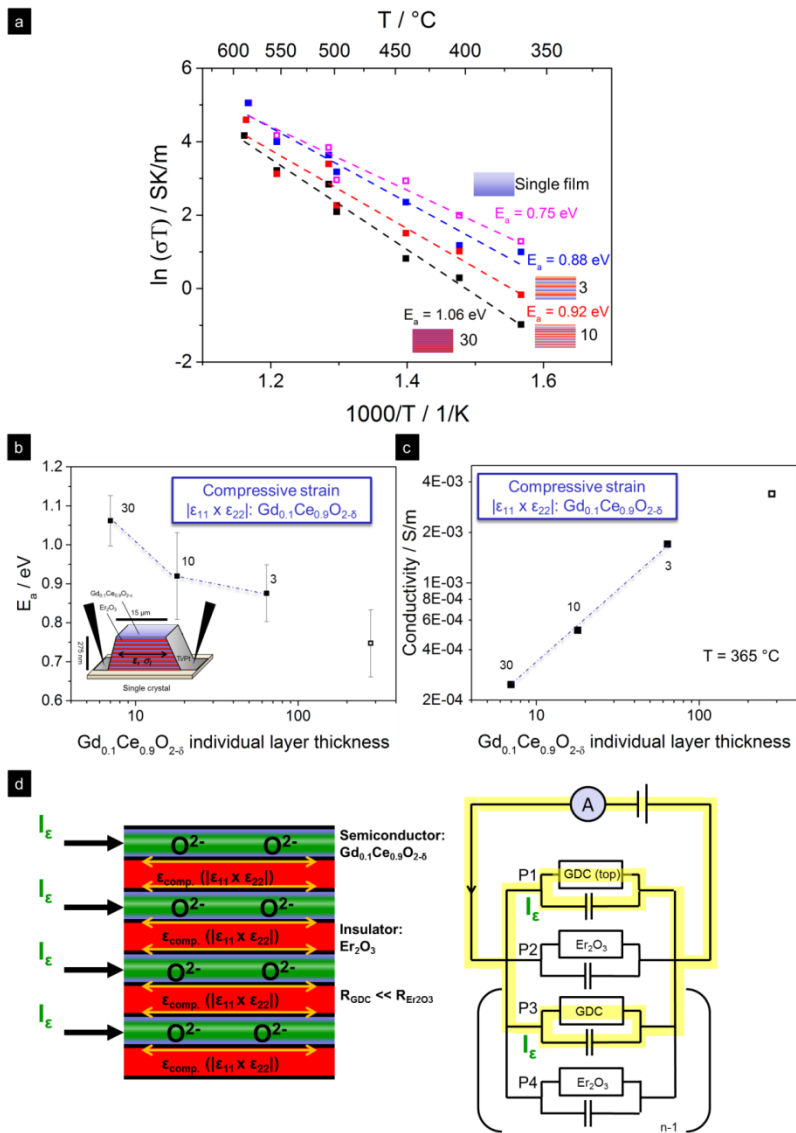
Figure 9.4: Ionic conductivity for the sideways contacted and strain modulated $Gd_{0.1}Ce_{0.9}O_{2-\delta}/Er_2O_3$ multilayer micro-dots. a) Arrhenius plot of the conductivity for $Gd_{0.1}Ce_{0.9}O_{2-\delta}$ single thin film vs. $Gd_{0.1}Ce_{0.9}O_{2-\delta}/Er_2O_3$ multilayer thin film micro-dots for sideways contacting. The numbers next to the specimens indicate the number of bilayers. b) Activation energy with respect to the thickness of the individual single layer thickness of $Gd_{0.1}Ce_{0.9}O_{2-\delta}$. The measurement setup is shown in the inset. The total change of activation energy is $\Delta 0.31$ eV. The inset shows the measurement setup that allows measurement of the whole multilayer structure. c) Plot of electric conductivities of the $Gd_{0.1}Ce_{0.9}O_{2-\delta}$ single thin film and $Gd_{0.1}Ce_{0.9}O_{2-\delta}/Er_2O_3$ multilayer thin films with respect to the thickness of $Gd_{0.1}Ce_{0.9}O_{2-\delta}$ for 585°C. The open symbol refers to the single film. d) Schematic view graphic on conduction pathways and electronic circuit model for the $Gd_{0.1}Ce_{0.9}O_{2-\delta}/Er_2O_3$ multilayer micro-dots. Left: Model of the current flow in the specimen for $R_{GDC} << R_{Er2O3}$. Here, the ionic current flows through all semiconducting layers of the $Gd_{0.1}Ce_{0.9}O_{2-\delta}$ phase. The Er_2O_3 phase does not contribute to the electric conductivity, but serves as phase to tune the compressive strain acting on the $Gd_{0.1}Ce_{0.9}O_{2-\delta}$ phase of the micro-dot structure. Right: Equivalent circuit model and ionic pathways of the micro-dot device. The yellow shading indicates the flow of the ionic current along P1+P3 and strain modulation within the $Gd_{0.1}Ce_{0.9}O_{2-\delta}$ RC circuit elements of a micro-dot. Blocking for the strain modulating pathways P2+P4 is indicated. Total thin film structure thickness was kept constant at 275 nm.

9.5 Defect Thermodynamic Model for Strain-Modulated $Gd_{0.1}Ce_{0.9}O_{2-\delta}$/$Er_2O_3$ Multilayer Micro-Dot Device Structures

In the following, we discuss the concept of sideways contacted $Gd_{0.1}Ce_{0.9}O_{2-\delta}$ and Er_2O_3 multilayer micro-dots in their ionic transport characteristics for modified interfacial strains. For a multilayer micro-dot, the gadolinia-doped ceria single layers represent the small band gap phase with a band gap of 3.1 eV[125] and a predominantly oxygen ionic conductivity with an activation energy of ionic conductivity of ~0.75 eV in air for bulk[180]. On the other hand the erbia single layers of the multilayer dots are the wide band gap phase with a band gap of 7.6 eV[181] and an ionic activation energy of ~1.6 eV in air for bulk[128]. Based on bulk transport data, it is to be expected that the erbia single layer phases block the electric field lines for sideways contacting in the multilayer. The current is carried by the ionic conducting $Gd_{0.1}Ce_{0.9}O_{2-\delta}$ single layers of the multilayer micro-dot for sideways electrode arrangements measuring along the strained interfaces. The erbia's sole function in the multilayer is to modify the interatomic distances locally at the interface by imposing a compressive strain on the ionic current carrying $Gd_{0.1}Ce_{0.9}O_{2-\delta}$ phase. We keep the film thickness in all experiments constant and vary systematically the number of interfaces and single layer thicknesses of $Gd_{0.1}Ce_{0.9}O_{2-\delta}$ and Er_2O_3 phases in the multilayers. Consequently, we consider that due to big differences in the conductivity of the two materials either the $Gd_{0.1}Ce_{0.9}O_{2-\delta}$ or the interfaces are relevant for the conduction while the bulk Er_2O_3 phase is an electric insulator and only serves as matrix to achieve the desired strain state variation in the $Gd_{0.1}Ce_{0.9}O_{2-\delta}$ (GDC) phase by the lattice misfit of the two adjacent materials: The lattice misfit f between the two materials, erbia and gadolinia-doped ceria with the lattice constants a_{Er2O3} and a_{GDC}, in the following denoted as a_ε (since the $Gd_{0.1}Ce_{0.9}O_{2-\delta}$ phase is the conducting phase under strain) with respect to erbia is defined as

$$f = \frac{a_{Er_2O_3} - a_\varepsilon}{a_{Er_2O_3}}$$

Equation 9.5.1

and gives a numerical value of the theoretical lattice misfit of 2.74%, acting compressively on the $Gd_{0.1}Ce_{0.9}O_{2-\delta}$ single layers The ionic conduction of the latter small band gap phase is described by an oxygen ion hopping mechanism via oxygen vacancies[182], which are the predominant charge carrier introduced through doping, as shown in Equation 9.5.2.

$$Gd_2O_3 \xrightarrow{CeO_2} 2Gd'_{Ce} + 3O_O^x + V_O^{\bullet\bullet}$$

Equation 9.5.2
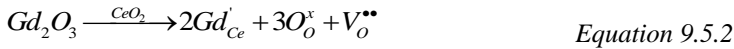
The wide-band gap phase erbia reveals p-type conduction as predominant mechanism in air[128]. The predominant fast ceria-based ionic conductivity, σ_{ionic}, of the multilayer micro-dot for measurement along the interfaces is given by:

$$\sigma_{ionic}(T) = (2q)\left[V_o^{\bullet\bullet}\right]\upsilon_i = (2q)\left[V_o^{\bullet\bullet}\right]\frac{\upsilon_{0i}}{T}\exp\left(-\frac{\Delta H_{mig}}{k_B T}\right)$$

Equation 9.5.3

2q represents the charge of an oxygen vacancy, $\left[V_O^{\bullet\bullet}\right]$ refers to the oxygen vacancy concentration, υ_i stands for the ionic mobility, υ_{0i} is the pre-exponential ionic mobility factor, ΔH_{mig} is the enthalpy of oxygen vacancy migration and k_B Boltzmann's constant. For the sake completeness it has to be mentioned that the overall measured ionic activation energy E_a of the strained volumes consists of the enthalpy of oxygen vacancy migration ΔH_{mig} and the enthalpy of oxygen vacancy-dopant associate formation ΔH_{assoc} through

$$\Delta E_a = \Delta H_{mig} + \Delta H_{assoc}$$

Equation 9.5.4

We consider predominantly the migration enthalpy to change, and refer for discussion of defect associations to Refs.[183-188]. Throughout the following we consider the migration enthalpy to be the dominant term; therefore, the activation energy is treated to be represented in good

approximation by the migration enthalpy. The total volume change is negligibly small for solids; therefore, energy and enthalpy are considered to be equal.

One can express Eq. 4 in terms of the oxygen ionic diffusion coefficient, D_{ionic}, being proportional to the square of the jump distance d and its oxygen ionic hopping frequency ω by:

$$\sigma_{ionic}(T) = \frac{(2q)^2 \left[V_o^{\bullet\bullet} \right]}{k_B T} D_{ionic} = \frac{(2q)^2 \left[V_o^{\bullet\bullet} \right]^2}{k_B T} d^2 \omega \quad \text{Equation 9.5.5}$$

$$= \frac{(2q)^2 \left[V_o^{\bullet\bullet} \right]^2}{k_B T} a_\varepsilon{}^2 \omega \alpha_\varepsilon \qquad \qquad \text{Equation 9.5.6}$$

The jump distance d is directly related to the lattice constant a_ε of the $Gd_{0.1}Ce_{0.9}O_{2-\delta}$ and strain state due to its cubic fcc lattice structure nature, Eq.6. For oxygen ionic hopping over vacancies in the strained fcc lattice the geometry factor $\alpha_\varepsilon = 1$. It is important to note that modifications of the strain tensor elements may lower symmetry and, hence, affect in Eq.6 both the geometry factor and strained lattice constant a_ε for the conducting $Gd_{0.1}Ce_{0.9}O_{2-\delta}$. This could also potentially alter Poisson's ratio.

We can assume the only quantity that is significantly influenced by strain is the migration enthalpy ΔH_{mig}, all other quantities are hardly affected by strain.[2, 83, 84] Thermodynamically the $Gd_{0.1}Ce_{0.9}O_{2-\delta}$ strain activated volume, ΔV_{mig}, of ionic migration (and possible contributions of association, included in the migration enthalpy) depends on the applied hydrostatic pressure p imposed by the erbia single layers in the multilayer dot; this is in accordance to De Souza`s models[55,56] and is described in good approximation by the following equation:

$$\Delta V_{mig,eff} = \frac{\partial \Delta G_{mig}}{\partial p_{eff}} \qquad \qquad \text{Equation 9.5.7}$$

where ΔG_{mig} stands for the Gibb's energy of migration. The Gibb's free energy is given by

$$\Delta G_{mig} = \Delta E_{mig} - T\Delta S_{mig} - \sigma\Delta V_{mig}$$ *Equation 9.5.8*

for a system influenced by the strain tensor σ. Neglecting the activation entropy and considering the case of biaxial strain, we can rewrite (eq. 8) using (eq. 5) to

$$\Delta H_{mig} = \Delta E_{mig} - \frac{2}{3}\sigma_{xx}\Delta V_{mig}$$

Equation 9.5.9

The biaxial strain σ_{xx} is then given by

$$\sigma_{xx} = 3B\frac{1-2v}{1-v}\frac{a-a_\varepsilon}{a_\varepsilon}$$ *Equation 9.5.10*

B denotes the bulk modulus, v Poisson's ratio and a and a_ε the lattice constants of the unstrained and strained material, respectively. Using the lattice mismatch and above presented equations the activation volumes of the strained multilayer thin film samples could be calculated, see Table 9.2. The resulting strain activated volumes range from 3.03 to 7.22 cm^3 mol^{-1} correspond to a change in ionic activation energy of 0.75 to 1.06 eV for an increase of 6 to 60 single layers in the multilayers ($Gd_{0.1}Ce_{0.9}O_{2-\delta}$/$Er_2O_3$)x3 to ($Gd_{0.1}Ce_{0.9}O_{2-\delta}$/$Er_2O_3$)x30. Using the consideration of elastic moduli in bulk and thin film samples presented above this corresponds to a change of strain of 0.1% or 1.16%, estimated from Raman spectroscopy. For the constants used in the calculations, see Refs.[177-179]. The change in activation volume is increased for highly strained structures. De Souza states that the activation volume of fluorite-structured oxides is 1 to 2 cm^{3}mol^{-1} for pressures below 1 GPa[55].

Table 9.2: Calculated strain activation volumes for the multilayer thin film system investigated.

Specimen	Strain activation volume / $cm^3 mol^{-1}$
$(Gd_{0.1}Ce_{0.9}O_{2-\delta}/Er_2O_3)x3$	3.03
$(Gd_{0.1}Ce_{0.9}O_{2-\delta}/Er_2O_3)x10$	3.96
$(Gd_{0.1}Ce_{0.9}O_{2-\delta}/Er_2O_3)x30$	7.22

9.6 The Role of Micro-Electrode Contacting and Geometry in Measuring Strain-Ionic Transport Modulations for Micro-Electrochemical Devices

State-of-the-art electric contacting operates either *via* placing of top in-plane electrode contacts on a strained multilayer film or by macroscopically painting metal electrodes at the sides of the multilayer[79,189]. As discussed in the introduction both strategies may not be applicable for implementation of strained multilayer oxides as functional building blocks for new micro-electrochemical chip devices. Nevertheless, we exemplify the state-of-the-art contacting of similarly strained $Gd_{0.1}Ce_{0.9}O_{2-\delta}/Er_2O_3$ multilayers *via* deposition of top in-plane electrodes, see Figure 9.5a and b. Although the thickness of the individual single layers was changed over a wide range to affect the strain activated volumes of the small band gap $Gd_{0.1}Ce_{0.9}O_{2-\delta}$ phase no change of activation energy was measurable. Similar observations were made for the effective ionic conductivity measured as invariant on strain activated volume of the ceria single layers for the contacted top-electrodes. Using state-of-the-art top-electrode contacting it can be assumed that only the topmost layer is contributing to the total conductivity *via* pathway P1 of the equivalent circuit model in Figure 9.5c. Here, the pathways P2-P4 of the circuit model (*i.e.* the strained volume fractions) do not contribute to the overall conductivity measured through the top-electrode approach.

The electric field lines get restricted and blocked off at the subsequent insulating erbia single layer. Hence, no strain effect is measurable even though it is present in the sample for state-of-the-art top-electrode contacting of the multilayer. This clearly demonstrates the need for sideways contacting and alternative strategies such as for micro-dot based devices with sideways contacting.

Literature reports on multilayers for which despite the structural proof no effect of strain on ionic transport of the structures was measurable, *i.e.* for top in-plane electrode contacted YSZ/CeO$_2$ multilayers or strained gadolinia-doped ceria films[71,143,144]. For that case alteration of the micro-electrode design relative to the strain tensor elements and activated volumes of the conductive multilayer component is of importance.
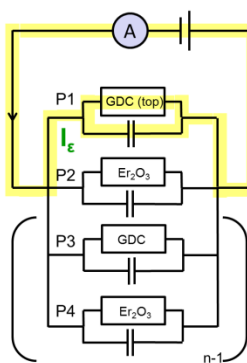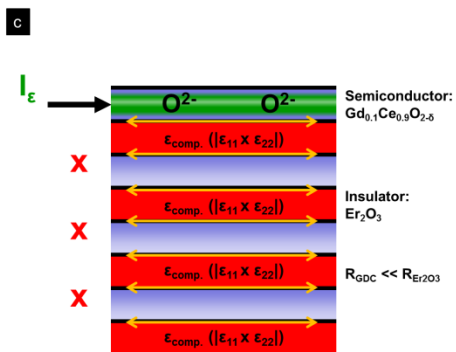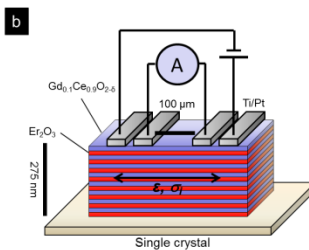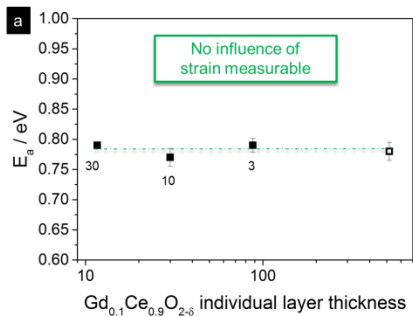
Figure 9.5: Ionic conductivity for top-electrode contacted and strain modulated $Gd_{0.1}Ce_{0.9}O_{2-\delta}/Er_2O_3$ multilayer films. a) Arrhenius plot of the conductivity for $Gd_{0.1}Ce_{0.9}O_{2-\delta}$ single thin film vs. $Gd_{0.1}Ce_{0.9}O_{2-\delta}/Er_2O_3$ multilayer thin films for classic top in-plane electrode contacting. The numbers next to the specimens indicate the number of bilayers. b) The measurement setup is shown for top in-plane electrode contacting. The activation energy remains invariant on the strain state of the multilayer. The classic measurement set-up is not suited to measure real strain effects on ionic transport. c) Schematic view graphic on conduction pathways and electronic circuit model for the classically contacted $Gd_{0.1}Ce_{0.9}O_{2-\delta}/Er_2O_3$ multilayer. Left: Model of the current flow in the specimen for $R_{GDC} << R_{Er2O3}$. Here, the ionic current flows only through the top most $Gd_{0.1}Ce_{0.9}O_{2-\delta}$ layer; it gets blocked at the subsequent insulating erbia layer and other strained $Gd_{0.1}Ce_{0.9}O_{2-\delta}$ films do not contribute to the current in the device. Right: Equivalent circuit model and ionic pathways of the classically contacted multilayer film. The yellow shading indicates the flow of the ionic current going only along P1 (top most layer). All other pathways P2-P4 do not contribute to the electronic circuit.

9.7   Conclusion

We demonstrate a new strategy to fabricate ionic conducting gadolinia-doped ceria/erbia multilayer dot array structures, illustrate the feasibility of sideways dot contacting for 2 orders of magnitude smaller distances (15 microns) towards the state-of-the-art and show that the ionic conductivity activation energy of the small conducting ceria-based phase can be manipulated by the compressively imposed strain activated volumes through the erbia for a multilayer dot.

All multilayer thin film dots show the orientation aimed for, *i.e.* successful biaxial texturing of the metal oxide thin films on the sapphire substrates can be concluded. To get insight into the interfacial state, Raman spectroscopy was applied to investigate the cation-anion-near order. Changes in the strain state can be correlated to a relative change of the positions of the Raman shifts and the sensitivity of this method allows observing increasing strain at the interface as the proportion of strained volume is increased. Regarding the activation energy, a change of $\Delta 0.31$ eV can be observed for ~1.16% relative strain for the ceria-based phase in the multilayer samples.

Our findings have the following implications for the future design of micro-electrochemical devices based on strain oxide modulation.

First, a strategy to fabricate such electrochemical heterostructures as microdevices is presented. This strategy allows exploiting the altered flux of charge carriers along the interfaces parallel to the surface for a sideways controlled ionic conducting multilayer dot. For example, our work opens the possibility to replace classic single metal oxide films in future resistive switches by a functional strained multilayer dot. The broad range for which we can alter the ionic conductivity activation energy through compressive strain, in the given example of ceria single layers for the multilayer dot, would not be achievable by classic doping or changes of non-stoichiometry for a resistive switch functional oxide film. Hence, we can use the interfacial strain of such multilayer dots and short electrode distances to actively tune the desired resistive properties in their memristive and memcapacitive properties in follow-up studies. The short electrode distances were a prerequisite to reach typical local electric field

strengths of about $> 10^6$ V/m[39]. The presented fabrication strategy together with the concept of micro-dots with strained internal interfaces is a promising avenue for novel electrochemical micro devices, *e.g.* energy conversion and storage devices, information technology devices or sensors.

Second, we contribute with a hands-on proof-of-concept to the on-going debate on the role of micro-electrode contacting for strained ionic conducting multilayers. Revealing that the classical top in-plane electrode approach is not suitable to measure real strain effects for the given case of erbia/gadolinia-doped ceria multilayers; the change in activation energy is nil for a broad range of number of interfaces varied (ranging from a single layer thickness from 300 to 6) even though there is structural proof for strain. Measuring the same multilayer structures with the sideways contacted micro-dot approach reveals that a *real strain effect* is indeed measured. Defect thermodynamics and strain activated volume model were well applied to describe the change of conductivity and activation energy for the multilayers.

Third, till date it was challenging to compare strain-ionic transport results obtained by different research groups for multilayer systems based on zirconia or ceria single layers as a conductive phase. Looking forward, the quantitative analysis of near order and ionic bond strength of the anionic-cationic lattice that can be measured by Raman spectroscopy punctuates its potential with respect to a multilayer's film growth, processing and chemistry. State-of-the-art literature considers cationic disorder to be characterized by XRD and so very often no clear trends were observable relative to the varying strain activated volumes. However, we report that there are observable near order relaxation processes relative to the strain activated volume occurring on the near order and confirm earlier computational study predictions.

10   Impact and Follow-up

Strain engineering for solid state ionics has received considerable attention over the last 10 years, not only for basic research but also for application like micro solid oxide fuel cells. For instance, it is being considered to use layered systems as an engineering strategy for modulating the conductivity for low-temperature solid oxide fuel cells[190], but some groups also seek strategies to limit interfacial effects, since for some applications their effects are detrimental[191]. Sanna *et al.*[192] employed layered structures to phase-stabilize a chemical phase, namely δ-Bi_2O_3, to consequently control the conductivity of the system. Most of the work was carried out using pulsed laser deposition, but other thin film deposition techniques have been investigated as well, *e.g.* sputtering[193].

Different strain magnitudes were investigated using a layered system with Yttrium doped zirconia and $Ce_{1-x}Zr_xO_2$ where different zirconia contents were used to modify the lattice constant of $Ce_{1-x}Zr_xO_2$ through Vegard's law[53]. Strain effects on conductivity was also not only studied in fluorites structure oxides, but also in perovskites[194] or Ruddlesden-Popper phase materials[106].

The results of part II of this thesis tackling strain-modulated conductivity changes were confirmed independently by Fluri *et al.*[72]. Lazovski *et al.*[195] demonstrated as well that lattice compression and the resulting strain in acceptor doped ceria give rise to increased activation energy of ionic conduction.

A discussion regarding the role of contacting was amplified, *e.g.* the role of the sideways electrode placement as suggested for the new microdot contacting route was discussed by Shen and Hertz[53] and Pergolesi *et al.*[196]. Also the work by Wen *et al.*[58] extensively discusses the role of electrode placement for measuring heterostructures.

Investigation of fluorite structures with Raman spectroscopy gained popularity after we demonstrated its usefulness to track strain states in fluorite oxide structures as the cationic and oxygen anionic near order vibration can suitably be measured, *e.g.* by Ackermann *et al.*[197]. Raman

microscopy was also applied by Shi et al.[198] to reveal local strain changes in buckled thin film membranes. In this application the very high spatial resolution compared to other methods, *e.g.* optical profilometry, is of great advantage.

The current review by Pryds and Esposito[59] shows that this topic is still getting a lot of attention and will probably remain of great interest for the scientific community over the next years.

PART III
Designing Strained Interface Heterostructures for Memristive Devices

11   Abstract

Ionic heterostructures are an exciting new way of designing novel types of functional oxides for micro-electrochemical devices through interfacial strain engineering. The application of such heterostructure materials requires novel fabrication routes for devices and proof-of-concept on its capability to actively modulate properties such as conductance or memristance with respect to interfaces and strain fields. Herein, we report a first strain-modulated memristive device based on heterostructure microdots where interfacial strain is used in the model system $Gd_{0.1}Ce_{0.9}O_{2-\delta}/Er_2O_3$ to set and tune the property of "memristance". By decreasing the electrode separation of a microdot beyond standard, high local electric field strength can be established in the strained oxide units through which a classic resistance can successfully be altered to a memristance for the current-voltage profiles of the device. Excitingly, we uncover strong local biaxial and anisotropic distortions in the switching layers of the microdots at high strain fields in the oxides through an unusual approach of near-order vibrational Raman spectroscopy mapping and combined long range-order TEM studies. Relaxed and rather isotropic lattices are predominantly present for the ionic conducting layers of the heterostructure microdots when we fabricate low-strained interfaces for enlarged monolayer thicknesses. Using density functional theory calculations we develop a model explaining the effect of strain on lattices, oxygen-transport and memristance through interfacial reduction of the ceria phase upon high strain levels in the heterostructure dots. Finally, we can directly link the effective strain level and distortion degree acting on the conducting ceria phase of the heterostructure microdot to the defect concentrations and, consequently, the memristance modulating the hysteretic behavior to nonvolatility as a property. Strain-engineering of functional oxides such as in heterostructure microdot units is a new way for tuning the properties for oxide-based electrochemical devices beyond the classic ways for future information technology, and energy storage and harvesting devices based on memristive functions.

12   Introduction

Material heterostructures have provided discoveries and excitement to engineer novel electro-chemo-mechanic properties for fast ion conductors under strain[22,46,50,57,58,64,72,192]. Ion conductors and modulating their transport properties are of paramount importance for applications like energy and information technology or sensors, requiring high functional density and properties tailored for the application[61,142,199]. This challenges scientists to develop new tools and routes to provide the means to precisely control the material architectures.

The constituents of ion conductor heterostructures can be defined as two oxide materials that are consecutively stacked at varying layer count and layer thickness and grown with a given orientation on a single-crystalline substrate. The resulting lattice mismatch at the interfaces leads to compressive and tensile strain in the two constituent materials, respectively. Choosing one of the materials to be a conductive phase allows the active modulation of the oxygen ionic transport dependent on the magnitude of interfacial strain through the number of interfaces at a constant total film thickness[55,76,198]. Up to now, most of the studies in this area have been directed towards a fundamental understanding without device integration and performance design. However, strained heterostructure oxides may offer a direct integration as functional thin film compounds with tunable carrier transport for novel circuit elements with extended functionalities in the future.

In the last few years the field of *ionic* memristive memories (also often referred to as memristors or resistive switches) rapidly emerged and received considerable attention due to their potential to replace *electronic* transistor based technology in future memory and computing architectures[17,28,200-204]. This is because *ionic* memristive devices offer lower power consumption, shorter read/write times, superior endurance, *etc.* compared to conventional technologies[200]. Redox-based memristive memories rely on the control of ionic carriers in oxide thin films under a strong bias stimulus[21,205,206]. Despite the huge progress made in the field of memristive memories, material design criteria and tools still need to be

developed to open new ways for material architectures. Here, alternative ways in designing these oxide film structures to alter their carrier flux/concentration profiles under bias for ionic memristive devices to modulate the property of "memristance" are needed. Nowadays, most devices are based on a single oxide film, either crystalline[207] or amorphous[208], as the switching element, relying only on doping to control material properties.

For modulating the charge transport, strain engineering is a promising material design tool. It has been shown that strain modulation can alter the resistivity by several orders of magnitude, and can induce large changes in the activation energy when compared to classic doping approaches[46,57]. Although the impact of strain modulation in ionic heterostructure oxides is clearly demonstrated, no study has been carried out as to how ionic transport-strain modulation affects on the one hand the property of "memristance" and also the performance in a real device. Here, the question of how to design material heterostructures and integrate them into strained ionic memristive devices is explored for the first time for the property of memristance.

To rationally connect the control of strain at heterostructure interfaces to charge transport and memristance, it is necessary to gradually increase the overall strain through an increased number of interfaces while keeping the total film thickness constant. Any such model system must consist of a switching oxide heterostructure sandwiched laterally between two metal electrodes at reasonably small distances in order to achieve the required electric field strength, which is one of the fundamental requirements of the memristive device. This forms the basis to systematically design strained model ionic heterostructures to modulate the physical property of memristance. Ref.[209] reported through a microdot contacting route the successful contacting and strain engineering of heterostructures to measure its impact on "resistance" for the system $Gd_{0.1}Ce_{0.9}O_{2-\delta}/Er_2O_3$. On the other hand, memristive devices are operated at room temperature with high electric fields, conditions under which strain effects are expected to affect ionic conduction most strongly[22,51,79]. However, devices based on strained ionic conducting oxide heterostructures to alter

"memristance" still do not exist, require novel fabrication routes at smaller dimensions compared to state-of-the-art microdots, and principles are still to be proven.

We use lattice strain modulation as a new design tool in oxide heterostructures to gain fundamental insights on the control of oxygen ionic transfer, and to expand our knowledge significantly beyond the previously studied implication on the property of resistance[209], newly through this work, to the physical property of "memristance". This could enable a novel ionic type of electrochemical device, namely, the *strained ionic memristor based on oxide heterostructures*. In the present study, we carry out a systematic investigation of structural and transport properties of compressively strained microdot heterostructure oxides to design a well-described model system and relate to the newly suggested operation as strained memristive memory through alteration of memristance.

13 Methods

13.1 Pulsed laser deposition targets

The powders, $Gd_{0.1}Ce_{0.9}O_{2-\delta}$ (Praxair, Woodinville, WA) and Er_2O_3 (Sigma-Aldrich, Switzerland) were uniaxially and then isostatically pressed at 440 bars for 2 minutes to form ceramic targets. Sintering was carried out isothermally at 1650 °C for Er_2O_3 and at 1400 °C for $Gd_{0.1}Ce0.9O_{2-\delta}$ with hold times of 24 h for Er_2O_3 and of 4 h for $Gd_{0.1}Ce_{0.9}O_{2-\delta}$. Heating and cooling rates were 5 °C/min each.

13.2 Pulsed laser deposition thin film fabrication

Mono- and heterolayer film depositions were carried out on round single crystalline, double-side polished (0001)-oriented sapphire substrates (Stettler sapphire, Switzerland). Before deposition, the PLD chamber (Surface Technologies, Germany; KrF excimer laser, 248 nm) was pumped to a pressure of 4×10^{-6} mbar. The deposition was performed at 700 °C, at an oxygen pressure of 0.0267 mbar and with a target-substrate distance of 85 mm. The laser energy during deposition was kept constant at 0.81 J/cm^2. To get different layer thicknesses the number of pulses was adjusted accordingly, for growth rates see Supplementary information S1.

13.3 Microdot Heterostructure and Sidewise Contact Microfabrication

After thin film deposition carried out by Pulsed Laser Deposition, the samples are subject to photolithography to create a pattern of dots on the films that we can use to make the microdots. Those dots are the template for the microdots. This pattern was made with spin-coating AZ 4533 Photoresist (Microchemical, Germany) to achieve a thickness of 4.3 – 4.6 microns. After letting the sample rest and soft-bake with 100°C for 90 sec the sample was exposed in a MA6 mask aligner (SUSS MicroTec, Germany) with a dose of 190 mJ/cm^2 at 405 nm. After a short resting time the sample was subject to post-bake with 115°C for 20 sec. After another

resting period we developed the sample in 2 different puddles filled with AZ 826 developer with 39 sec in each puddle. Finally the sample was dried in an N_2 stream. In the next step, the microdots were etched using an Oxford Plasmalab 80. After the dots were free etched the pattern for the electrodes had to be defined. AZ nLof 2020 (Microchemical, Germany) was spin-coated onto the sample. After a resting period the samples were soft-baked at 110 °C for 180 sec followed by another resting period. The samples were exposed with a dose of 75 mJ/cm^2 at 365 nm. After another resting period they were post-baked at 110°C for 90 sec. After a final resting step for rehydration the samples were developed in 2 puddles of AZ 726 for 45 sec each. Then the samples were dried in an N_2 stream. We detail the fabrication process flow in Supplementary information S1.

13.4 Structural characterization

The ceramic PLD targets and as-deposited thin films were characterized by X-ray Diffraction (Bruker D8, Cu Kα). Confocal Raman microscopy and Raman mapping (WITec CRM200, WITec, Germany and WITec 300 alpha, WITec, Germany) was done using a 532 nm wavelength laser for excitation with a spectral resolution of 0.7 cm^{-1}. Fitting was done by OriginPro 9.1 using a Gaussian function.

13.5 Microstructural characterization

Scanning electron microscopy (SEM, LEO 1530) was used to analyze the surface topography and cross-sections. Preparation of the TEM lamellas was performed using FIB scanning electron microscope (Zeiss NVision 40). The gallium beam-induced deposition of the protection layer and then subsequent milling were carried out at 30 kV and 300 pA. HR-TEM images were acquired using an FEI Tecnai F30 FEG operating at 300 kV. The annular dark field STEM images were recorded using a FEI Talos F200X operated at 200 kV. Fourier diffractogram analysis was performed using the Gatan DigitalMicrograph software package.

13.6 Electrical measurements and microdot device characterization

Device contacting was done using Pt needles and 3D micropositioners (Everbeing, Taiwan). All electrical measurements were carried out with a Keithley 2612B source measurement unit (Keithley Instruments, USA). Preforming was performed using a positive voltage of 200 V with a ramping-up speed of 1 V/s. After reaching the maximum voltage a compliance current level of 200 nA was set. Previous experiments showed that a current higher than 200 nA can lead to device failure. A preforming was successful if the current reached the set compliance level of 200 nA and stayed there until the hold time of 1 h ended. Cyclic voltammetry was carried out with maximum amplitudes of +/- 200 V with a sweep rate of 500 mV/sec. Each sample was cycled at least 50 times to ensure stability.

13.7 Density functional theory (DFT) calculations

Our density functional theory calculations were performed with the VASP code[210] using the PBEsol exchange-correlation functional[211]. Wavefunctions were expanded in planewaves up to a kinetic energy of 500 eV for PAW potentials[212,213] with explicit Ce 4f states, while Er 4f states were frozen in the core in a Er^{3+} configuration. For the 4-atom fluorite unit cell a 12x12x12 Γ-centered reciprocal space mesh was used, which was reduced to 3x3x3 for the 96-atom cubic supercell and to 2x2x1 for the cell used to describe the CeO_2/Er_2O_3 interface. In our calculations Gd doping was implicitly included by removing a O atom along with two electrons from the simulation cell when creating an oxygen vacancy, which electronically mimics the presence of a $2Gd_{Ce}^{'}V_O^{\bullet\bullet}$ cluster. Phonon calculations were carried out within the frozen phonon method implemented in the Phonopy code[214].

14 Results and Discussions

14.1 Ionic Heterostructure Oxide Dot Design for Strained Anionic Memristive Devices

We fabricate biaxially strained heterostructure oxide microdots to study the influence of strain on oxygen anionic switching and the memristive behavior, Figure 14.1a. The microdots are fabricated using pulsed laser deposition, ablating thin films onto single crystalline sapphire substrates. Our thin film model system consists of two different materials, $Gd_{0.1}Ce_{0.9}O_{2-\delta}$ and Er_2O_3. One material, in our case $Gd_{0.1}Ce_{0.9}O_{2-\delta}$, is more conductive than the second one by several orders of magnitude[120,139]. The second material serves in this case only to impose compressive lattice strain on the conductive $Gd_{0.1}Ce_{0.9}O_{2-\delta}$ phase and to therefore modulate the electrical transport in the heterostructure, Figure 14.1b. This strain-imposing phase, here Er_2O_3, is chosen to be an electrical insulator[181]. The two phases, conductive and insulating, are stacked consecutively; the total film thickness was kept constant at a thickness of 275 nm ± 10%, while the number of interfaces was actively varied, *i.e.* from 6 to 60 interfaces. As a result, the heterostructure oxide microdots with a low number of interfaces are supposed to have less strain acting on the ionic conductor lattice and interfacial strain increases with an increasing number of interfaces for the microdot, since the strain is the biggest at the interfaces. Now to rationally access the strained interfaces down to nanoscale, it is necessary to develop a unique device design with sideways attached electrodes contacting the free-etched heterostructure dots on a chip. The switching mechanism for ceria based memristive devices is based on oxygen vacancy conduction in the ion conductor balanced by electronic carriers[139,215,216], which we will now actively tune by imposing the strain field in various degrees with the insulating erbia layer and monolayer thickness variations in the heterostructure dot device. Herein, to operate the device units on the chip newly as memristors it is a prerequisite to apply high electric field strengths, in the range of MV/m, for operation as memristive memory. In order to achieve this, a substantial reduction in the device size relative to previously reported microdot devices[209] was

necessary. Hence, the challenge to realize these high field strengths and to contact the strained interfaces directly through sideways attached electrodes at small distances had to be overcome. We present successfully contacted microdot switching structures to alter in this work "memristance" with a small size of approximately 2.5 microns diameter, Figure 14.1c and d. Importantly, this is now roughly a one order of magnitude decreased microdot size when compared to the state-of-the-art in literature which was previously used to alter "resistance"[209] and is an important step to realize those new memristive switches under strain. These microdots were fabricated using photolithography and physical dry-etching, to obtain devices at micrometer-scale, see Methods and Supplementary information 24.1 for details on the microfabrication process flows and materials etch rates.
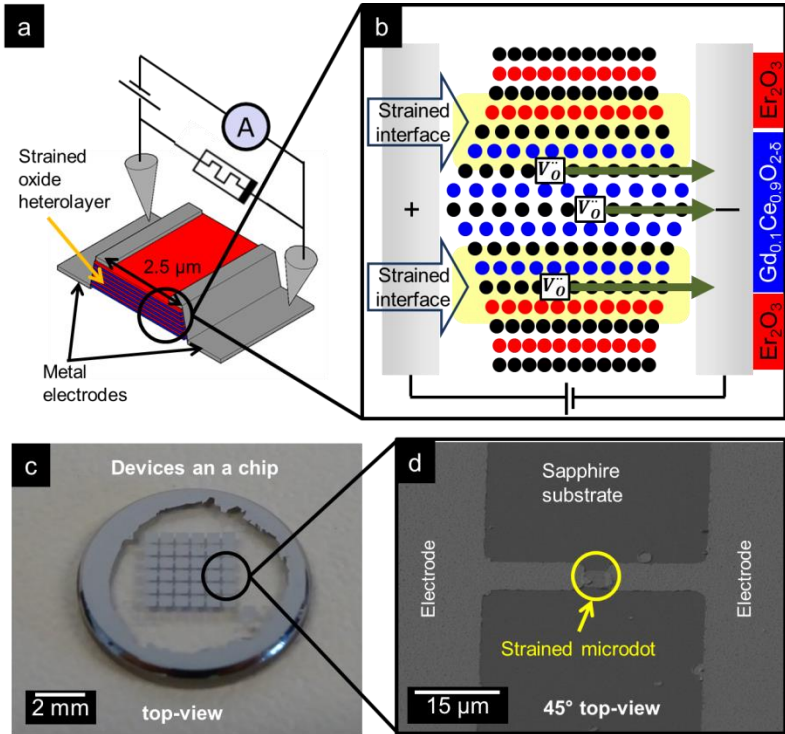
Figure 14.1: Strained multilayer microdots.   a) Schematic view of the microdot system. b), Schematic view of the interfacial lattice mismatch and the conduction model. c) Optical image of the electrode arrangement on the chip with the ceramic microdots in between the contacting bridges. d) SEM micrograph of the strained microdot on the chip.

14.2 Local Modulation and TEM Characteristics of the Anisotropic Strain Field at the Heterostructure Interfaces of the Memristive Oxide Dot

TEM imaging and diffraction techniques have been successfully employed to investigate oxide heterolayers, such as Fourier analysis of high resolution images to investigate crystallographic orientation relationships at heterolayer interfaces. Here we apply both TEM and STEM imaging and diffraction analyses to assess heterostructure layer growth, and the strain state of the conducting oxide phase. In cross-sectional annular dark field STEM images we observe well-defined layers of $Gd_{0.1}Ce_{0.9}O_{2-\delta}$ and Er_2O_3 stacked consecutively with monolayer thicknesses down to 3 nm, Figure 14.2a and b. Oriented growth of the multilayer heterostructure using sapphire-substrates allows for well-defined interfaces between the two materials, which we demonstrate on two examples using atomic-resolution TEM imaging for the 6 and 60 interface modulated heterostructure oxides in a microdot. While keeping the total device thickness constant, we increase the number of interfaces. This results in an increase of the strain-affected volume over the total device. The growth conditions employed here result in oriented growth of columnar grains in the out-of-plane [111] direction. The influence of different growth rates for $Gd_{0.1}Ce_{0.9}O_{2-\delta}$ and Er_2O_3 can also be observed in the cross-sections, see also Supplementary information 24.1 for deposition rates, Table 24.1. Diffraction analysis reveals that the cubic fluorite structure[217] is present throughout the heterostructure microdots for the $Gd_{0.1}Ce_{0.9}O_{2-\delta}$ phases Figure 14.2c. Following a similar TEM diffraction approach to strain mapping in confined Si thin films[218], Fourier analysis of atomic-resolution TEM images[219] was used to make a relative assessment of lattice distortion in the conducting ceria phase for the 6 and 60 interface modulated samples.

Miller plane spacing, d_{hkl}, in the out-of-plane [111] direction and in-plane [311] direction was measured in the $Gd_{0.1}Ce_{0.9}O_{2-\delta}$ phases of the heterostructure microdots using diffractograms (*e.g.* Figure 14.2c and Supplementary Information 24.2) computed from the highlighted regions labeled "1" and "2" in the high resolution TEM images Figure 14.2d and f

for 6 and 60 interfaces, respectively. The highlighted regions were approximately 11 nm tall (*i.e.* in the direction normal to the $Er_2O_3/Gd_{0.1}Ce_{0.9}O_{2-\delta}$ interface), with region "2" in the 6 interface heterostructure microdot positioned 12 nm from a heterolayer interface. For the 6 interface heterostructure dot we assumed region "2" to be more relaxed, as it is furthest from an interface. Importantly, compared to region "2" in the 6 interface sample, we measure that the 60 interface sample exhibits elongation in the out-of-plane [111] spacing by 4.5 ± 0.2 %, which is accompanied by a contraction in the in-plane [311] spacing by 2.1 ± 0.2 % and is consistent with interfacial compressive strain in region "1". In contrast, when compared to region "2" in the 6 interface sample (12 nm from the interface), the out-of-plane [111] spacing in region "1" (adjacent to the interface) is only elongated by 1.2 ± 0.2 %. In conclusion, we report fully strained $Gd_{0.1}Ce_{0.9}O_{2-\delta}$ layers for the 60 interfaces microdot with in plane-compression, and in contrast, relaxation towards the center of the $Gd_{0.1}Ce_{0.9}O_{2-\delta}$ layers for the 6 interfaces microdot. This analysis is detailed in Table 14.1. The oriented growth was further confirmed by XRD, see Supplementary information 23.3. To understand if Gd segregation at the interfaces could play a role in modulating the memristance, we investigated the $Gd_{0.1}Ce_{0.9}O_{2-\delta}$ cation distribution in the $Gd_{0.1}Ce_{0.9}O_{2-\delta}/Er_2O_3$ interface region of an as-prepared heterolayer sample *via* electron energy-loss spectroscopy (EELS) in a scanning transmission electron microscope (STEM), Supplementary Information 24.4. $Gd_{0.1}Ce_{0.9}O_{2-\delta}$ spectra acquired near the $Gd_{0.1}Ce_{0.9}O_{2-\delta}/Er_2O_3$ interface (within 2.5 nm) and relatively far from the interface (22 nm - 28 nm) were compared to determine if there was a significant difference in the ratio of intensities of the cerium (Ce M_{45}) to gadolinium (Gd M_{45}) signals, which is proportional to the ratio of elemental concentrations[38]. The difference in measured intensity ratios in the layer and interface regions was found to be negligible within the measurement error in this case, indicating that the two regions exhibit approximately equal area-averaged cation stoichiometry, see Figure 24.3 for details. Therefore, it is reasonable to conclude that cation segregation doesn't play a role in the strain and interface induced modification of the overall memristive response in these heterostructure devices. EELS also indicated that Ce ions in the interface region were reduced relative to Ce

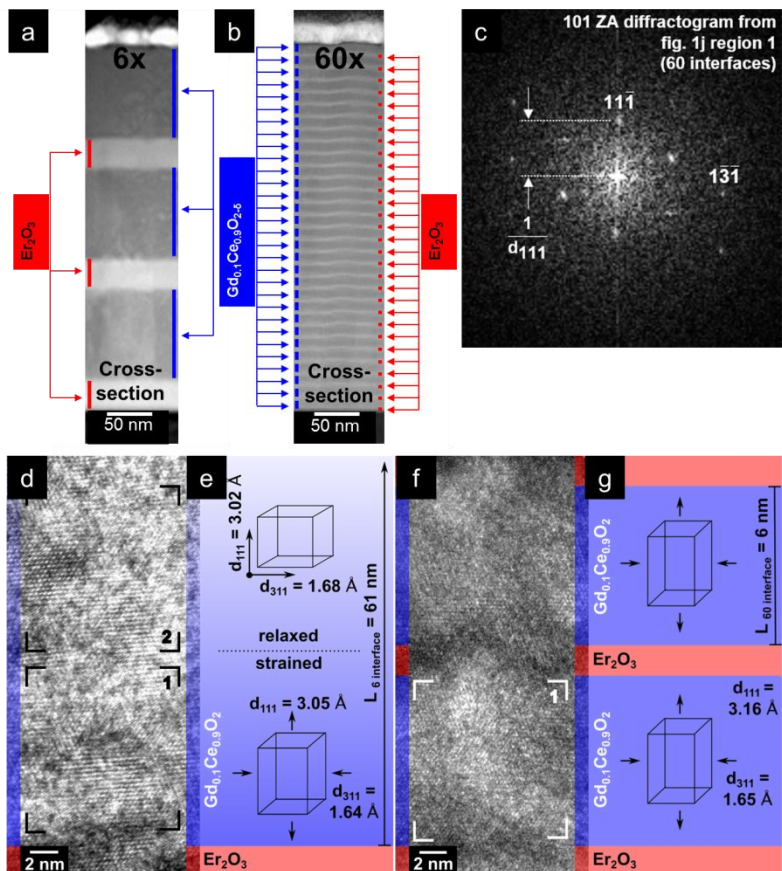ions in the layer region, a consequential point discussed below and in Supplementary Information 24.4.

Figure 14.2: High magnification micrographs of multilayers. a) and b), Annular dark field STEM cross sectional view of a 6 and 60 interfaces $Gd_{0.1}Ce_{0.9}O_{2-\delta}/Er_2O_3$ multilayer sample, respectively. c) Diffractogram of $Gd_{0.1}Ce_{0.9}O_{2-\delta}$ layer displaying fluorite structure (computed from region 1+2 in d). d) and f), atomic-resolution bright field TEM images of $Gd_{0.1}Ce_{0.9}O_{2-\delta}/Er_2O_3$ interface(s) in 6 and 60 interface samples, respectively, with highlighted regions labelled "1" and "2" indicating the areas used to compute diffractograms. e) and g), diagram illustrating the results of the Miller plane spacing measurements in the out-of-plane and in-plane directions in the conducting oxide phase. The 6 interface sample contains a more relaxed region "2" positioned 12 nm from the interface, and a more strained region "1" adjacent to the interface, e), whereas the conducting phase in the 60 interface sample is fully strained, g).

We successfully present a novel design strategy for the heterostructure microdots, which are deployable for testing as switching device to alter memristance. We analyze the strain state near the interface and in the relaxed zones by atomic-resolution TEM, showing the evolution of strain relaxation within the thin film and the in-plane and out-of-plane strain anisotropy. This allows us to locally resolve the strain states at the interfaces and in the center of the layers. In the following we investigate the influence of interface modulations on structure and the property of memristance.

Table 14.1: Comparison of $Gd_{0.1}Ce_{0.9}O_{2-\delta}$ out-of-plane and in-plane Miller spacing obtained through TEM and out-of-plane strain obtained through Raman Spectroscopy.

Microdot constituents	# of interfaces microdot		Region	TEM d_{111} (Å)	TEM d_{311} (Å)	Raman F_{1g} (out-of-plane) strain / %
$Gd_{0.1}Ce_{0.9}O_{2-\delta}$/ Er_2O_3	6 (Figure 14.2d)		2	3.02 ± 0.06	1.68 ± 0.02	0.0085
$Gd_{0.1}Ce_{0.9}O_{2-\delta}$/ Er_2O_3	6 (Figure 14.2d)		1	3.05 ± 0.04	1.64 ± 0.01	0.0085
$Gd_{0.1}Ce_{0.9}O_{2-\delta}$/ Er_2O_3	60 (Figure 14.2f)		1	3.16 ± 0.05	1.65 ± 0.01	0.61

14.3 Raman Spectroscopic Local Mapping and DFT Description for the Heterostructure Resistive Switching Microdots

Motivated by the opportunity to modulate the interfacial strain through the number of interfaces and monolayer thickness for the $Gd_{0.1}Ce_{0.9}O_{2-\delta}$/$Er_2O_3$ heterostructure unit in the device architectures, we turn to Raman microscopy to probe the atomistic near-order correlations and provide a first Raman mapping relative to the device structure features and vibrational modes, Figure 14.3a. We use cluster analysis to decompose the hyperspectral map into single clusters, which can be assigned to the materials and device segments, Figure 14.3b and c.

Raman spectroscopy is a particularly useful type of vibrational spectroscopy to investigate such systems, as exemplified by Kreisel *et al.*[114], for the following reasons: Firstly, we excite the interactions between the cation- and anion sublattices which makes this technique particularly sensitive to changes in the oxygen sublattice[220]. Since the ionic transport in the conductive phase of $Gd_{0.1}Ce_{0.9}O_{2-\delta}$ relies on the oxygen sublattice, this allows us to draw conclusions about structure-transport interactions. Secondly, we can measure with high spatial resolution (~360nm)[1], which is useful for measuring our micron-sized devices using a 532nm laser for excitation. Unlike TEM, Raman spectroscopy directly probes the full extent of the thin film sample in out-of-plane direction. Thirdly, it allows us to directly connect the spectroscopic results to interfacial strain states through interpretation and analysis of the change in the ionic bond strengths through the shift of the frequencies of the Raman bands. When a bond of a heterostructure oxide phase is stretched or compressed it changes its vibrational frequency, thereby altering the peak position of the respective mode. Analyzing the Raman spectra, Figure 14.3d, we first turn to the reference sample made from pure $Gd_{0.1}Ce_{0.9}O_{2-\delta}$ in a single thin film microdot device. A single Raman-active peak is visible, originating from the unstrained fluorite

---

[1] See Supplementary Information 24.5 for calculation of the Raman spot resolution.

structure for only one triply degenerate F_{2g} mode, in agreement with literature[172,221,222]. The efficiency of scattering I is given by

$$I = C \sum_j \left| e_i R_j e_s \right|^2 \qquad\qquad \textit{Equation 14.3.1}$$

where C is a constant, R_j is the Raman tensor of a phonon j, and e_i and e_s are the polarization vectors of the incoming and scattered beams, respectively. For $Gd_{0.1}Ce_{0.9}O_{2-\delta}$ fluorite structure-type the Raman tensors for the three directions of the crystal coordinate system are given by

$$R_x \begin{bmatrix} 0 & 0 & 0 \\ 0 & 0 & d \\ 0 & d & 0 \end{bmatrix} R_y \begin{bmatrix} 0 & 0 & d \\ 0 & 0 & 0 \\ d & 0 & 0 \end{bmatrix} R_z \begin{bmatrix} 0 & d & 0 \\ d & 0 & 0 \\ 0 & 0 & 0 \end{bmatrix}. \qquad \textit{Equation 14.3.2}$$

In the absence of stress the three optical Raman modes have the same frequency of about 464cm^{-1} as the isotropic cubic crystal system is from a group theoretical point of view symmetry inverse, see Loudon *et al.*[222]. In the spectra of the $Gd_{0.1}Ce_{0.9}O_{2-\delta}/Er_2O_3$ heterostructure microdots we can observe a peak splitting of the triply degenerated F_{2g} mode into the in-plane F_{2g} and the out-of-plane F_{1g} modes related to strained $Gd_{0.1}Ce_{0.9}O_{2-\delta}$ cubic fluorite structure, Figure 14.3e and inset of Figure 14.3g. This is associated with a decrease of symmetry for biaxially strained samples where the isotropy between in-plane and out-of-plane direction is lifted[115,223,224]. The strain analysis through Raman microscopy is focused on the $Gd_{0.1}Ce_{0.9}O_{2-\delta}$ modes, since this is the phase that is relevant for the transport behavior, *i.e.* all current flows through this phase. Importantly, this finding agrees with the observation in TEM where we see the elongation along the out-of-plane axis, more pronounced with increasing in-plane compression, as detailed in Figure 14.2d to g and Table 14.1. This lifting of the symmetry could also influence Poisson's ratio[225]. Information on erbia Raman spectra assignment is presented in detail in Supplementary Information 24.6.

We observe a monotonic shift of the relevant Raman band with an increase in the number of interfaces for the $Gd_{0.1}Ce_{0.9}O_{2-\delta}/Er_2O_3$ heterostructure dots, Figure 14.3f. The strain is largest at the interface and relaxes towards the interior of the layers, this means when we start to decrease the monolayer thickness at a constant total film thickness for the

$Gd_{0.1}Ce_{0.9}O_{2-\delta}$ phase, the strain fields can relax less, leading to an overall increase of strain in the system and the splitting of the F_{2g} Raman mode is most pronounced. *Viz.* this agrees with the TEM analysisFigure 14.2d to g. The strain associated with the frequency shift is computed through DFT calculations. Frequencies of the Raman-active stretching modes were computed in the fluorite unit cell with different amounts of imposed in-plane strain, Figure 14.3g. The underestimation of the Raman frequencies in the calculations can be explained by the missing larger Gd ions, which are expected to blue shift the frequencies. The magnitude of relative changes as a function of strain are, however, expected to be reliably predicted. Using the values obtained thereby, we were able to calculate strains in the $Gd_{0.1}Ce_{0.9}O_{2-\delta}$ phase ranging from relaxed (unstrained) to -1.26% compressive strain for 60 interfaces heterostructure microdots. We want to point out that these strain values obtained *via* DFT calculations are in good agreement (within +/- 0.1%) with strain values obtained by high pressure Raman studies on ceria crystals[176]. For further information on how to analyze Raman scattering data from strained samples see Supplementary information 24.5.

Local Raman mapping was successful and used for the first time on a heterostructure microdot device to probe memristance in connection with DFT computations to access the strain states and to show anisotropy present in the conductive $Gd_{0.1}Ce_{0.9}O_{2-\delta}$ phase of the microdot. Density functional theory predictions were used to analyze the data and relate the experimentally obtained values to compressive strains at the internal interfaces. Results of Raman mapping measurements are consistent with those from aforementioned TEM analysis. We use these results to further study the implication on memristance under strain for the microdot devices.
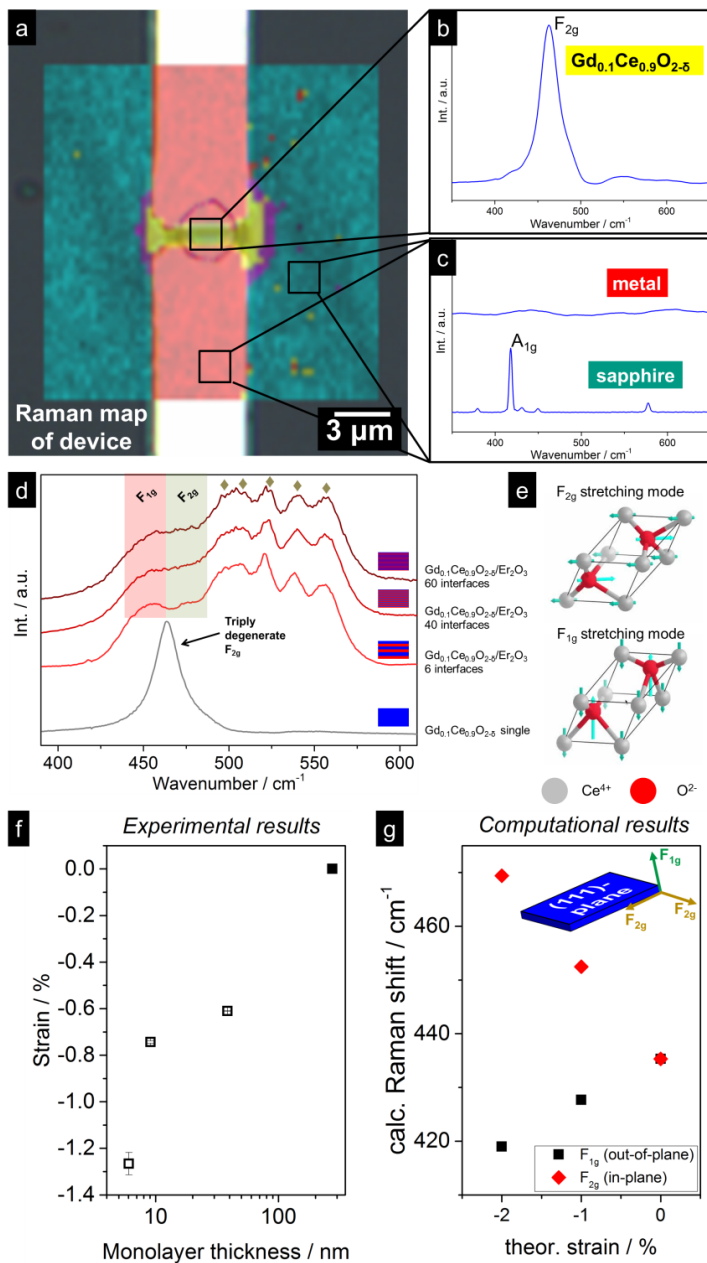
Figure 14.3: Structural characterization, mapping and interfacial strain state. a) Raman device map to investigate the structural consistency of the microdots. The yellow, red, turquoise and purple colors represent different materials obtained through cluster analysis. The purple rim represents an overlay of the yellow $Gd_{0.1}Ce_{0.9}O_{2-\delta}$ signal and the turquoise sapphire signal. b) Cluster analysis of Raman modes extracted from the Raman device map showing the $Gd_{0.1}Ce_{0.9}O_{2-\delta}$ single phase device c) Cluster analysis of Raman modes extracted from the Raman device map showing the electrodes and the substrate, respectively. d) Micro-Raman spectra of the compressively strained microdots. F_{2g} and F_{1g} denote the relevant cationic-anionic $Gd_{0.1}Ce_{0.9}O_{2-\delta}$ Raman bands. The diamonds represent Er_2O_3 bands. The $Gd_{0.1}Ce_{0.9}O_{2-\delta}$ single phase sample shows the triply-degenerate F_{2g} mode. e) Splitting of the $Gd_{0.1}Ce_{0.9}O_{2-\delta}$ bands due to symmetry change in out-of-plane and in-plane modes. f) Analysis of the band shifts using the computational results to compute the magnitude of interfacial strain g) DFT simulations to correlate the Raman frequency shift to strain states. Inset: Raman mode splitting in the sample reference system.

14.4 Physical Switching and Dynamics: A Strained Memristive Microdot Device

As an initial step to characterize the transport behavior of our samples, they were subject to a preforming procedure in accordance with literature[226,227]. After successful preforming the samples were investigated with cyclic voltammetry, Figure 14.4 and Table 14.2. We observe for the single phase $Gd_{0.1}Ce_{0.9}O_{2-\delta}$ sample that with increasing positive voltage there is a continuous increase in current, Figure 14.4a. Once we have reached the maximum and decrease the voltage again, the current decreases as well with a slight hysteresis. For the negative polarity a similar behavior can be observed. After increasing the current with rising voltage at negative polarity we reach the negative maximum, then we decrease the voltage again and observe a continuous decrease of current until zero voltage is reached. Hence, changing the polarity of the device resets it back to the high resistance state within one switching cycle. The unstrained $Gd_{0.1}Ce_{0.9}O_{2-\delta}$ microdot reveals an asymmetric hysteretic memristive switching curve with a low R_{off}/R_{on} ratio of ~1.5 in the positive branch. We ascribe the asymmetry of the current-voltage profile

to the initial preforming step applied with positive polarity discussed in Ref.[227].

Now increasing the compressive strain on the $Gd_{0.1}Ce_{0.9}O_{2-\delta}$ heterolayer phases of the microdot increases the hysteretic opening at positive polarity while maintaining the volatile switching characteristics, Figure 14.4b to d. This leads to an increase of the R_{off}/R_{on} ratio, see also Table 14.2. When the compressive strain on the conductor of the heterolayer dot is increased to -1.26% the switching characteristics of the systems are changing to a non-volatile behavior, Figure 14.4d. For the positive branch a further increase of the R_{off}/R_{on} ratio can be observed, reaching more than 1 order of magnitude. Analysis of the microdots' current-voltage profiles revealed that the OFF-state (high resistance state) remains virtually unchanged with respect to strain at the heterostructure interfaces in the $Gd_{0.1}Ce_{0.9}O_{2-\delta}$ phase, Figure 14.5a. Importantly, it is the conductivity of the ON-state (low resistance state) of the heterostructure dot device that is being modulated by the effective strain imposed on the $Gd_{0.1}Ce_{0.9}O_{2-\delta}$ phase under the high local electric fields. We report that increasing the effective compressive in-plane strain up to -1.26 % in the $Gd_{0.1}Ce_{0.9}O_{2-\delta}$ phase of the heterostructure microdots results in an increase of the R_{off}/R_{on} ratio by one order of magnitude, Figure 14.5b. In the present study we operate for the first time memristive heterostructure microdots to alter memristance at room temperature under high local electric field strength of about 80 MV/m and observe for increased strain the enlargement in the assigned R_{off}/R_{on} ratio of the switch.
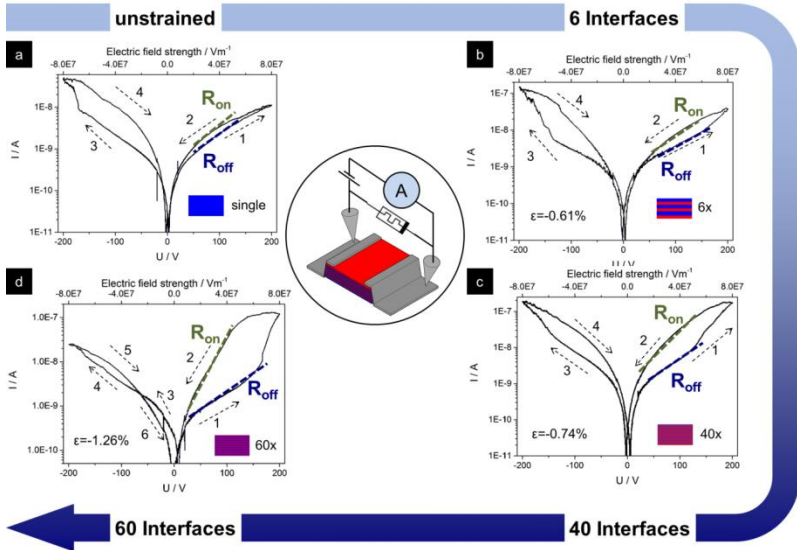
Figure 14.4: Electrical characterization through cyclic voltammetry and memristive behavior. a) I-V curve of the unstrained $Gd_{0.1}Ce_{0.9}O_{2-\delta}$ single phase microdot. b) I-V curve of the 6 interfaces sample c) I-V curve of the 40 interfaces sample. d) I-V curve of the 60 interfaces sample with a strain of -1.26%. This curve shows an additional crossing at negative polarity. The R_{off}/R_{on} ratio increase from 1.5 to 15 when increasing the compressive strain from unstrained to -1.26%.
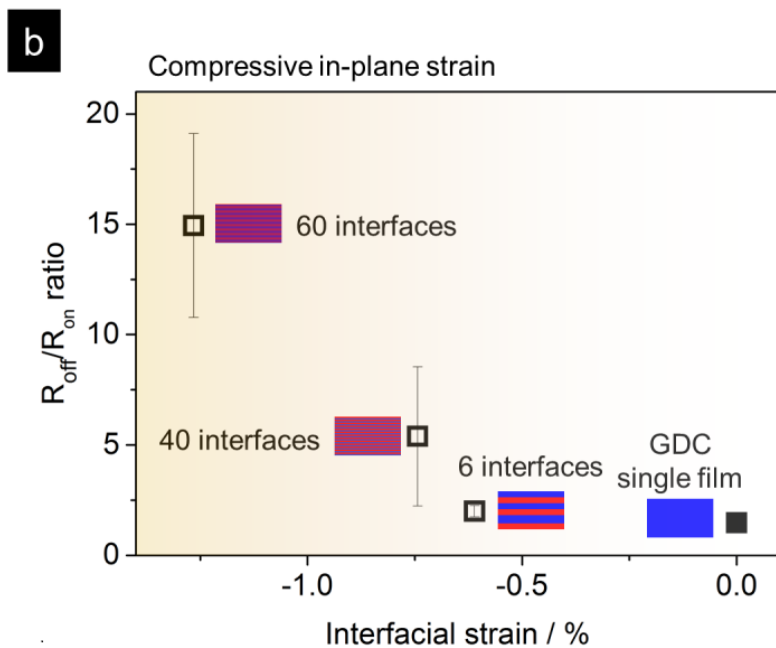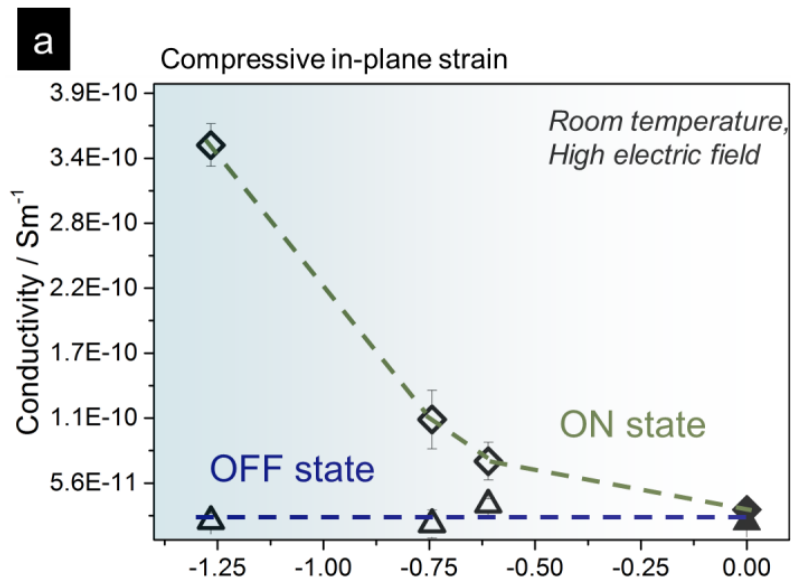
Figure 14.5: Strained interfaces to control memristance. a) The interfacial state of the system acts primarily on the ON-state, the OFF-state remains unchanged. b) This behavior leads to a minimum R_{off}/R_{on} ratio at the unstrained sample an increased R_{off}/R_{on} ratio with an increasing number of interfaces.

We interpret the finding as follows in light of the atomistic structure investigations by Raman spectroscopy and TEM measurements, Figure 14.6a and b. Earlier, Gao *et al.*[228] investigated the switching behavior of single phase ceria films through *in-situ* TEM studies, revealing restive switching by a filamentary type mechanism, mediated by reduced Ce_2O_3 portions within the ceria films. Also, Song *et al.*[129] reported a preferential reduction of ceria at the interfaces within heterostructures formed with zirconia-based oxides as second constituent material. They find that ceria reduction at the interface is independent of the strain, since the Ce^{3+} concentrations are identical for compressive and strain fields applied. However, density functional theory (DFT) studies showed that under compressive strain both neutral (*i.e.* thermally created) and ionized (*i.e.* charge-compensating for Gd^{3+} dopants) oxygen vacancies prefer to be located at the Ce_2O_3/ZrO_2 interface[103]. Such a cerium reduction at the interface is consistent with our own EELS observations, and we confirm the latter results for the CeO_2/Er_2O_3 interface based on our own DFT computation where we plot the energy as a function of the distance to the surface, Figure 14.6c**.** Additional information to the DFT calculations of vacancies at the CeO_2/Er_2O_3 interface is presented in Supplementary information 24.7. Together with our own structural TEM, EELS and Raman spectroscopy investigations, we propose that reduction of ceria takes place close to the (strained) interfaces, increasing the interfacial Ce^{3+} concentration during preforming under high electric field strength in our heterostructure microdot devices for memristance modulation. This is comparable to reduction effects of PLD grown ceria layers relative to the air interface that are described by Chueh *et al.*[229] using XPS. See Supplementary information 24.8 for detailed defect chemical equations on the ceria reduction at the strained interfaces.
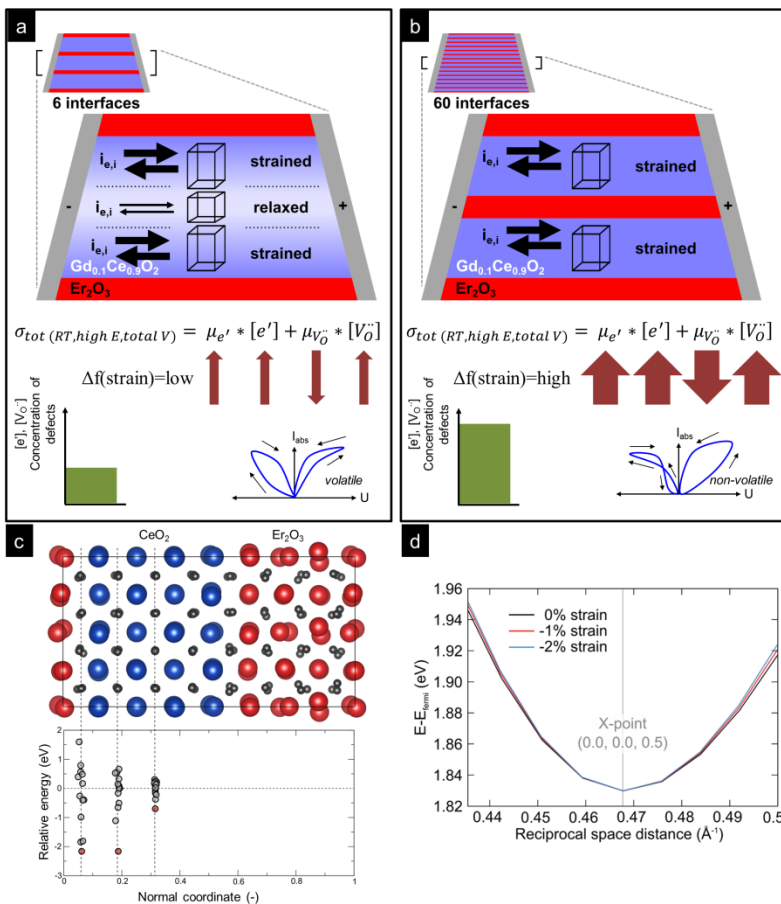
Figure 14.6: Reduced interfacial states in heterostructures. a) The strained interfaces give rise to an increase in the number of charge carriers. The compressively strained volumes decrease the mobility of the oxygen ions. In samples with a low number of interfaces the strain relaxes toward the center of the $Gd_{0.1}Ce_{0.9}O_{2-\delta}$ phase, decreasing the fraction of strained material with respect to the total device volume. The total conductivity is given by $\sigma_{tot\,(RT,\,high\,E,\,total\,V)} = \mu_{e'} * [e'] + \mu_{V_O^{\cdot\cdot}} * [V_O^{\cdot\cdot}]$, where σ_{tot} stands for the total conductivity over the total volume of the $Gd_{0.1}Ce_{0.9}O_{2-\delta}$ phase of the device. $\mu_{e'}$ and $\mu_{VO^{\cdot\cdot}}$ represent the electronic and ionic mobilities, respectively; [e'] and $[V_O^{\cdot\cdot}]$ are the electronic and ionic charge carrier densities. b) In samples with a high number of interfaces the device volume is fully strained. The influence on charge carrier densities and mobilities is much larger. c) DFT calculations show it is energetically favorable for the defects to be located close to the interfaces. d) Increasing the compressive strain reduces the effective mass of the electrons, thereby increasing the electronic mobility, as confirmed through DFT calculations.
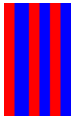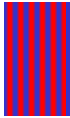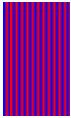
We now turn to the effect of the systematically modulated strained volumes in the ceria-based phases of the heterostructures on the memristive response: By two independent structural investigation methods, TEM and Raman, Figure 14.2 and Figure 14.3, we show that the magnitude of strain and, importantly, of its biaxial lattice distortion is systematically increased with increasing number of interfaces in the microdot, Table 14.1. Secondly, in the heterostructure dots with a low interface count, a relaxed and less biaxially distorted zone is found within the ceria-based monolayer structures for distances greater than 12 nm from the interface. The overall higher degree of biaxial lattice distortions in the ceria-based heterostructure dots with 60 interfaces (high strain) has an effect on both the ionic and electronic charge carriers and the mixed conductivity. A formation energy reduced by up to several tenths of eV[103] results in an increased effective concentration of oxygen vacancies balanced by an also increased number of electronic carriers (in line with our EELS observations, Ref. [129] and [229]). The oxygen vacancy mobility is reduced due to increased migration barriers under compressive strain[55] as also confirmed by our DFT calculations (Supplementary information S7). Here, the curvature of the lowest unoccupied bands in pure CeO_2 is found to increase with increasing compressive strain, meaning that the electrons resulting from oxygen vacancy formation, which reside in these bands, are characterized by a lower effective mass and hence higher mobility with increasing compressive strain, Figure 14.6d. For the highly strained (high interface count) microdot heterostructures, the high biaxial strain thus leads to an increase in the electronic mobility that can be used for modulation of the memristance in the ON-state. The excess electrons created populate the Ce 4f band[230]. The overall conductivity is given by

$$\sigma_{tot\,(RT,\,high\,E,\,total\,V)} = \mu_{e'} * [e'] + \mu_{V_O^{\cdot\cdot}} * [V_O^{\cdot\cdot}] \qquad \textit{Equation 14.4.1}$$

where σ_{tot} stands for the total conductivity over the total volume of the $Gd_{0.1}Ce_{0.9}O_{2-\delta}$ phase of the device. $\mu_{e'}$ and $\mu_{Vo\cdot\cdot}$ represent the electronic and ionic mobilities, respectively; *[e']* and *[V_O¨]* are the electronic and ionic charge carrier densities. The modulation of the electronic charge carrier densities balanced by oxygen ionic vacancies and their mobilities, respectively, gives rises to the *memristance* modulation after preforming. This interplay of electronic and ionic conductivity also explains the

change of persistence in highly strained and high interface count samples. The increase in memristance, *i.e.* the formation of the hysteresis during cycling is a product of the changed conductivities, due to the formation of reduced filaments of ceria[228], facilitated through the interfaces[129] and modulated by the compressive in-plane strain. The introduction of the additional crossing in the current-voltage signal of the high interface sample can be explained through the mechanism of filament breakdown: The filament of reduced material is reoxidized through transport of oxygen ions to the filament. This ionic transport is governed by compressive strain because oxygen ions must diffuse inwards from the electrodes. Only if the ionic transport is very slow the filament is stable enough to keep the low resistance state while cycling back to zero voltage and then start cycling with opposite polarity. Another reason supporting these characteristics is the overall change in relaxed (non-reduced) volumes as confirmed in our HRTEM measurements. Samples with a lower interface count have thicker individual $Gd_{0.1}Ce_{0.9}O_{2-\delta}$ layers; therefore, more material is available which acts as oxygen reservoir. A varying magnitude of strain in the $Gd_{0.1}Ce_{0.9}O_{2-\delta}$ phases and interfacial effects altered by the interface count in the heterostructure microdots of the devices govern structurally the break in cubic symmetry, raising oxygen vacancy sites and in turn, can be actively used to tune the memristance property.

Table 14.2: Analysis of the IV-profiles in resistive switching for strained heterolayer microdots

Microdot constituents		# of interfaces microdot	$Gd_{0.1}Ce_{0.9}O_{2-\delta}$ monolayer thickness / nm	Er_2O_3 monolayer thickness / nm	in-plane strain	R_{off}/R_{on} ratio	Persistence
$Gd_{0.1}Ce_{0.9}O_{2-\delta}$ (Figure 14.4a)		single	275	-	unstrained	1.48	volatile
$Gd_{0.1}Ce_{0.9}O_{2-\delta}/Er_2O_3$ (Figure 14.4b)		6	61	30	-0.61%	2.00	volatile
$Gd_{0.1}Ce_{0.9}O_{2-\delta}/Er_2O_3$ (Figure 14.4c)		40	9	4.5	-0.74%	5.39	volatile
$Gd_{0.1}Ce_{0.9}O_{2-\delta}/Er_2O_3$ (Figure 14.4d)		60	6	3	-1.26%	14.94	non-volatile

15   Conclusions

The results show a new, exciting way to use multilayered heterostructure oxides as a functional building block to control the degree of biaxial strain in ionic conductors, and demonstrate for the first time their direct implication for devices with tuned memristive properties by strain. The resistive switching and memristive behavior could be changed from volatile to non-volatile memristance upon strain modulations in the conducting phase of the heterostructure oxide units on the example of $Gd_{0.1}Ce_{0.9}O_{2-\delta}/Er_2O_3$ materials. The successful decrease of the microdot size by one order of magnitude compared to state-of-the-literature to reach an electrode separation of 2.5 microns, yielding electric field strength of up to 80 MV/m, allowed accessing the property of "memristance" for strained multilayer heterostructures. The systematic and successful increase of strained volume in the $Gd_{0.1}Ce_{0.9}O_{2-\delta}$ phase of the heterostructure microdots was proven by Raman microscopy together with DFT simulations to interpret the experimental results. Raman mapping was used as a novel method to locally relate the chemical mapping of the material and strain states to the device structure. The results obtained by Raman microscopy and complementary TEM analysis clarify that local strain relaxation could be observed within the low interface count sample in the conducting phases of the heterolayer dots. We reveal that for the high number of interfaces, tuning the repetitions of ceria and erbia layers down to 3 nm, the increased biaxial strain distortion results not only in a modulation of the ionic conductivity primarily through the changed migration barriers, but also the electronic mobility *via* strain induced enhanced electronic mobility. Furthermore, the defect concentration at the interfaces is increased with greater strain levels. We provide a successful integration and design of strain levels and lattice biaxial distortion to tune the charge carrier transport in an ionic heterostructure oxide, and demonstrate their direct implication as novel microdot devices to modulate the property of memristance. The presented materials design concepts and insights are useful to make new architectures for micro-electrochemical devices beyond classic doping strategies, not only for digital information storage applications based on

memristance but also for related fields such as energy harvesting and storage devices.

PART IV
Influence of Electrode Symmetry and Electroforming on Resistive Switching of Structured Memristive Devices

16 Abstract

Restive switching memories operating on ionic carriers are considered as potential next generation memristor storage-class memories to replace electronic transistor memory technologies. In a classical arrangement, resistive switching devices consist of a switching oxide sandwiched between two metal electrodes arranged in a cross-plane geometry. Importantly, one electrode is in contact with the substrate while the other electrode is exposed to the atmosphere or a capping layer, resulting in an inherent asymmetry for most memristive devices. It is debated how the intrinsic asymmetry in oxygen exchange and varied interfacial defect states of the electrode-oxide interfaces *vs.* the initial electroforming may affect the resistive switching property. Here, we present a unique model experiment to study solely the implication of electroforming for a totally symmetric device through an in-plane microdot oxide design with sideways attached electrodes. Thereby, we can study the implication of electroforming on resistive switching at realistic local electric field strengths. For this, we study the influence of electroforming on symmetric $Gd_{0.1}Ce_{0.9}O_{2-\delta}$ thin film devices and $Gd_{0.1}Ce_{0.9}O_{2-\delta}/Er_2O_3$ multilayer devices. Here, the symmetry break, which is artificially introduced through electroforming at varied polarity, is replicated in the current-voltage curves and the subject of further analysis. Changing the electroforming polarity flips the memristive response with a mirror plane at zero volt. Analyzing the R_{off}/R_{on} ratios of the hysteresis allows us to observe that the resistance ratios remain the same with different electroforming polarities, *i.e.* positive and negative, for both the $Gd_{0.1}Ce_{0.9}O_{2-\delta}$ and $Gd_{0.1}Ce_{0.9}O_{2-\delta}/Er_2O_3$ samples. The shapes of the curves, *i.e.* the position of the large R_{off}/R_{on} areas and additional crossings can also be reproduced at different polarities through our electroforming experiments. An important observation is that through electroforming with a long and strong bias pulse we modulate actively the number of defects in the system. Based on the symmetric model microdot resistive switching structures, we conclude that the underlying processes for transport remain the same, but the degree of reduction in the conductive phase of the switch depends on the effective electroforming initially applied to the symmetric device structures. EELS is being employed to

investigate the interfacial reduction states and a preferential reduction at the interfaces can be confirmed. Since the exchange with the environment, electrode interfaces and oxide microstructure remain the same for both cases of electroforming with positive and negative electroforming, the strong asymmetry present in the resistive switching response is given by the initial electroforming bias and polarity. Electroforming introduces a strong asymmetry on the resistive switching property by affecting the reduction state of the mixed conducting oxide which defines how many defects are present for the ionic transport of the resistive switch. We gain deeper understanding about the role of electroforming in symmetric devices and correlate this to a model where the symmetric electroforming response is explained through a reduction of the interfaces of the oxide. Ultimately, the study provides new insight into the connection of electroforming and device symmetry to alter the property of resistive switching, exemplified for ceria-based oxides.

17 Introduction

In the last decade oxide-based resistive switches have gained considerable attention as potential candidates for next-generation memories replacing current transistor-based technologies[18,21,200,204]. Most memristive devices consist of a resistive switching thin film sandwiched between two metal electrodes in a conventional cross-plane geometry, where the first electrode is deposited on a substrate, and on top of this first metal layer the thin film switching oxide is placed[25,205,231]. Therefore, it is inherent for this commonly employed cross-plane design that an *asymmetric electrode design* is present in terms of microstructures and oxygen exchange reactions with the environment. One electrode is always buried under the thin film, while the other one is exposed to the atmosphere[232,233]. Here, the thin film growth mode can be responsible for differences in microstructure within the extent of the resistive switching thin film, *e.g.* a gradient in grain boundary density. This may result in a changed defect density profile at the bottom electrode when compared to the counter top electrode. Such asymmetries are also present in packaged devices, since one electrode is exposed to the capping layer, while the other electrode is in contact with the substrate. Further, the electrodes, even when the same materials are selected, may also differ by the sequence of their deposition during sample fabrication. For example, the electrode interfaces may vary with respect to being grown either on the substrate or on the oxide for a cross-plane switching device geometry. The density of grain boundaries and dislocations may differ for the part of the oxide being directly deposited on the bottom electrode whereas the grain boundary density is different close to the second electrode deposited on top of the oxide[234].

An important aspect is that in many devices an electroforming (also called preforming) step is necessary to activate resistive switching; this applies to all classes of resistive switches, *i.e.* valence change memories, electrochemical metallization cells and thermochemical memories[235]. This electroforming step requires very often higher voltage, higher current or a longer duration than the subsequent, regular switching process for the operation of the memristive switch as memory or computational unit. The memristive switching device is often set to a state of higher conductivity

during and after the electroforming process. In filamentary-type devices a conductive filament or a reduced pathway is formed in the oxide during the electroforming step[236-238], and in the subsequent switching the charge carrier transport is taking place in this higher conductivity region. We refer here to the work of Yang and Williams[238] where they investigate the role and mechanism of electroforming in TiO_2 based devices in a cross-plane device geometry with different interfaces, one ohmic and the other one Schottky-like. They study the mechanism of electroforming and the role of different polarities during electroforming and find that the device is controlled by the as-deposited asymmetries and that the formation of conductive channels *via* oxygen vacancies is responsible for the switching process. They also discuss the role of oxygen gas evolution during electroforming. In the work of Kwon et al.[236] the formation and disruption of titania-magneli phase is identified to be responsible for the resistive switching behavior. In other cases it was also observed that electroforming in iron oxide sets the device into a state of lower conductivity[239]. Electroforming is required to either create defects that can act as charge carriers later, accumulate them at interfaces or reduce the material. This creates a state that is thermodynamically frozen, *i.e.* not in its equilibrium but kinetically hindered, and imposes differences in the later switching characteristics, although the device design does not necessarily reflect such asymmetries.

There is a fundamental interest to study symmetry breaks in memristive devices, be it either to be used as a design tool or a property that needs to be well controlled to have good reproducibility in the devices. In multi-terminal stacked devices asymmetries can be amplified and could be used to create different input-output responses through *e.g.* electroforming, while keeping the same fabrication process and device design. We refer to the work carried out in the groups of Ielmini[202], Leblebici[203] and Waser[240], where they demonstrate the usefulness of stacked and 3D devices.

Deliberate or inherent symmetry breaks in switching devices can actively be used as a design strategy to modulate device properties, *e.g.* through different electrode materials. Several asymmetric systems with respect to the switching direction were fabricated and measured in literature, see

Table 17.1, but so far only few studies, e.g. Yang et al.[238] and Jeong et al.[241] have directly targeted the effect and applicability of device symmetry and asymmetry for cross-plane geometries, respectively. To the best of our knowledge no studies were published on in-plane devices. This highlights that this topic is of great importance and could contribute substantially to the understanding of memristive devices.

Table 17.1: Asymmetric memristive material systems, where the device symmetry is broken on purpose by using different electrode materials (of varying work function) in contact with the switching oxide for cross-plane geometries.

Material System	Ref.
$Pt/TiO_2/Al$ $Pt/Ni/TiO_2/Al$ $Pt/Mn/TiO_2/Al$ $Pt/W/TiO_2/Al$	[241]
$Al/W/WO_x/AlO_y/Al$	[242]
$Ti/Gd_2O_3/Pt$	[243]
$Pt/ZnO/Pb(Zr_{0.52}Ti_{0.48})O_3/CoFe_2O_4/Au$	[244]
$Pt/SiO_x/TiN$	[245]
$Pt/Ta2O5-x/TiOxNy/TiN/Ta2O5-x/Pt$	[246]

Due to the abovementioned constraints of inherent asymmetry it remains challenging to study the effects of symmetry in resistive switching devices. As electroforming can define the thermodynamic boundaries set within which the resistive switching device is operated, it is doubtless that understanding of the processes involved is required to elaborate best switching device operation schemes. In-plane devices allow to design model experiments with devices that are completely symmetric in the switching direction. So far this has been challenging, since contacting issues had to be overcome and devices with a small electrode separation needed to be realized.

We fabricate symmetric memristive devices to investigate the role of symmetry breaks given by the initial electroforming applied to $Gd_{0.1}Ce_{0.9}O_{2-\delta}/Er_2O_3$ multilayer memory structures. Conventional devices have many sources of asymmetries, *e.g.* microstructure, exchange

reactions with the environment, or variations in defect density and distribution, see Figure 17.1a and Figure 17.1b. In this study we demonstrate a model memristive device that is strictly symmetric with respect to the electrode materials, their microstructures and the exposure to gas atmosphere along the switching direction. In the design employed in this work the switching oxide is fabricated as a microdot onto a sapphire substrate and the metal electrodes are attached sideways, whereby a unique "real" in plane switching device is realized. Making such a device that is strictly symmetric in the switching direction with respect to the abovementioned, symmetry-breaking elements and fabrication challenges is complex and was not achieved so far.

In the present work we study a memristive device with *a symmetric electrode design* and this allows us to investigate the influence of electroforming and symmetry on the resistive switching characteristics. Ultimately, the results contribute to the understanding of the role of electroforming in symmetric devices and show new ways how this knowledge could be used to introduce new oxide architectures for memory or computational hardware components operating on memristance.
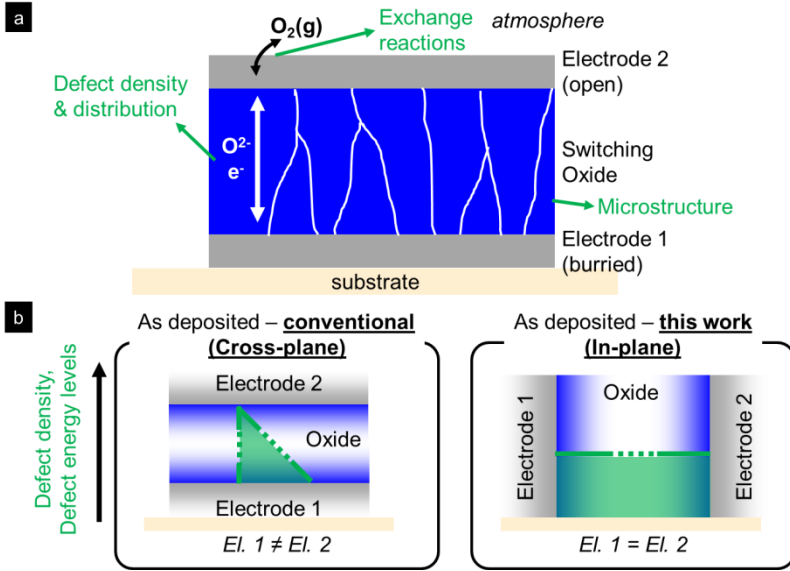
Figure 17.1: Sample and experimental design. a) Schematic side-view of a vacuum grown cross-plane design memristive device. There are different sources of asymmetry, e.g. the electrodes, leading to a modulation of exchange reactions with the environment (atmosphere); growth induced microstructural variations or variations in the defect density and defect energy levels. b) Left side: In conventional devices most of these asymmetries are inherently present. Right side: In the devices presented in this work an in-plane device design is employed eliminating potential sources of asymmetry.

18   Methods

18.1 Sample Fabrication

The thin films and multilayered thin films with a thickness of approximately 275nm were fabricated by Pulsed Laser Deposition (Surface Technologies, Germany; KrF excimer laser, 248 nm) on c-cut sapphire substrates (Stettler sapphire, Switzerland). The films were deposited at 700 °C at an oxygen pressure of 0.0267 mbar. The microdot structures were fabricated with standard photolithography methods and dry etching. First, a pattern was made using positive photoresist (AZ 4533). After dry etching to remove the excess material and create free-standing microdots negative photoresist (AZ 2020) was used to make a pattern for the contacting electrodes, see Ref.[209,237], Figure 18.1 and Supplementary Information 24.1for details on the microfabrication route. The Pt metal electrodes were deposited by e-beam evaporation.
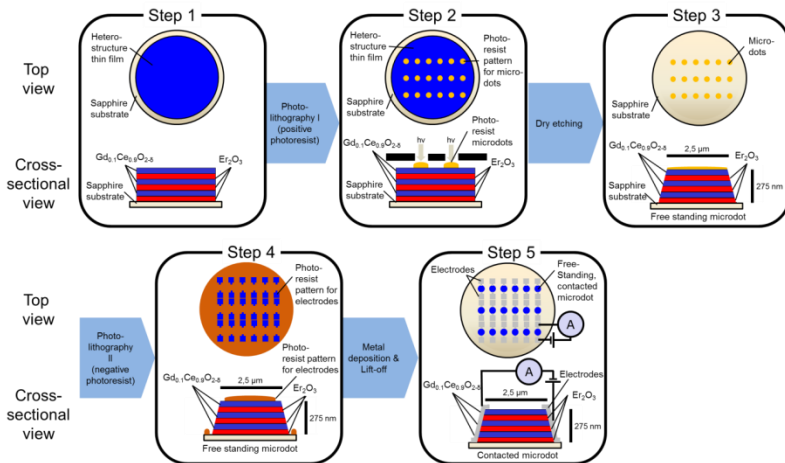
Figure 18.1: Microfabrication process flow to produce strained microdots contacted by electrodes for small dot sizes down to 2.5 microns in diameter.

18.2 Structural and Chemical Characterization

The thin films were characterized by X-ray diffraction (Bruker D8, Cu Kα) and confocal Raman microscopy (WITec alpha300R, WiTec, Germany, 532 nm). The microstructure was investigated with scanning electron microscopy (SEM, LEO 1530). Lamellas for TEM analysis were prepared using a FIB scanning electron microscope (Zeiss NVision 40). The annular dark field STEM images were recorded using a FEI Talos F200X operated at 200 kV.

18.3 Electrical Characterization

All electrical measurement were carried out using a Keithley 2612B source measurement unit (Keithley Instruments, USA), Pt needles and 3D micropositioners (Everbeing, Taiwan). The electroforming program consisted of a ramping step with a sweep rate of 1V/sec to a voltage of 200 V and then a dwell step of 3600 sec with a compliance current of 200 nA. If this compliance current was reached the applied voltage was

reduced accordingly. The cyclic voltammetry was carried out with a sweep rate of 500 mV/sec, an amplitude of ± 200 V and a compliance current of 200 nA.

19   Results and Discussions

The microdots used in this work are based on the either pure $Gd_{0.1}Ce_{0.9}O_{2-\delta}$ or a combination of the materials $Gd_{0.1}Ce_{0.9}O_{2-\delta}$ and Er_2O_3 in a multilayer design to tune the effective defects present in the switching oxide, see Ref.[237] for details. Such a symmetric switching device can be characterized through a mirror plane cutting the device in the middle; and can be realized as the electrodes are shaped by microfabrication after deposition at the same time and differ towards classic subsequently deposited resistive switching geometries, Figure 19.1a. Besides the advantages of allowing us to capture real strain effects at micrometer scale another striking feature of the microdot design employed here is that along the charge carrier flow direction, *i.e.* the switching direction, the device is strictly symmetric, see Figure 17.1b right side. This implicates that all asymmetries in the electric measurements stem from the treatments after sample (device) preparation and are not a result of unequal interfaces *i.e.* substrate-electrode *vs.* air-electrode. In other words, such a resistive switching symmetric architecture allows to study solely the implication of electroforming (applying a long and strong bias pulse at larger current magnitude) prior to the resistive switching operation. We test this hypothesis by applying different polarities during the electroforming procedure, as illustrated in Figure 19.1b. This design element that we can engineer gives us the unique opportunity to study the role of electroforming and asymmetry in oxide-based resistive switching devices with the same electrodes, oxide microstructures and defect states in the switching direction for a given material.
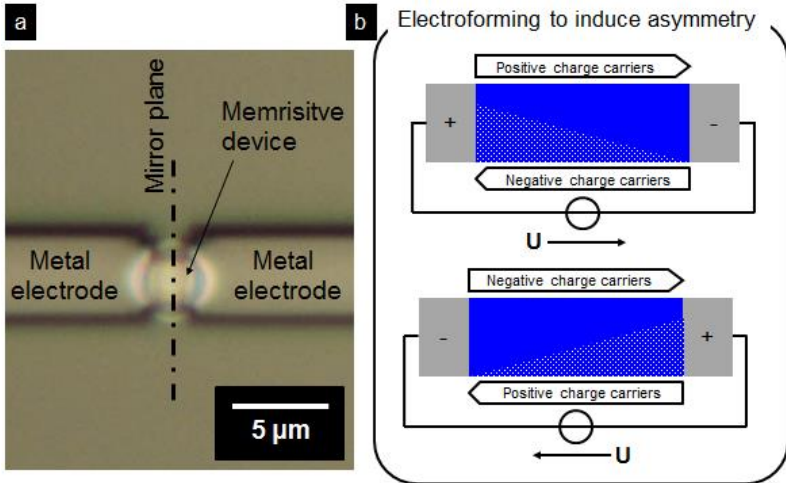
Figure 19.1: Symmetric devices and the application of electroforming to induce asymmetry. a) Optical micrograph of a microdot memristive device. b) The symmetry imposed through device design can be studied via a deliberately induced symmetry break, in this case electroforming with different polarities is used.

Electroforming is the one-time application of a high current or voltage leading to a breakdown of the material. Very often this is needed to increase the defect density, *e.g.* the oxygen vacancy concentration, which in turn results in the formation of conductive filaments and sets the device into a low resistance state[238]. In the present study a voltage of 200V was applied, corresponding to a field strength of $8*10^7$ V/m. A compliance current of 200 nA was set. If no compliance current was set the device failed after reaching very high current levels, usually resulting in electrode delamination.

The electroforming procedure was deemed successful when the current was still at the compliance value after the full electroforming period of the ramping time and one hour dwell time, this means the device didn't fail and the electrodes were still intact. Device failure was usually characterized by a steep and sudden increase in resistance.

The electroforming program is shown in the top section of the first column of Figure 19.2, the bottom section of the first column displays the corresponding electric response. This experiment was carried out for the sample design consisting of a single phase $Gd_{0.1}Ce_{0.9}O_{2-\delta}$ thin film and for the 60 interfaces $Gd_{0.1}Ce_{0.9}O_{2-\delta}/Er_2O_3$ design. To deliberately introduce asymmetry the two systems under investigation were subject to electroforming with either positive or negative polarity, with respect to a specific electrode. As shown in the first column of Figure 19.2, the positive and the negative electroforming yield a similar response, which is characterized by a slow increase in current during the voltage sweep, followed by a sudden change in conductivity after ~150 sec. Then the current reaches a level where it runs into the set compliance current. After successful electroforming as described above we studied how different polarities during electroforming change the memristive response of the microdots, *i.e.* the current-voltage (*IV*) profiles. The memristive behavior of the samples was investigated using cyclic voltammetry[247].

A voltage of positive polarity was applied, and was subsequently swept up to a maximum voltage of 200V and then cycled to the opposite polarity. The cyclic voltammetry experiments revealed that the *IV* curves for positive and negative electroforming polarity have the same basic shape, but are mirrored as zero volts. Taking a closer look at the shape of the curves of the 60 interfaces sample we can see that after electroforming with positive polarity, Figure 19.2a, 2nd column, a large hysteretic opening prevails, *i.e.* a large R_{off}/R_{on} ratio at the positive side, which is also the side of the applied electroforming at positive polarity. On the negative side the hysteretic opening is smaller than on the positive side with a crossing at ~85V. For electroforming with negative polarity, see Figure 19.2b, we can observe the large R_{off}/R_{on} ratio on the negative side. On the positive side we can observe a crossing at approximately 100V. The current at the crossing is for both cases ~ 2.5 nA. The R_{off}/R_{on} ratios are approximately around 15 and 18 for positive and negative electroforming, respectively; see Supplementary Information 25.1.

Conducting the same experiment with the $Gd_{0.1}Ce_{0.9}O_{2-\delta}$ single phase sample yields the same results, Figure 19.2, third column. The memristive

profile displays a small hysteretic opening at the side of the electroforming polarity and a larger hysteretic opening at the side of opposite polarity. Similar current-voltage characteristics, only mirrored at zero volt are observable for the opposite polarity. Here it should be mentioned that the $Gd_{0.1}Ce_{0.9}O_{2-\delta}$ single phase samples are selected as an example for volatile hysteretic current-voltage characteristics, for a detailed discussion see Ref.[237]. This allows us to confirm the same symmetry-dependent charge carrier transport behavior for operation at different time scales. The R_{off}/R_{on} ratios are equivalent for different electroforming polarities, see Supplementary Information 25.1.
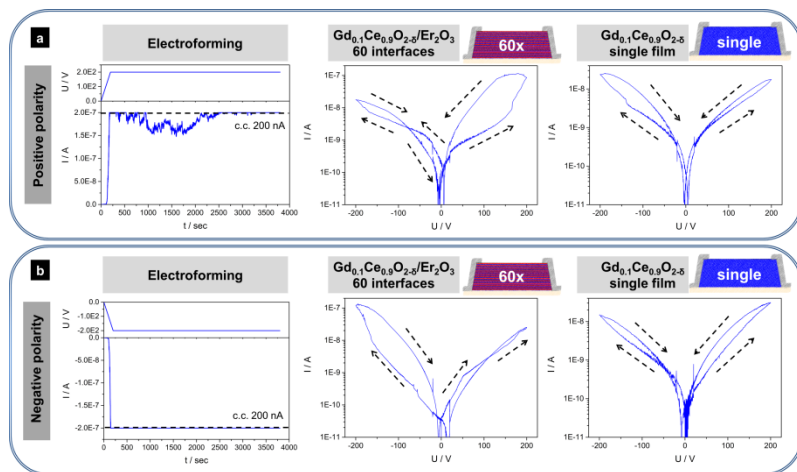
Figure 19.2: Memristive characteristics after electroforming at different polarities. a) Electroforming with positive polarity. The first column shows the general electroforming program and response, the second column the current-voltage curve of a 60 interfaces $Gd_{0.1}Ce_{0.9}O_{2-\delta}/Er_2O_3$ sample and the third column shows the current-voltage curve of a GDC single film microdot device. b) Electroforming with negative polarity. The first column shows the general electroforming program and response, the second column the current-voltage curve of a 60 interfaces $Gd_{0.1}Ce_{0.9}O_{2-\delta}/Er_2O_3$ sample and the third column shows the current-voltage curve of a GDC single film microdot device.

Since the two cases of electroforming at different polarity exemplified for two different material systems with their distinctive persistence characteristics are only different in their polarity during electroforming, we can conclude the difference in the current-voltage curves, which can be described by a mirror symmetry at zero volt which stems only from the electroforming. Other symmetry breaks along the electrical switching direction are not present in the microdot switches, and therefore cannot influence the memristive characteristics. After successful demonstration, that electroforming induces the symmetry break in the current-voltage profile of the switch we turn to EELS to carefully investigate the redox state of the ceria conductor material in the resistive switch. Through local

EELS mapping, the ratio of the Cerium-M_5 and Cerium-M_4 peaks, measured at the interface and in the bulk, confirms a reduction of ceria towards the secondary oxide interfaces[129,248], resulting in an increased defect density close to the interface, see Figure 19.3.
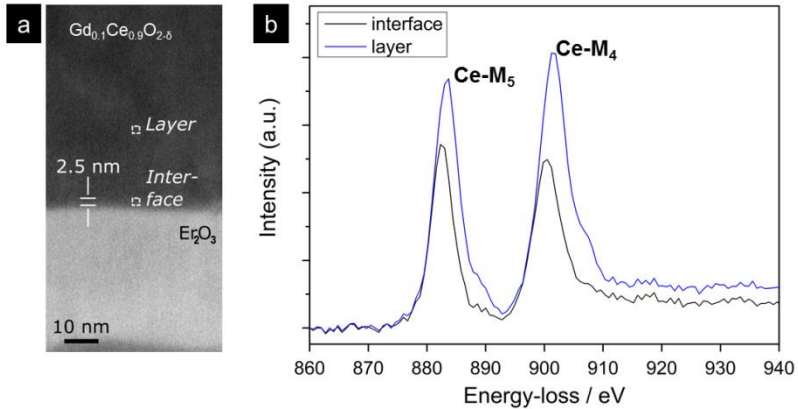

Figure 19.3: EELS of a $Gd_{0.1}Ce_{0.9}O_{2-\delta}/Er_2O_3$ multilayer sample. a) Micrograph of the specimen showing the measurement spots. b) Comparison of the spectra at the interface and within the layer (bulk) reveals the reduction of the cerium ions at the interfaces.

Electroforming is required to obtain reliable and reproducible results for this type of device, Figure 19.4. This holds for the single thin films samples, Figure 19.4a and the 60 interface samples, Figure 19.4b. Before electroforming the measured currents are one to two orders of magnitude lower than after electroforming. We ascribe this to an increase density of defects, caused by an electrochemical reduction of the conducting ceria phase, preferably at the interfaces. The non-electroformed resistive switches and their profiles display only very small hystereses with some capacitive characteristics, Figure 19.4, second column. For the 60 interfaces non-electroformed sample, no additional crossing can be observed. The additional crossing emerges only after electroforming.
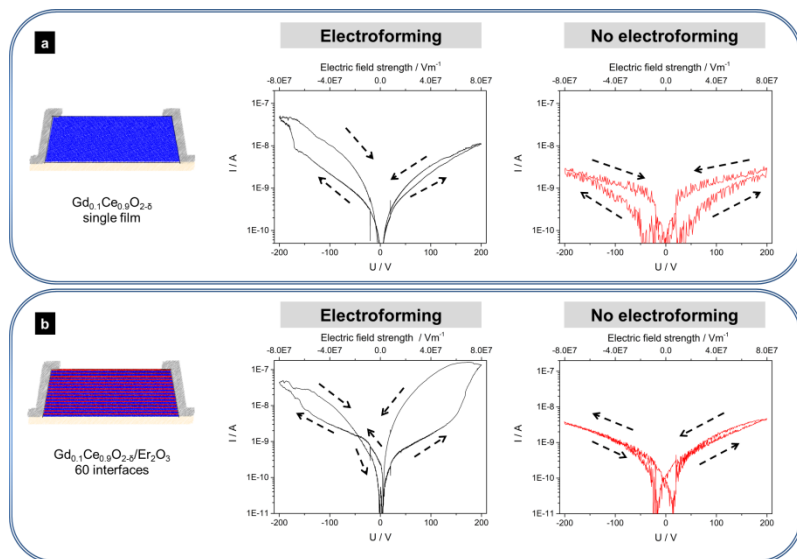
Figure 19.4: Electroforming characteristics of symmetric resistive switching devices. a) Change after electroforming for the $Gd_{0.1}Ce_{0.9}O_{2-\delta}$ single thin film sample. b) Change after electroforming for the $Gd_{0.1}Ce_{0.9}O_{2-\delta}/Er_2O_3$ 60 interfaces sample

The memristive behavior is mediated by electronic and ionic charge carriers[120,130,131]. During the electroforming process the ceria layer is undergoing additional reduction. This is in parts in agreement with other findings in the field, for example where a higher fraction of Ce^{3+} present at interface is reported by Song *et al.*[129] and Chueh *et al.*[229]. In the present case the thickness and extent of the reduced layer is increased through electroforming.
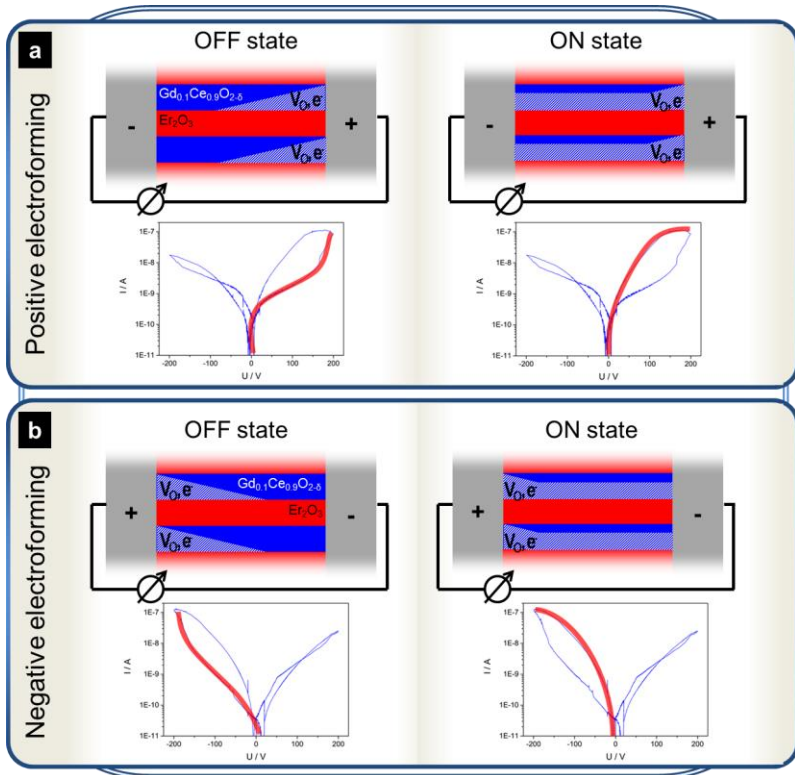
Figure 19.5: Model of the OFF/ON states as a function the changed electroforming polarity. In the OFF state the interface does not form a continuous boundary layer (filament) between the electrodes. In the ON state a continuous reduced filament of ceria spans between the two eelctrodes. This holds for the the case of a) positive electroforming and b) negative electroforming, leading to the mirrored memristive response.

Based on the electrochemical results and first EELS/TEM confirmation, we interpret the role of electroforming on symmetric resistive switches based on ceria as follows: During electroforming electrons are injected into the system from the side of positive polarity, leading to an enlarged, electrochemically reduced interface boundary layer at this electrode, resulting in an increased density of the electronic charge carriers. While the voltage is increased during the sweep, the ionic and electronic charge

carriers are migrating to the electrode with opposite charge, resulting in a decrease in resistance, see Figure 19.5. In the electroformed samples the reduced portion of the oxide interface has been enlarged, resulting in only a small part of the cerium oxide that has to undergo reduction during the voltage sweep. In other words, a non-uniform density gradient of charge carrier concentration is established between the two electrodes. When reversing the polarity the reduced portion is being reoxidized. Depending on the concentration of the non-reduced cerium oxide (Ce^{4+}), *i.e.* the non-interfacial portion of $Gd_{0.1}Ce_{0.9}O_{2-\delta}$, the reoxidation happens faster if more $Gd_{0.1}Ce_{0.9}O_{2-\delta}$ is available. The CeO_2 portion of the thin film layer, which is larger in the $Gd_{0.1}Ce_{0.9}O_{2-\delta}$ single film sample compared to the multilayered system, is acting as oxygen reservoir; thereby, also facilitating the volatile behavior in this sample, see Figure 19.6. In the material system investigated the strain state of the conducting oxide also plays a role. In this case we have compressive strain in ceria, leading to a decrease in ionic conductivity[209], also facilitating the slow reoxidation through ionic transport in the high interface count sample.
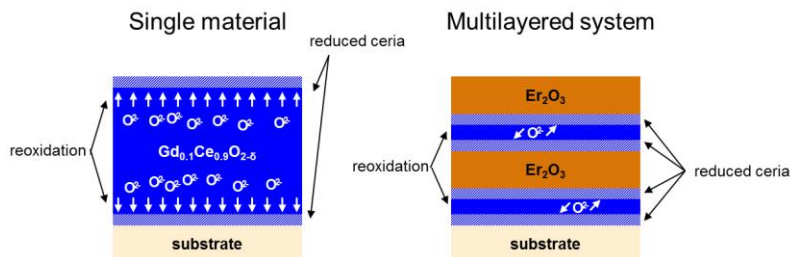

Figure 19.6: Reoxidation of reduced ceria. Larger volumes of ceria support the fast reoxidation of Ce^{3+} rich portion of the conducting oxide.

20   Conclusions

In this study we demonstrate a model experiment to study the role of electroforming for a totally symmetric in-plane resistive switching (memristive) device. Choosing the oxide switches to be microdots with sideways attached electrodes gives the unique opportunity to reach the needed high electric field strengths to induce switching but keep totally symmetric electrode-oxide interface in terms of their defects at interfaces and oxygen exchange with the environment. The resistive switching property can be studied electrochemically solely with respect to the applied initial electroforming which is the matter of investigation. Here, two model microdot oxide structures based on various interface modulated ceria heterostructures in terms of their defect densities have been selected. In general, the occurrence and reaction of electroforming is studied for resistive switches with either volatile or non-volatile characteristics by choice of the switching oxide, being either $Gd_{0.1}Ce_{0.9}O_{2-\delta}$ or multilayered $Gd_{0.1}Ce_{0.9}O_{2-\delta}/Er_2O_3$. We demonstrate that in-plane microdots can be used to create a model case for which the resistive switch has a high level of "symmetry" given by *i)* the microstructures and defects at the exposed and buried electrode interfaces and *ii)* towards the oxygen gas exchange with the atmosphere. Through this approach we can study the effect of electroforming on the evolvement of the current-voltage profiles for the switches. The electroforming process is carried out at different polarities, *i.e.* either positive or negative bias applied. Actively reversing the polarity allows to demonstrate that this change in polarity during preforming is implemented into the hysteretic memristive current-voltage response depends on the initial electroforming polarity for its switching and effective magnitude: we observe for the non-volatile resistive switches based on multilayered $Gd_{0.1}Ce_{0.9}O_{2-\delta}/Er_2O_3$ a mirror plane at zero voltage in the current-voltage profile, *i.e.* where the polarity changes its sign from positive to negative. The shapes of the curves display a hysteretic opening with a large R_{off}/R_{on} ratio at the polarity of electroforming and an additional crossing at the opposite polarity. Exactly the same behavior is observable when the polarity is reversed, *e.g.* the hysteresis with large opening is mirrored from the positive side to the negative side. This confirms for the very first

time that for the given case of a strictly symmetric resistive switching device (or memristor) the major determining parameter of the resistive switching property is the initially applied electroforming and induced defects (*i.e.* reduction of the ceria-phase). Moreover, we show a high level of material, defect and interface processing as we demonstrate a successful inversion of the resistive switching profile in its resistance ratios in OFF and ON state, additional crossings and shape of the hysteretic curves simply by exchanging the bias polarity at a fixed magnitude. On an atomistic level, we understand the process of electroforming such that the amount of reduced ceria is increased in a given conductor phase, modulating the number of ionic and electronic charge carriers. Subsequently, the density and mobility of these defects drives the resistive switching process; hence, the electroforming is for the given material a necessity and determines the switch characteristic. On a broader scale, one may see here analogies between freezing defects by electroforming (under a high electric field strength) in the material and to what is done in a classic temper and quench step, defining the thermodynamic boundary conditions of any oxide ceramic conductor. Through the deliberately introduced element of a symmetry break, which was electroforming at different polarities, we were able to demonstrate that this artificial asymmetric element has impact on the resistive switching characteristics. By doing so, we exclude that differences in the microstructure and/or exchange reactions with the environment between both electrode-oxide interfaces drive the changes in this in-plane devices; it is solely the electroforming process as presented for the given case of ceria-based resistive switches and memristors.

PART V
Summary and Outlook

Here the outcome of this PhD thesis and its impact on the scientific community is discussed and analysed in a broader context. Also, questions that arose during this thesis but remain to be answered in the future are presented and discussed.

21 General Conclusion

The aim of this thesis was to investigate how interfacial effects in general and strain in particular could be employed to modulate the physical property of memristance. Based on a comprehensive literature review it was decided that a multilayer approach would be the most suitable strategy, since it allows to finely tune the strained volumes for oxygen ionic conductors. Two phases are grown on each other and the resulting lattice mismatch gives rise to strain. To have a model that allows a clear assignment of the induced changes of the conductivity it was decided to have one phase that is an electric insulator while the other phase is assigned to be an oxygen ionic conductor. This way it can be safely assumed that all the current flows through the conductor and the number of variables that can play a role in the model has been reduced. The materials couple can be selected to result in compressive or tensile strain in the conductor phase. Considering current resistive switching models it is still not clear whether lattice compaction or lattice tension would yield the better results.

The materials that were selected as ionic conductor and insulator were $Gd_{0.1}Ce_{0.9}O_{2-\delta}$ and Er_2O_3, respectively. This material pair yields compression in the $Gd_{0.1}Ce_{0.9}O_{2-\delta}$; therefore, one expects a decrease in ionic conductivity in this material system for the in-plane direction. Samples were successfully fabricated with PLD and optical photolithography, first with an electrode distance of 15 μm, later with 2.5 μm. To capture real strain effects the electrodes were attached sideways instead of using top electrodes. It was found that top electrodes to not provide reasonable results for the present case when trying to capture strain effects at the microscale trying to contact nanoscopic interfaces. To impose different magnitudes the total film thickness of all samples was kept the same at 275 nm, but different layer counts were fabricated. The

number of interfaces was varied from 6 to 60, yielding different magnitudes of compressive in-plane strain.

In Arrhenius-type heating experiments it was proven that the ionic conductivity was decreased and the activation energy was increased under compressive strain. A compressive strain value of -1.26% allowed us to decrease the electrical conductivity by 75% and to increase the activation energy of ionic conduction by Δ0.31 eV. Based on these promising results the 2.5 μm devices were used for testing of the memristance modulation, since a certain electric field strength is required to observe memristance. The strain values were probed with Raman spectroscopy analyzing the shift of the F_{2g} Raman mode of the ion conducting $Gd_{0.1}Ce_{0.9}O_{2-\delta}$ phase.

It was tested if electroforming is required for operation as memristive device and it was indeed found that electroforming is beneficial, since it increases the current measureable by one to two orders of magnitude. Also, without electroforming the shape of the *IV* profiles shows no memristive modulation, revealing that not only a decrease in resistivity is the consequence of electroforming, but also the occurrence of memristance. With our strain and interface aided design approach we could modulate the R_{off}/R_{on} ratio by one order of magnitude. The otherwise volatile hysteretic characteristics were found to be non-volatile for the highly-strained 60 interfaces sample.

One distinctive feature of the device design employed is that it is strictly symmetric, which gave the opportunity to study the role of electroforming and symmetry on resistive switching. It was found that a deliberate break in symmetry is exactly represented in the IV curves. Electroforming at positive and negative polarity has been employed to break the symmetry and this results in an electric mirror plane at zero Volts.

To assess the in-plane strain states Raman microscopy mapping was applied to the oxide microdots and their multilayers for the device structures. This allows us to directly connect a change in lattice modulations imposed through lattice mismatch to a strain value. At first, we compared our results to experimental data to get a good estimation of

the strain values but later we employed DFT calculations to get more precise values.

To confirm our results with an independent second method we decided to use high resolution transmission electron microscopy. After preparing the TEM lamellas with FIB cutting we measured the $Gd_{0.1}Ce_{0.9}O_{2-\delta}$ spacing at the interfaces and at the center of film for the $Gd_{0.1}Ce_{0.9}O_{2-\delta}/Er_2O_3$ 60 interfaces sample and the $Gd_{0.1}Ce_{0.9}O_{2-\delta}$ single film sample. The results confirmed that compressive in-plane and tensile out-of-plane strain is imposed in the $Gd_{0.1}Ce_{0.9}O_{2-\delta}$ films. A strain gradient from the interface, where the strain field originates, to the film interior was measured and strain relaxation within the conductor films proven.

EELS was used to investigate the interfaces. It was found that the ceria at interfaces is preferentially reduced. A higher interface count leads in total to a larger portion of interfacial volume, resulting in a larger portion of reduced ceria as the lattice structure goes from cubic isotropic to a strained state.

Concluding, a new strained memristive device is demonstrated. New fundamentals on fabrication, contacting and measurement methodology were established. A proof-of-concept of this novel device architecture is shown and could be further miniaturized for commercialization.

22   Outlook & Future Challenges

Ultimately, the thesis contributed in understanding the relationship of strained interfaces and electric transport, particularly at moderate temperatures and high electric fields. This can be used for the fabrication of memristive devices, as demonstrated here through sideways contacted multilayer oxide microdots. Even though it was successful to develop the new strained memristors based on oxide heterostructures, and hypothesis could be tested concerning the electric transport-structure-resistive switching properties in such materials and devices, there are still many topics to be explored and questions that we want to answer.

A deeper structural understanding would help to refine the models connecting strain, interfacial redox states and the related memristive response. Strain analysis using standard Raman microscopy is suffering from thermal broadening and using a cooling stage with liquid nitrogen cooling would help to narrow the FWHM of the peaks and would therefore improve the peak separation, allowing a better strain determination.

To make the concept of using strain for memristive devices more relevant for high density application further downsizing would be required. However, the proof of concept given through this thesis and electrochemistry behind it can actively be used for further downscaling. To achieve this, e-beam lithography is suggested in the first patterning step where the microdot pattern is created on the multilayer thin film. A resist with a sufficiently low etching rate has to be selected or the device has to be thinner. Another option that would be enabled by a substantial decrease in size would be the application of electrochemical impedance spectroscopy. Using impedance spectroscopy to analyze the ON and OFF states for the in-plane microdots would allow getting a deeper understanding of the underlying mechanism. In the presented design of the strained microdots for resistive switches the usage of impedance spectroscopy was limited by the resistance of the samples and the high voltages required to reasonably investigate the ON and OFF state. Separation of electronic and ionic contributions would be an important

cornerstone for understanding the switching behavior in strain- and interface controlled multilayered systems based on mixed ionic-electronic oxides in the future. This could be achieved for example through oxygen partial pressure depended conductivity measurements and analysis of the Brouwer diagram. Another way would be ^{18}O tracer diffusion experiments, like previously carried out by Aydin *et al.*[74,95]. For optically active systems, *e.g.* Pr-doped ceria, absorption measurements could be used to track the oxidation state of the system[249].

In-situ TEM measurements to directly observe the resistive switching process would help to connect the electric transport data to structural changes (*e.g.* in redox state of the oxide) and actual mass transport in the device under bias. However, these remain challenging in sample preparation, measurement and data analysis Also one would have to keep in mind that the TEM lamella as resistive switch would be a scenario far from a real device structure due to its constrained volume after FIB-cutting.

It remains to be explored how tensile strain impacts on the modulation of memristance and tuning the electronic and ionic conductivities. Sm_2O_3 and Bismuth-Niobates seem to be promising candidates for the insulating phase, keeping the same approach of using $Gd_{0.1}Ce_{0.9}O_{2-\delta}$ as conductive phase and using the insulating phase to impose strain on the conducting strain. Different strain magnitudes can also be employed; *e.g.* by using Vegard's law in the Bismuth-Niobates; however, it seems advisable to remain in the elastic strain regime but still try to get a maximum of strain. Also the critical thickness for formation of dislocation has to be considered.

The present work was carried out on polycrystalline thin films. In order to get a better understanding for the role of grain boundaries and the grain boundary density it would be possible to grow epitaxial and grain boundary free thin films. That would allow taking the understanding of structure-transport relationships in strain- and interface controlled samples to a higher level.

In applications, a different sample design could be employed using the anisotropic strain behavior in thin films through a crosspoint design, where bottom and top electrodes are sandwiching a thin film. This means an in-plane compressive film could be used by exploiting its out-of-plane tensile strain. One would have to consider the use of a bottom electrode with the correct structure to ensure well-controlled growth.

PART VI
Appendix

23 Supplementary Information Part II: A Microdot Multilayer Oxide Device: Let Us Tune the Strain-Ionic Transport Interaction

23.1 Spatially resolved Raman scans of the micro-dot array

Raman spectra with respect to their spatial position on the specimen are displayed. The spot of the excitation laser was moved to the strained $Gd_{0.1}Ce_{0.9}O_{2-\delta}/Er_2O_3$ multilayer structure and to another randomly chosen spot on the surface that is not the metal electrode, as depicted in Figure 23.1. Figure 23.1a indicates the measured spots on the specimen. Figure 23.1b shows the spectrum obtained by measuring the free-etched surface of the sample. The spectrum clearly shows just the sapphire features. Figure 23.1c was measured on the $Gd_{0.1}Ce_{0.9}O_{2-\delta}/Er_2O_3$ multilayer structure and shows the known spectrum for these heterostructure.
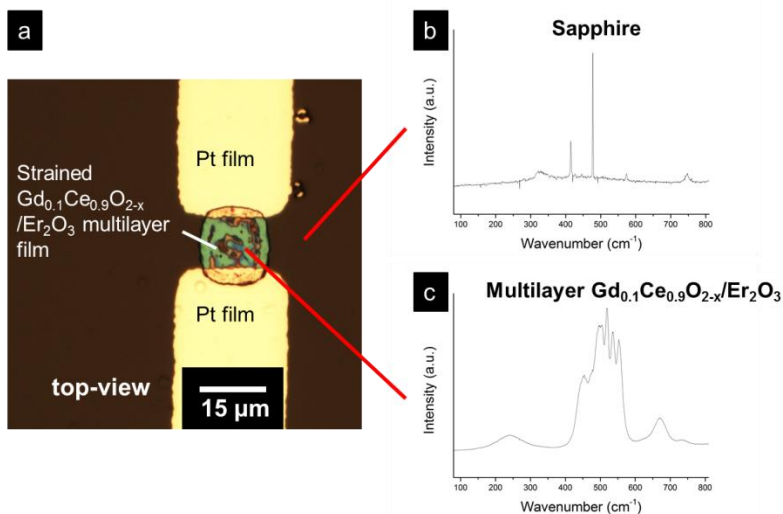
Figure 23.1: Spatially resolved Raman spectra of the multilayer micro-dots on the free etched surface. a) High-magnification light microscopy picture of a microdot contacted by side-wise attached Pt electrodes. The red lines indicate the spot where the Raman spectra shown in b) and c) were recorded. b) Raman spectrum of the free etched sapphire substrate. c) Raman spectrum of the micro-dot. The characteristic features of the $Gd_{0.1}Ce_{0.9}O_{2-\delta}/Er_2O_3$ multilayer can be observed.

23.2 Detailed XRD Scans

Detailed θ-2θ scans of all processed thin film samples were recorded and are displayed in Figure 23.2. All samples show a narrow FWHM and are well-oriented, with (111) or higher order orientations. Samples with a single layer film thickness < 9 nm for Er_2O_3 or < 18 nm for $Gd_{0.1}Ce_{0.9}O_{2-\delta}$ show superlattice modulation. The non-symmetry of the satellite peaks stems from non-perfect geometrical alignment of the specimens. The peak positions are in agreement with Refs.[161,162]. When going to a higher number of interfaces, *i.e.* the number of layers is increased we can observe a systematic shift of the peak positions.
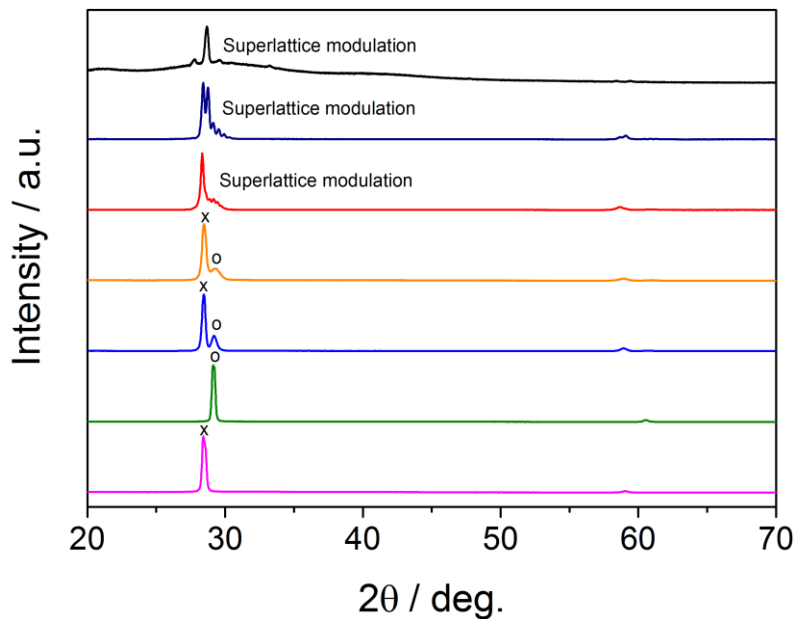
Figure 23.2: X-Ray diffractograms of all thin film samples. The numbers indicate the number $Gd_{0.1}Ce_{0.9}O_{2-x}/Er_2O_3$ of bilayers.

23.3 XRD patterns of pellets

X-ray diffractograms of the bulk ceramic pellets used for Pulsed Laser Deposition are displayed in Figure 23.3. The patterns show all characteristic peaks, indicating the correct phase and no impurities.
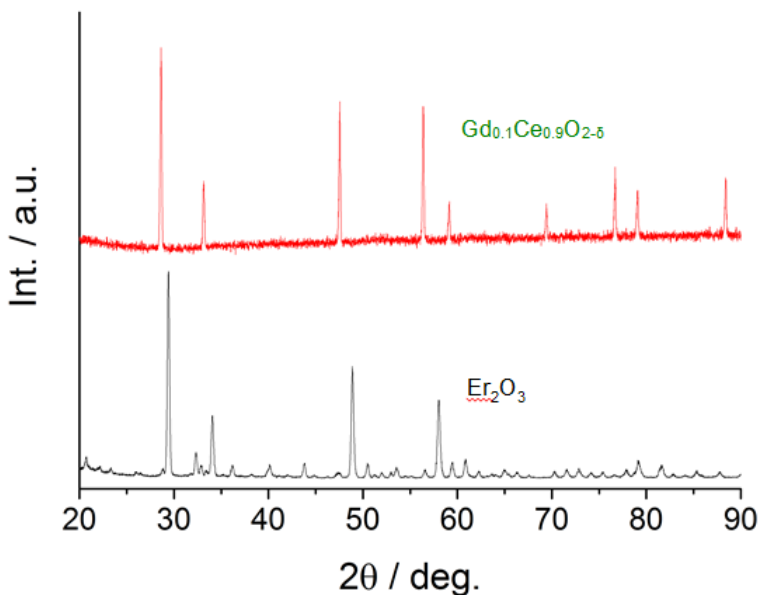
Figure 23.3: X-Ray diffractograms of the bulk ceramic pellets.

23.4 Comparison of Raman spectra of $Gd_{0.1}Ce_{0.9}O_{2-\delta}$ and Er_2O_3 of pellets and single thin film samples

Raman spectra of all pellet and thin film samples were recorded and compared to each other and to Refs.[168,172,174]. The pellet sample peaks match with the thin samples. For $Gd_{0.1}Ce_{0.9}O_{2-\delta}$ the peak could be assigned to the F_{2g} mode, see Figure 23.4. The peak is at the unstrained position (~463 cm^{-1}), which is at a higher wavenumber than the peaks tentatively identified in the spectra of the strained samples. For the case of Er_2O_3 the Raman spectra of bulk pellet and thin film sample match, see Figure 23.5. All the peaks could be assigned to F_g and F_g+A_g peaks or could be identified in Raman spectra of compounds with the same bixbyite structure. For all Raman measurements an experimental series with different laser energies was made to exclude influence from laser heating. The composition was the same for all samples, *i.e.* a shift of the Raman lines due to change of the composition can be neglected.
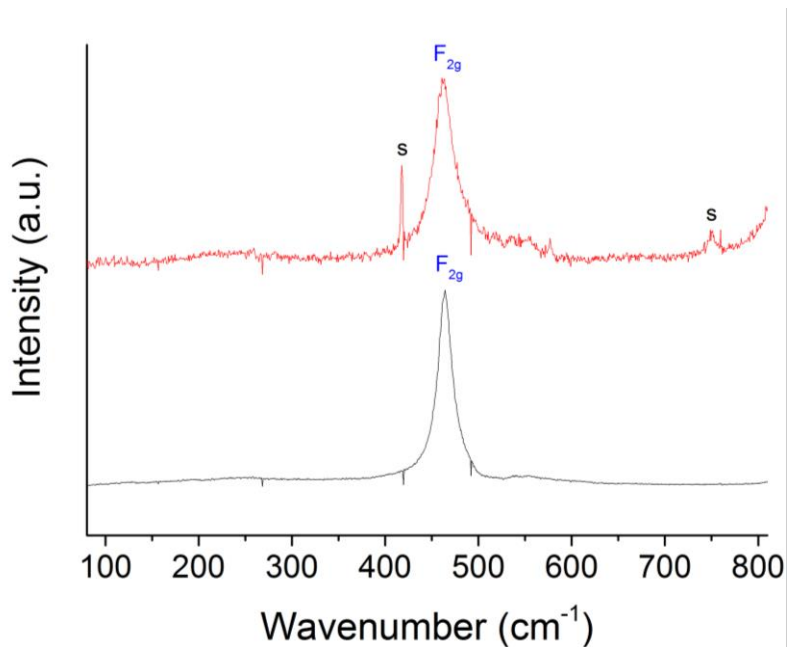
Figure 23.4: Raman spectra of the bulk pellet (black line) and single thin film sample (red line). The blue F_{2g} index marks the respective Raman mode of $Gd_{0.1}Ce_{0.9}O_{2-\delta}$. Both samples show a good match, the thin film sample shows sapphire features from the substrate.
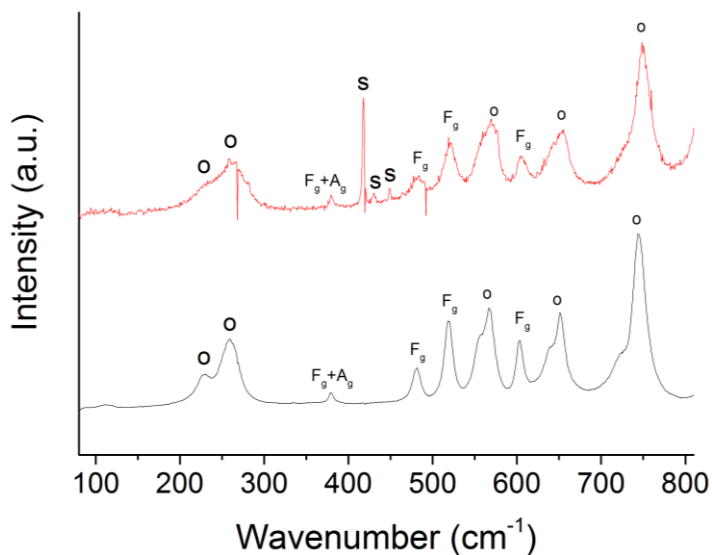
Figure 23.5: Raman spectra of the bulk pellet (black line) and single thin film sample (red line). The F_g and F_g+A_g index marks the respective Raman modes of Er_2O_3. The (o) index marks peaks that could be identified in similar bixbyite structures. Both samples show a good match, the thin film sample shows sapphire features from the substrate.

24 Supplementary Information Part III: Designing Strained Interface Heterostructures for Memristive Devices

24.1 Fabrication details

Compared to the state-of-the-art in literature[209] we were able to decrease the size of the devices by ~one order of magnitude. After thin film deposition in a PLD system (Figure 18.1, step 1), see **Table S1.1** for deposition rates, the samples were subject to a first photolithography step. This photoresist pattern was made with spin-coating AZ 4533 Photoresist (Microchemical, Germany) to achieve a thickness of 4.3 – 4.6 microns. After letting the sample rest and soft-bake with 100°C for 90 sec the sample was exposed in a MA6 mask aligner (SUSS MicroTec, Germany) with a dose of 190mJ/cm^2 at 405 nm (Figure 18.1, step 2). After resting the sample was post-baked with 115°C for 20 sec. After another resting period we developed the sample in 2 different puddles filled with AZ 826 developer with 39 sec in each puddle. Subsequently the sample was dried in an N$_2$ stream.

Then the microdots were subject to dry-etching using an Oxford Plasmalab 80 (Figure 18.1, step 3). The etching rates for the oxides and the photoresist were measured in previously carried out pilot experiments, see **Table S1.2**. AZ nLof 2020 was spin-coated onto the sample to create a pattern for metal deposition (Figure 18.1, step 4). Following a resting step the samples were soft-baked at 110°C for 180 sec followed by another resting period. The samples were then exposed at 365 nm with a dose of 75 mJ/cm^2. Another resting period was followed by a post-bake at 110°C for 90 sec. After a final rehydration the samples were developed in 2 puddles of AZ 726 for 45 sec each. The samples were dried in an N$_2$ stream and finally subject to metal deposition to fabricate the electrodes (Figure 18.1, step 5).

A process flow chart depicting the sample fabrication is shown in Figure 18.1.

Table 24.1: Thin film deposition rates

Material	PLD deposition rate / nm*100pulses^{-1}
Er_2O_3	~1
$Gd_{0.1}Ce_{0.9}O_{2-\delta}$	~2

Table 24.2: Etch rates

Material	Etch rate in Ar plasma / nm*min^{-1}
Er_2O_3	0.59
$Gd_{0.1}Ce_{0.9}O_{2-\delta}$	1.24
Sapphire	1.75
AZ nLof 2020	~10

24.2 HR-TEM diffraction analysis

Relative assessment of lattice spacing out-of-plane ([111]) and in-plane ([311]) was performed *via* Fourier analysis of atomic-resolution images of the 6 and 60 interface samples. Representative 101 zone axis diffractograms computed from $Gd_{0.1}Ce_{0.9}O_{2-\delta}$ in the 60 and 6 interface samples are shown in Figure 24.1a and b, respectively. Spot separation was measured 4 to 6 times (typically 5) depending on the number of high order reflections visible in the diffractogram. Standard error propagation was performed using the measured mean and standard deviation.
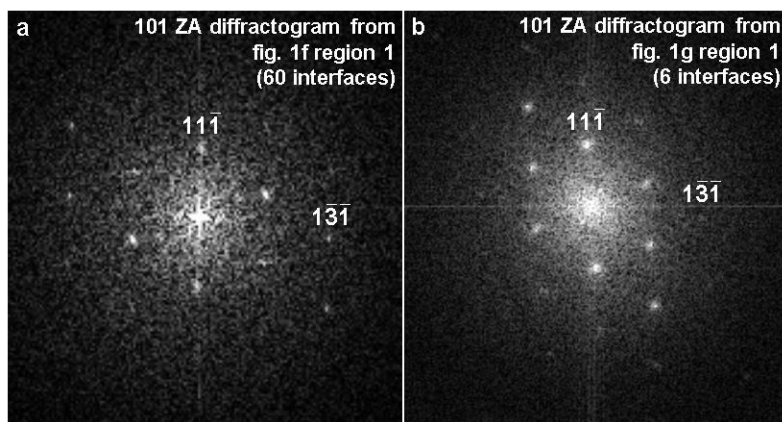

Figure 24.1: Typical 101 zone axis (ZA) diffractograms used for relative lattice plane spacing analysis. Diffractograms were computed from $Gd_{0.1}Ce_{0.9}O_{2-\delta}$ layers 60 and 6 interface samples.

The result of this analysis is detailed in Table 14.1, and reveals a relative contraction of the in-plane [311] spacing by 2.8 ± 0.2 % when comparing regions 1 and 2 in the 6 interface sample, Figure 14.2c**.** This result suggests the strain field relaxes within the several nanometers directly adjacent the interface.

24.3 XRD Structural characterization

The thin films were also characterized with X-Ray Diffraction in Bragg-Brentano configuration, Figure 24.2. The 6 interfaces sample shows the single peaks for both materials, $Gd_{0.1}Ce_{0.9}O_{2-\delta}$ and Er_2O_3. The 40 and 60 interfaces samples exhibit supelattice modulation.
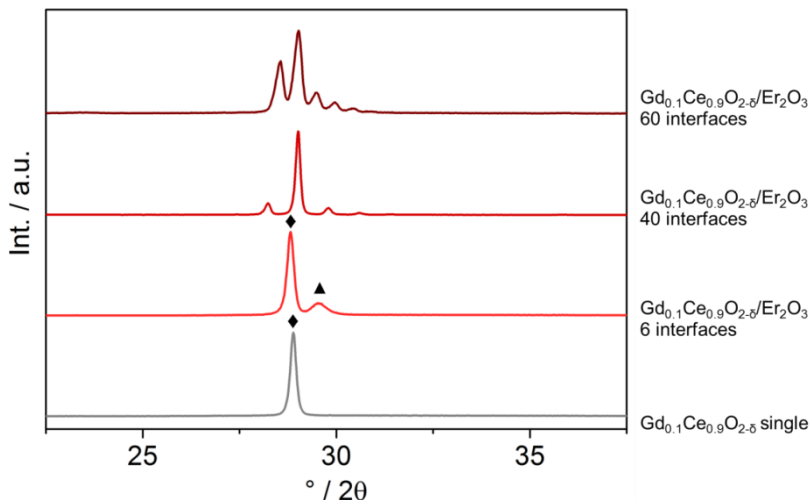

Figure 24.2: X-Ray diffractograms of the thin film samples. The diamond symbol refers to $Gd_{0.1}Ce_{0.9}O_{2-\delta}$ phase and the triangle symbol to $Er_2O_{3.}$

24.4 Scanning transmission electron microscope electron energy-loss spectroscopy

Dopant cation segregation at the interfaces was investigated in non-preformed samples using STEM EELS to track the intensity ratio of the Ce M_{45} and Gd M_{45} ionization edges. A negligible difference in the intensity ratio, $I_{M45}^{Ce}/I_{M45}^{Gd}$, was observed when comparing spectra acquired in the GDC layer ($I_{M45}^{Ce}/I_{M45}^{Gd} = 11.6 \pm 0.8$) and within 2.5 nm of the interface $I_{M45}^{Ce}/I_{M45}^{Gd} = 11.8 \pm 1.3$). The cited error is one standard deviation in the mean value measured at five locations along the interface. In the interface region (*i.e.* within 2.5 nm of the interface), cerium

reduction was typically observed as a reversal in the Ce M_5 to M_4 peak height ratio, and a slight shift of both peaks towards lower energy-loss[250].
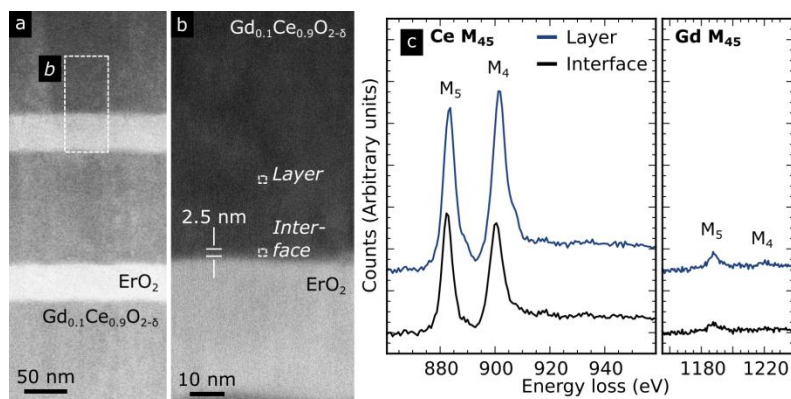

Figure 24.3:TEM and EELS measurements. a) Annular dark field (ADF) STEM image of $Gd_{0.1}Ce_{0.9}O_{2-\delta}/Er_2O_3$ multilayers. b) ADF STEM image of a single $Gd_{0.1}Ce_{0.9}O_{2-\delta}/Er_2O_3$ interface; the image was acquired in the region of a highlighted with a dashed box labeled b. c) Area-averaged Ce M_{45} and Gd M_{45} energy-loss spectra acquired in the $Gd_{0.1}Ce_{0.9}O_{2-\delta}$ layer 22 nm – 28 nm from the $Gd_{0.1}Ce_{0.9}O_{2-\delta}/Er_2O_3$ interface (Layer), and acquired within the 2.5 nm directly adjacent to the $Gd_{0.1}Ce_{0.9}O_{2-\delta}/Er_2O_3$ interface (Interface). The spectra labeled Layer and Interface were acquired in the regions of b highlighted with a dashed box with corresponding labels.

STEM EELS experimental details:

A JEOL 2010F STEM equipped with a Gatan Enfina energy-loss spectrometer was operated with an acceleration voltage of 200 kV. The probe size at the specimen was approximately 0.7 - 1 nm. Individual spectra were acquired with an exposure time of 0.5 s, and a spectrometer dispersion of 0.7 eV/channel. The convergence and collection semi-angles were about 15 mrad and 33 mrad, respectively. For spectral processing, spectra were shifted such that the Ce M_5 edge maxima had an energy loss of 883 eV. An inverse power-law fit to the background signal was used for background subtraction, and signal integration windows were selected to minimize specimen thickness effects (*e.g.* plural

scattering artifacts)[251]. Background fitting and signal integration windows are provided in the table below.

	Background fitting (eV)	Signal integration (eV)
Ce M$_{45}$	890 – 870	875 – 955
Gd M$_{45}$	1070 – 1170	1175 – 1255

24.5 Additional Raman Spectroscopy Theory

According to Ganesan *et al.*[252], the frequencies of the three optical modes can be described by the following secular equation:

$$\begin{bmatrix} p\varepsilon_{11} + q(\varepsilon_{22} + \varepsilon_{33}) - \lambda & 2r\varepsilon_{12} & 2r\varepsilon_{13} \\ 2r\varepsilon_{12} & p\varepsilon_{22} + q(\varepsilon_{33} + \varepsilon_{11}) - \lambda & 2r\varepsilon_{23} \\ 2r\varepsilon_{13} & 2r\varepsilon_{23} & p\varepsilon_{33} + q(\varepsilon_{11} + \varepsilon_{22}) - \lambda \end{bmatrix} =$$
$$0 \qquad\qquad\qquad\qquad\qquad\qquad\qquad\qquad\qquad \textit{Equation 24.5.1}$$

, where *p*, *q* and *r* are the phonon deformation potentials. The Raman frequencies for the strained and unstrained cases can be calculated from the eigenvalues λ.

$$\lambda = \omega_{strained}^2 - \omega_{unstrained}^2 \qquad\qquad \textit{Equation 24.5.2}$$

This can be rewritten as

$$\Delta\lambda = \omega_{strained} - \omega_{unstrained} \approx \frac{\lambda_{strained}}{2\omega_{unstrained}}. \qquad \textit{Equation 24.5.3}$$

Resolution:

The spatial resolution achievable with optical microscopy is given by

$$Spatial\ resolution = \frac{0.61 * \lambda}{NA} \qquad\qquad Equation\ 24.5.4$$

λ is the wavelength, in this case 532 nm, NA stands for the numerical aperture, which is for the given case 0.9, giving a spatial resolution of about 360 nm on average.

24.6 Raman Microscopy on Erbia

A Raman spectrum of an Er_2O_3 thin film on sapphire is presented in Figure 24.4. All Raman band assignments presented in Table 24.3 were assigned using Refs. [253-256]. A pilot experiment with varying laser powers was conducted to exclude influence from laser-induced sample heating.
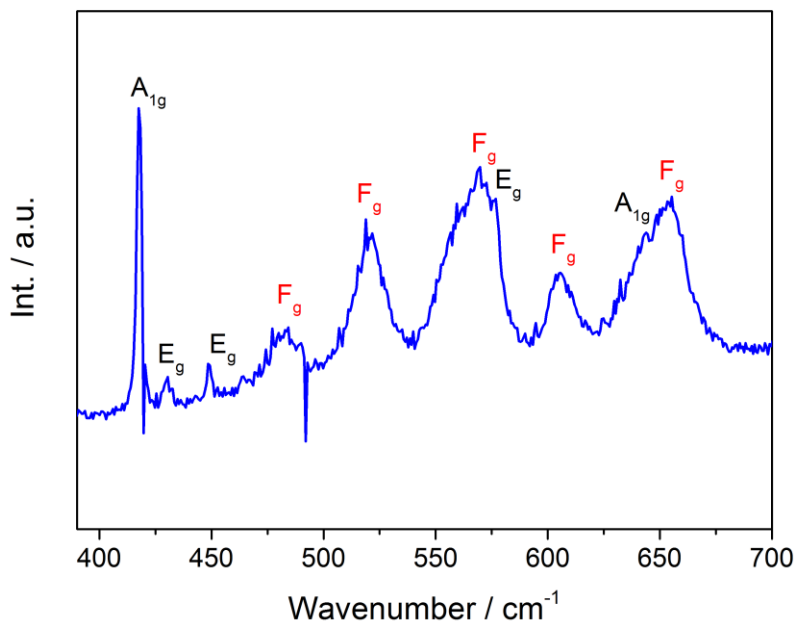

Figure 24.4: Er_2O_3 micro-Raman spectrum. The black indices refer to sapphire vibrational modes and the red denoted indices refer to the phase of Er_2O_3.

Table 24.3: Assignment of Raman modes for Figure 24.4: Er_2O_3 micro-Raman spectrum

Wavenumber / cm^{-1}	Mode	Ref.
~417	A_{1g}	[256]
~430	E_g	[256]
~449	E_g	[256]
~480	F_g	[253-255]
~520	F_g	[253-255]
~569	F_g	[253-255]
~576	E_g	[256]
~605	F_g	[253-255]
~645	A_{1g}	[256]
~655	F_g	[253-255]

24.7 DFT calculations of vacancies at the CeO_2/Er_2O_3 interface

In Figure 14.6c we show the energy for oxygen vacancies at different positions in a CeO_2/Er_2O_3 heterostructure. In this calculation, charged oxygen vacancies were created by removing two electrons from the calculation, which mimics the presence of two Gd^{3+} dopants at Ce^{4+} sites. The effective composition is thus $Gd_{0.06}Ce_{0.94}O_{1.97}$.

The disorder in Er_2O_3 leads to a significant scatter in the data, but since high energy states will not be populated, we can focus on the low-energy states highlighted in red. These data points show that vacancies can reside

in lower energy states close to the interface, which is in agreement with previous calculations for charged and neutral oxygen vacancies[103].

Figure 24.5 reports the oxygen vacancy migration barrier in CeO_2 under applied biaxial strain, for migration along both the in-plane and out-of-plane direction.
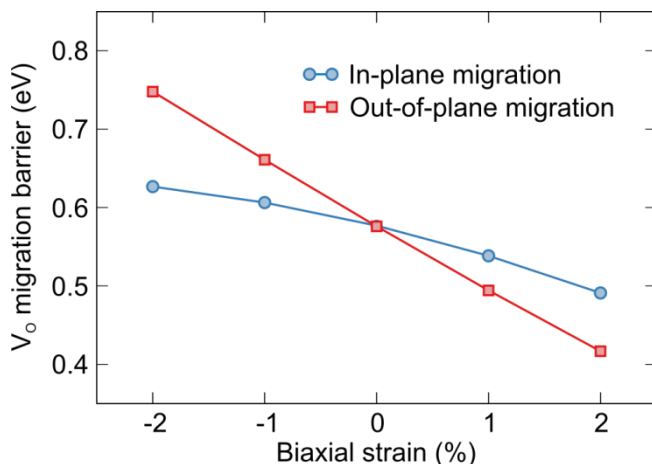

Figure 24.5: Oxygen vacancy migration barriers in CeO$_2$ under biaxial strain.

Independent of the migration direction, the migration barrier increases under compressive (negative) biaxial strain, which will reduce the mobility of oxygen vacancies under compressive strain.

Figure 14.6d shows the bottom of the conduction band of pure CeO_2 around the X (0.0, 0.0, 0.5) point of the Brillouin zone. These bands, which will be occupied by oxygen vacancy-generated electrons, show a systematically higher curvature with increasing compressive strain, which translates to a smaller effective mass and hence a higher mobility of these electrons with increasing strain.

24.8 Defect chemical equations

The equilibrium at the ceria-erbia interface can be described as follows in Kröger-Vink notation:

$$O_O^x + Ce_{Ce}^x \rightleftharpoons \frac{1}{2}O_2(g) + V_O^{\cdot\cdot} + Ce'_{Ce} + e' \qquad \textit{Equation 24.8.1}$$
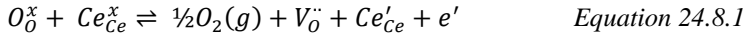
25 Supplementary Information Part IV: The role of symmetry and electroforming in strained heterostructure strained resistive switches

25.1 Analysis of the R_{off}/R_{on} ratios of preforming with different polarities

The R_{off}/R_{on} ratios of the IV curves of the two different systems, $Gd_{0.1}Ce_{0.9}O_{2-\delta}$ single thin film and $Gd_{0.1}Ce_{0.9}O_{2-\delta}/Er_2O_3$ 60 interfaces were analyzed to compare the equivalence of the mirrored IV curves, Figure 25.1. It was found that within the error the R_{off}/R_{on} ratios are the same for preforming with positive or negative polarity. We conclude that this supports the model that the preforming introduced an electric mirror plane at zero volts.
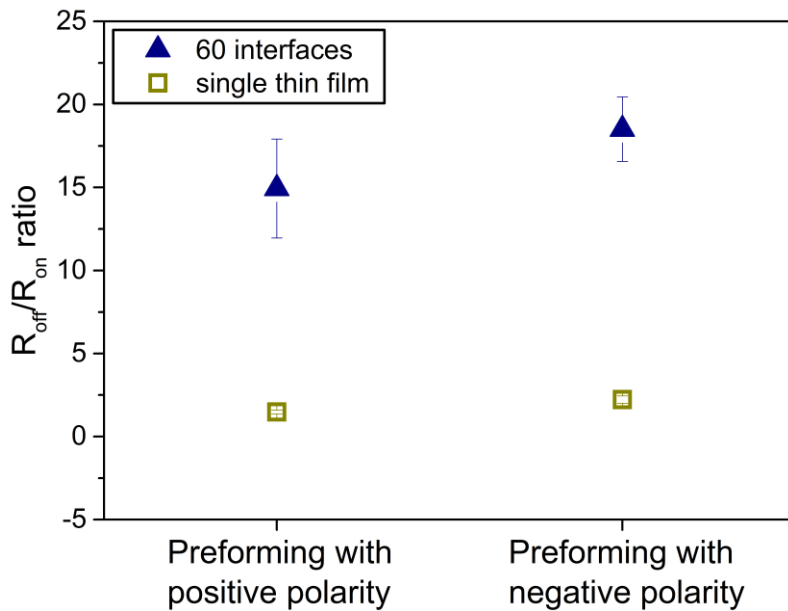
Figure 25.1: Analysis of the R_{off}/R_{on} ratios of preforming with different polarities

26   List of Figures

166

27   List of Tables

28   List of Abbreviations and Symbols

a	lattice constant
ALD	atomic layer deposition
B	bulk modulus
c.c.	compliance current
CMOS	complementary metal–oxide–semiconductor
DFT	density functional theory
DRAM	dynamic random-access memory
E	energy
ε	strain
EELS	electron energy loss spectroscopy
eV	electronvolt
f	lattice mismatch
FeRAM	Ferroelectric random-access memory
FIB	focused ion beam
FWHM	full width at half maximum
G	Gibb's energy
H	enthalpy
I	current
k_B	Boltzmann constant
MOSS	multi-beam optical stress sensor
μ_j	mobility of the charge carrier species j
ν	Poisson's ratio
p	pressure
PCM	phase change memory
PLD	pulsed laser deposition
q	elementary charge
RHEED	reflection high-energy electron diffraction
R_{off}	electric resistance in the OFF state of the device
R_{on}	electric resistance in the ON state of the device
RRAM	resistive random-access memory
RSM	reciprocal space mapping
RT	room temperature
σ	mechanical stress / conductivity

SEM	scanning electron microscopy
STM	scanning tunneling spectroscopy
STO	Strontium Titanate
STTRAM	spin-transfer torque magnetic random-access memory
t	time
T	temperature
TEM	transmission electron microscopy
V	voltage / volume
XPS	X-ray photoelectron spectroscopy
XRD	X-ray diffraction
YSZ	Yttria-stabilized zirconia

29   Bibliography

1   File, T. Computer and Internet Use in the United States. *Current Population Survery Reports, U.S. Census Bureau, Washington, DC.*, P20-568., (2013).

2   Andrae, A. S. G. & Edler, T. On Global Electricity Usage of Communication Technology: Trends to 2030. *Challenges* **6**, 117-157, (2015).

3   Jagadish, H. V. *et al.* Big Data and Its Technical Challenges. *Commun Acm* **57**, 86-94, (2014).

4   Xu, L. D., He, W. & Li, S. C. Internet of Things in Industries: A Survey. *Ieee T Ind Inform* **10**, 2233-2243, (2014).

5   Chun, S. A., Shulman, S., Sandoval, R. & Hovy, E. Government 2.0: Making Connections between Citizens, Data and Government. *Information Polity: The International Journal of Government & Democracy in the Information Age* **15**, 1-9, (2010).

6   Cisco. Cisco Visual Networking Index: Global Mobile Data Traffic Forecast Update, 2015–2020. *Cisco Public White Paper*, (2016).

7   Moore, G. E. Cramming more Components onto Integrated Circuits (Reprinted from Electronics, pg 114-117, April 19, 1965). *P Ieee* **86**, 82-85, (1998).

8   Moore, G. E. in *Electron Devices Meeting, 1975 International.* 11-13 (IEEE).

9   Markov, I. L. Limits on Fundamental Limits to Computation. *Nature* **512**, 147-154, (2014).

10   Haron, N. Z. & Hamdioui, S. in *2008 3rd International Design and Test Workshop.* 98-103 (IEEE).

11   Henkel, J., Khdr, H., Pagani, S. & Shafique, M. in *2015 52nd ACM/EDAC/IEEE Design Automation Conference (DAC).* 1-6.

12   Taylor, M. B. A Landscape of the New Dark Silicon Design Regime. *IEEE Micro* **33**, 8-19, (2013).

13   Esmaeilzadeh, H., Blem, E., Amant, R. S., Sankaralingam, K. & Burger, D. in *Computer Architecture (ISCA), 2011 38th Annual International Symposium on.* 365-376.

14   Waldrop, M. M. The Chips are down for Moore's Law. *Nature* **530**, (2016).

15   Cavin, R. K., Lugli, P. & Zhirnov, V. V. Science and Engineering Beyond Moore's Law. *P Ieee* **100**, 1720-1749, (2012).

16   Hiatt, W. R. & Hickmott, T. W. Bistable Switching in Niobium Oxide Diodes. *Appl Phys Lett* **6**, 106-&, (1965).

17   Strukov, D. B., Snider, G. S., Stewart, D. R. & Williams, R. S. The Missing Memristor found. *Nature* **453**, 80-83, (2008).

18   Yang, J. J. *et al.* Memristive Switching Mechanism for Metal/Oxide/Metal Nanodevices. *Nat Nanotechnol* **3**, 429-433, (2008).

19   Chua, L. O. Memristor - Missing Circuit Element. *Ieee Transactions on Circuit Theory* **CT18**, 507-519, (1971).

20   Waser, R. Resistive Non-volatile Memory Devices (Invited Paper). *Microelectron Eng* **86**, 1925-1928, (2009).

21   Waser, R. & Aono, M. Nanoionics-based Resistive Switching Memories. *Nat Mater* **6**, 833-840, (2007).

22   Waser, R., Dittmann, R., Staikov, G. & Szot, K. Redox-Based Resistive Switching Memories - Nanoionic Mechanisms, Prospects, and Challenges. *Adv Mater* **21**, 2632-2663, (2009).

23   Vianello, E. *et al.* Sb-doped GeS$_2$ as Performance and Reliability Booster in Conductive Bridge RAM. *2012 Ieee International Electron Devices Meeting (Iedm)*, (2012).

24   Haemori, M., Nagata, T. & Chikyow, T. Impact of Cu Electrode on Switching Behavior in a Cu/HfO$_2$/Pt Structure and Resultant Cu Ion Diffusion. *Appl Phys Express* **2**, (2009).

25   Mohammad, B. *et al.* State of the Art of Metal Oxide Memristor Devices. *Nanotechnol Rev* **5**, 311-329, (2016).

26   Ielmini, D. Resistive Switching Memories based on Metal Oxides: Mechanisms, Reliability and Scaling. *Semicond Sci Tech* **31**, (2016).

27   Van Zant, P. *Microchip Fabrication : a Practical Guide to Semiconductor Processing*. Sixth edition. edn,   (McGraw-Hill Professional, 2014).

28   Sacchetto, D., De Micheli, G. & Leblebici, Y. Multiterminal Memristive Nanowire Devices for Logic and Memory Applications: A Review. *P Ieee* **100**, 2008-2020, (2012).

29   Yu, S. & Chen, P. Y. Emerging Memory Technologies: Recent Trends and Prospects. *IEEE Solid-State Circuits Magazine* **8**, 43-56, (2016).

30   Jo, S. H. *et al.* Nanoscale Memristor Device as Synapse in Neuromorphic Systems. *Nano Lett* **10**, 1297-1301, (2010).

31   Strukov, D. B. & Kohlstedt, H. Resistive switching phenomena in thin films: Materials, devices, and applications. *Mrs Bull* **37**, 108-117, (2012).

32   Chanthbouala, A. *et al.* Solid-state memories based on ferroelectric tunnel junctions. *Nat Nanotechnol* **7**, 101-104, (2012).

33   Sun, J. Z. Spin-transfer torque switched magnetic tunnel junctions in magnetic random access memory. **9931**, 993113, (2016).

34   Wong, H.-S. P. *et al.* Stanford Memory Trends. *https://nano.stanford.edu/stanford-memory-trends/*, (accessed July 20, 2016.).

35   Privitera, S. *et al.* Microscopy Study of the Conductive Filament in HfO$_2$ Resistive Switching Memory Devices. *Microelectron Eng* **109**, 75-78, (2013).

36   Watanabe, Y. *et al.* Current-driven Insulator-Conductor Transition and Nonvolatile Memory in Chromium-doped SrTiO$_3$ Single Crystals. *Appl Phys Lett* **78**, 3738-3740, (2001).

37   Guo, T. T., Tan, T. T. & Liu, Z. T. Resistive Switching Behavior of HfO$_2$ Film with different Ti doping Concentrations. *J Phys D Appl Phys* **49**, (2016).

38   Kim, J. *et al.* Effect of W Impurity on Resistance Switching Characteristics of NiO$_x$ Films. *Curr Appl Phys* **11**, E70-E74, (2011).

39   Yang, J. J., Strukov, D. B. & Stewart, D. R. Memristive Devices for Computing. *Nat Nanotechnol* **8**, 13-24, (2013).

40   Kryder, M. H. & Kim, C. S. After Hard Drives - What Comes Next? *Ieee T Magn* **45**, 3406-3413, (2009).

41   Meena, J. S., Sze, S. M., Chand, U. & Tseng, T. Y. Overview of Emerging Nonvolatile Memory Technologies. *Nanoscale Res Lett* **9**, 526, (2014).

42   Wang, Y. *et al.* Investigation of resistive switching in Cu-doped HfO2 thin film for multilevel non-volatile memory applications. *Nanotechnology* **21**, (2010).

43   Reyren, N. *et al.* Superconducting Interfaces between Insulating Oxides. *Science* **317**, 1196-1199, (2007).

44   Bhattacharya, A. & May, S. J. in *Annual Review of Materials Research, Vol 44* Vol. 44 *Annual Review of Materials Research* (ed D. R. Clarke) 65-90 (2014).

45   Smith, A. M., Mohs, A. M. & Nie, S. Tuning the Optical and Electronic Properties of Colloidal Nanocrystals by Lattice Strain. *Nat Nanotechnol* **4**, 56-63, (2009).

46   Yildiz, B. "Stretching" the Energy Landscape of Oxides - Effects on Electrocatalysis and Diffusion. *Mrs Bull* **39**, 147-156, (2014).

47   Malavasi, L., Fisher, C. A. & Islam, M. S. Oxide-ion and Proton Conducting Electrolyte Materials for Clean Energy Applications: Structural and Mechanistic Features. *Chem Soc Rev* **39**, 4370-4387, (2010).

48   Packan, P. *et al.* High Performance Hi-K plus Metal Gate Strain Enhanced Transistors on (110) Silicon. *Ieee International Electron Devices Meeting 2008, Technical Digest*, 63-66, (2008).

49   Heyns, M. *et al.* Advancing CMOS beyond the Si Roadmap with Ge and III/V Devices. *2011 Ieee International Electron Devices Meeting (Iedm)*, (2011).

50   Schichtel, N., Korte, C., Hesse, D. & Janek, J. Elastic Strain at Interfaces and its Influence on Ionic Conductivity in Nanoscaled Solid Electrolyte Thin Films - Theoretical Considerations and Experimental Studies. *Phys Chem Chem Phys* **11**, 3043-3048, (2009).

51   Korte, C., Peters, A., Janek, J., Hesse, D. & Zakharov, N. Ionic Conductivity and Activation Energy for Oxygen Ion Transport in Superlattices - the Semicoherent Multilayer System YSZ (ZrO_2 + 9.5 mol% Y_2O_3)/Y_2O_3. *Phys Chem Chem Phys* **10**, 4623-4635, (2008).

52   Shen, W. D., Jiang, J. & Hertz, J. L. Beneficial Lattice Strain in Heterogeneously Doped Ceria. *J Phys Chem C* **118**, 22904-22912, (2014).

53   Shen, W. D. & Hertz, J. L. Ionic Conductivity of YSZ/CZO Multilayers with variable Lattice Mismatch. *J Mater Chem A* **3**, 2378-2386, (2015).

54   Kushima, A. & Yildiz, B. Oxygen Ion Diffusivity in Strained Yttria Stabilized Zirconia: Where is the Fastest Strain? *J Mater Chem* **20**, 4809, (2010).

55   De Souza, R. A., Ramadan, A. & Hörner, S. Modifying the Barriers for Oxygen-Vacancy Migration in Fluorite-structured CeO$_2$ Electrolytes through Strain: a Computer Simulation Study. *Energy Environ. Sci.* **5**, 5445-5453, (2012).

56   Hinterberg, J., Zacherle, T. & De Souza, R. A. Activation Volume Tensor for Oxygen-Vacancy Migration in Strained CeO$_2$ Electrolytes. *Phys Rev Lett* **110**, (2013).

57   Korte, C. *et al.* Coherency Strain and its Effect on Ionic Conductivity and Diffusion in Solid Electrolytes - an Improved Model for Nanocrystalline Thin Films and a Review of Experimental Data. *Phys Chem Chem Phys* **16**, 24575-24591, (2014).

58   Wen, K. C., Lv, W. Q. & He, W. D. Interfacial Lattice-strain Effects on Improving the Overall Performance of Micro-solid Oxide Fuel Cells. *J Mater Chem A* **3**, 20031-20050, (2015).

59   Pryds, N. & Esposito, V. When Two Become One: An Insight into 2D Conductive Oxide Interfaces. *J Electroceram*, 1-23, (2016).

60   Evans, A., Bieberle-Hutter, A., Rupp, J. L. M. & Gauckler, L. J. Review on Microfabricated Micro-Solid Oxide Fuel Cell Membranes. *J Power Sources* **194**, 119-129, (2009).

61   Park, C. O., Fergus, J. W., Miura, N., Park, J. & Choi, A. Solid-state Electrochemical Gas Sensors. *Ionics* **15**, 261-284, (2009).

62   Yao, L. *et al.* Fabrication of High Performance Oxygen Sensors using Multilayer Oxides with High Interfacial Conductivity. *J Mater Chem A* **4**, 11422-11429, (2016).

63   van den Broek, J., Afyon, S. & Rupp, J. L. M. Interface-Engineered All-Solid-State Li-Ion Batteries Based on Garnet-Type Fast Li$^+$ Conductors. *Adv Energy Mater*, (2016).

64   Sata, N., Eberman, K., Eberl, K. & Maier, J. Mesoscopic Fast Ion Conduction in Nanometre-scale Planar Heterostructures. *Nature* **408**, 946-949, (2000).

65   Azad, S. *et al.* Nanoscale Effects on Ion Conductance of Layer-by-Layer Structures of Gadolinia-doped Ceria and Zirconia. *Appl Phys Lett* **86**, (2005).

66   Garcia-Barriocanal, J. *et al.* Colossal Ionic Conductivity at Interfaces of Epitaxial ZrO_2:Y_2O_3/$SrTiO_3$ Heterostructures. *Science* **321**, 676-680, (2008).

67   Guo, X. Comment on "Colossal Ionic Conductivity at Interfaces of Epitaxial $ZrO2$:Y_2O_3/$SrTiO_3$ Heterostructures". *Science* **324**, (2009).

68   Cavallaro, A. *et al.* Electronic Nature of the Enhanced Conductivity in YSZ-STO Multilayers Deposited by PLD. *Solid State Ionics* **181**, 592-601, (2010).

69   Li, F. *et al.* The Strain Effect on Colossal Oxygen Ionic Conductivity in Nanoscale Zirconia Electrolytes: a First-Principles-based Study. *Phys Chem Chem Phys* **15**, 2692-2697, (2013).

70   Tarancon, A. & Morata, A. New Insights into the Origin of the Oxide Ionic Diffusion Change in Strained Lattices of Yttria stabilized Zirconia. *Comp Mater Sci* **103**, 206-215, (2015).

71   Pergolesi, D. *et al.* Tensile Lattice Distortion does not Affect Oxygen Transport in Yttria-stabilized Zirconia-CeO$_2$ Heterointerfaces. *Acs Nano* **6**, 10524-10534, (2012).

72   Fluri, A., Pergolesi, D., Roddatis, V., Wokaun, A. & Lippert, T. In-situ Stress Observation in Oxide Thin Films and how Tensile Strain Influences Oxygen Ion Conduction. *Nat Commun* **7**, (2016).

73   Schichtel, N. *et al.* On the Influence of Strain on Ion Transport: Microstructure and Ionic Conductivity of Nanoscale YSZ|Sc$_2$O$_3$ Multilayers. *Phys Chem Chem Phys* **12**, 14596-14608, (2010).

74   Aydin, H., Korte, C., Rohnke, M. & Janek, J. Oxygen Tracer Diffusion along Interfaces of Strained Y$_2$O$_3$/YSZ Multilayers. *Phys Chem Chem Phys* **15**, 1944-1955, (2013).

75   Korte, C., Schichtel, N., Hesse, D. & Janek, J. Influence of Interface Structure on Mass Transport in Phase Boundaries between Different Ionic Materials: Experimental Studies and Formal Considerations. *Monatsh Chem* **140**, 1069-1080, (2009).

76   Sanna, S. *et al.* Enhancement of Ionic Conductivity in Sm-doped Ceria/Yttria-stabilized Zirconia Heteroepitaxial Structures. *Small* **6**, 1863-1867, (2010).

77   Karthikeyan, A. & Ramanathan, S. Temperature-dependent Interfacial Carrier Transport in Low-dimensional Oxides using Ionic Conductor-Insulator (YDZ-SiO$_2$) Superlattices. *J Appl Phys* **104**, (2008).

78   Li, B. *et al.* Multilayered YSZ/GZO Films with Greatly Enhanced Ionic Conduction for Low Temperature Solid Oxide Fuel Cells. *Phys Chem Chem Phys* **15**, 1296-1301, (2013).

79   Peters, A., Korte, C., Hesse, D., Zakharov, N. & Janek, J. Ionic Conductivity and Activation Energy for Oxygen Ion Transport in Superlattices - The Multilayer System CSZ (ZrO$_2$+CaO)/Al$_2$O$_3$. *Solid State Ionics* **178**, 67-76, (2007).

80   Tschope, A., Bauerle, C. & Birringer, R. Numerical analysis of space charge layers and electrical conductivity in mesoscopic cerium oxide crystals. *J Appl Phys* **95**, 1203-1210, (2004).

81   Sillassen, M. *et al.* Low-Temperature Superionic Conductivity in Strained Yttria-Stabilized Zirconia. *Adv Funct Mater* **20**, 2071-2076, (2010).

82   Mohan Kant, K., Esposito, V. & Pryds, N. Strain Induced Ionic Conductivity Enhancement in Epitaxial $Ce_{0.9}Gd_{0.1}O_{2-\delta}$ Thin Films. *Appl Phys Lett* **100**, 033105, (2012).

83   Jiang, J., Hu, X. C., Shen, W. D., Ni, C. Y. & Hertz, J. L. Improved Ionic Conductivity in Strained Yttria-stabilized Zirconia Thin Films. *Appl Phys Lett* **102**, 143901, (2013).

84   Kosacki, I., Rouleau, C. M., Becher, P. F., Bentley, J. & Lowndes, D. H. Surface Interface-related Conductivity in Nanometer Thick YSZ Films. *Electrochem Solid St* **7**, A459-A461, (2004).

85   Kosacki, I., Rouleau, C. M., Becher, P. F., Bentley, J. & Lowndes, D. H. Nanoscale Effects on the Ionic Conductivity in Highly Textured YSZ Thin Films. *Solid State Ionics* **176**, 1319-1326, (2005).

86   Jiang, J., Hu, X. C., Shen, W. D., Ni, C. Y. & Hertz, J. L. Improved ionic conductivity in strained yttria-stabilized zirconia thin films. *Appl Phys Lett* **102**, (2013).

87   Sata, N., Jin-Phillipp, N. Y., Eberl, K. & Maier, J. Enhanced Ionic Conductivity and Mesoscopic Size Effects in Heterostructures of BaF_2 and CaF_2. *Solid State Ionics* **154–155**, 497-502, (2002).

88   Jin-Phillipp, N. Y. *et al.* Structures of BaF_2–CaF_2 Heterolayers and their Influences on Ionic Conductivity. *The Journal of Chemical Physics* **120**, 2375-2381, (2004).

89   Guo, X. X. & Maier, J. Comprehensive Modeling of Ion Conduction of Nanosized CaF_2/BaF_2 Multilayer Heterostructures. *Adv Funct Mater* **19**, 96-101, (2009).

90   Swaddle, T. W. *Inorganic Chemistry : an Industrial and Environmental Perspective*. (Academic Press, 1997).

91   Guo, X. & Waser, R. Electrical Properties of the Grain Boundaries of Oxygen Ion Conductors: Acceptor-doped Zirconia and Ceria. *Prog Mater Sci* **51**, 151-210, (2006).

92   Gerhardt, R., Nowick, A. S., Mochel, M. E. & Dumler, I. Grain-Boundary Effect in Ceria Doped with Trivalent Cations. 2. Microstructure and Microanalysis. *J Am Ceram Soc* **69**, 647-651, (1986).

93   Ayache, J. *Sample Preparation Handbook for Transmission Electron Microscopy : Methodology*. (Springer, 2010).

94   Lee, W. E. & Rainforth, W. M. *Ceramic microstructures : property control by processing*. (London [etc.] : Chapman & Hall, 1994).

95   Aydin, H., Korte, C. & Janek, J. O-18-Tracer Diffusion along Nanoscaled Sc_2O_3/Yttria Stabilized Zirconia (YSZ) Multilayers: on the Influence of Strain. *Sci Technol Adv Mat* **14**, (2013).

96   Suess, M. J. *et al.* Analysis of Enhanced Light Emission from Highly Strained Germanium Microbridges. *Nat Photonics* **7**, 466-472, (2013).

97   Cho, S. Y. *et al.* Oxygen Transport in Epitaxial $La_{0.875}Sr_{0.125}CoO_{3-d}$ Thin-Film Cathodes for Solid Oxide Fuel Cells: Roles of Anisotropic Strain. *Scripta Mater* **115**, 141-144, (2016).

98   Shi, Y. *et al.* Growth of Highly Strained CeO_2 Ultrathin Films. *Acs Nano*, (2016).

180

99   Kubicek, M. *et al.* Tensile Lattice Strain Accelerates Oxygen Surface Exchange and Diffusion in La$_{1-x}$Sr$_x$CoO$_{3-d}$ Thin Films. *Acs Nano* **7**, 3276-3286, (2013).

100   Infortuna, A., Harvey, A. S. & Gauckler, L. J. Microstructures of CGO and YSZ Thin Films by Pulsed Laser Deposition. *Adv Funct Mater* **18**, 127-135, (2008).

101   Wagner, C. The Electrical Conductivity of Semi-Conductors involving Inclusions of another Phase. *J Phys Chem Solids* **33**, 1051-1059, (1972).

102   Ma, D. W. *et al.* Effect of Lattice Strain on the Oxygen Vacancy Formation and Hydrogen Adsorption at CeO$_2$(111) Surface. *Phys Lett A* **378**, 2570-2575, (2014).

103   Aidhy, D. S., Liu, B., Zhang, Y. W. & Weber, W. J. Strain-Induced Phase and Oxygen-Vacancy Stability in Ionic Interfaces from First-Principles Calculations. *J Phys Chem C* **118**, 30139-30144, (2014).

104   Ahn, K. *et al.* Lattice-Strain Effect on Oxygen Vacancy Formation in Gadolinium-doped Ceria. *J Electroceram* **32**, 72-77, (2014).

105   Marrocchelli, D., Sun, L. & Yildiz, B. Dislocations in SrTiO$_3$: Easy to Reduce but not so Fast for Oxygen Transport. *J Am Chem Soc* **137**, 4735-4748, (2015).

106   Tsvetkov, N., Lu, Q., Chen, Y. & Yildiz, B. Accelerated Oxygen Exchange Kinetics on Nd$_2$NiO$_{4+d}$ Thin Films with Tensile Strain along c-Axis. *Acs Nano* **9**, 1613-1621, (2015).

107   Jalili, H., Han, J. W., Kuru, Y., Cai, Z. H. & Yildiz, B. New Insights into the Strain Coupling to Surface Chemistry, Electronic Structure, and Reactivity of La0.7Sr0.3MnO3. *J Phys Chem Lett* **2**, 801-807, (2011).

108   Maree, P. M. J. *et al.* Generation of Misfit Dislocations in Semiconductors. *J Appl Phys* **62**, 4413-4420, (1987).

109   Sun, L., Marrocchelli, D. & Yildiz, B. Edge Dislocation slows down Oxide Ion Diffusion in doped CeO_2 by Segregation of Charged Defects. *Nat Commun* **6**, 6294, (2015).

110   Metlenko, V. *et al.* Do Dislocations Act as Atomic Autobahns for Oxygen in the Perovskite Oxide $SrTiO_3$? *Nanoscale* **6**, 12864-12876, (2014).

111   Yezhou Shi, S. L., Matteo Monti, Colvin Wang, Zhuoluo A. Feng, William D. Nix, Michael F. Toney, Robert Sinclair, William C. Chueh. Growth of Highly Strained CeO2 Ultrathin Films. *Acs Nano*, (2016).

112   Sheth, J. *et al.* Coupling of Strain, Stress, and Oxygen Non-stoichiometry in Thin Film $Pr_{0.1}Ce_{0.9}O_{2-\delta}$. *Nanoscale*, 16499-16510, (2016).

113   Shen, W. D., Jiang, J. & Hertz, J. L. Reduced ionic conductivity in biaxially compressed ceria. *Rsc Adv* **4**, 21625-21630, (2014).

114   Kreisel, J. *et al.* Probing Individual Layers in Functional Oxide Multilayers by Wavelength-Dependent Raman Scattering. *Adv Funct Mater* **22**, 5044-5049, (2012).

115   DeWolf, I. Micro-Raman Spectroscopy to Study Local Mechanical Stress in Silicon Integrated Circuits. *Semicond Sci Tech* **11**, 139-154, (1996).

116   Freund, L. B. & Suresh, S. *Thin film materials : stress, defect formation, and surface evolution*. 1st pbk. edn, (Cambridge University Press, 2009).

117   Perednis, D. & Gauckler, L. J. Thin film deposition using spray pyrolysis. *J Electroceram* **14**, 103-111, (2005).

118   Rupp, J. L. M., Scherrer, B., Schauble, N. & Gauckler, L. J. Time-Temperature-Transformation (TTT) Diagrams for Crystallization of Metal Oxide Thin Films. *Adv Funct Mater* **20**, 2807-2814, (2010).

119   Willmott, P. R. & Huber, J. R. Pulsed Laser Vaporization and Deposition. *Reviews of Modern Physics* **72**, 315-328, (2000).

120   Mogensen, M., Sammes, N. M. & Tompsett, G. A. Physical, Chemical and Electrochemical Properties of Pure and doped Ceria. *Solid State Ionics* **129**, 63-94, (2000).

121   Kroger, F. A. & Vink, H. J. Relations between the Concentrations of Imperfections in Crystalline Solids. *Solid State Phys* **3**, 307-435, (1956).

122   Eguchi, K., Setoguchi, T., Inoue, T. & Arai, H. Electrical-Properties of Ceria-Based Oxides and Their Application to Solid Oxide Fuel-Cells. *Solid State Ionics* **52**, 165-172, (1992).

123   Mogensen, M., Lindegaard, T., Hansen, U. R. & Mogensen, G. Physical-Properties of Mixed Conductor Solid Oxide Fuel-Cell Anodes of Doped Ceo$_2$. *J Electrochem Soc* **141**, 2122-2128, (1994).

124   Eyring, L. in *Handbook on the Physics and Chemistry of Rare Earths* Vol. Volume 3   337-399 (Elsevier, 1979).

125   Ruiz-Trejo, E. The Optical Band Gap of Gd-doped CeO$_2$ Thin Films as Function of Temperature and Composition. *J Phys Chem Solids* **74**, 605-610, (2013).

126   Prokofiev, A. V., Shelykh, A. I. & Melekh, B. T. Periodicity in the Band Gap Variation of Ln$_2$X$_3$ (X = O, S, Se) in the Lanthanide Series. *J Alloy Compd* **242**, 41-44, (1996).

127   Karlsruhe, F. *Inorganic Crystal Structure Database – ICSD* accessed 3rd October 2016).

128   Adachi, G., Imanaka, N. & Kang, Z. C. *Binary Rare Earth Oxides*. (Kluwer Academic Publishers, 2004).

129   Song, K. P. *et al.* Cerium Reduction at the Interface between Ceria and Yttria-stabilised Zirconia and Implications for Interfacial Oxygen Non-Stoichiometry. *Apl Mater* **2**, (2014).

130   Ruiz-Trejo, E. & Maier, J. Electronic Transport in Single Crystals of Gd-doped Ceria. *J Electrochem Soc* **154**, B583-B587, (2007).

131   Ruiz-Trejo, E., Tavizon, G. & Garcia-Ortega, H. Structure and Electronic Conductivity of Reduced Gd-doped CeO_2. *J Electrochem Soc* **154**, A70-A74, (2007).

132   Yao, L., Nishijima, H. & Pan, W. Contrary Interfacial Effects for Textured and Non-textured Multilayer Solid Oxide Electrolytes. *Rsc Adv* **6**, 34390-34398, (2016).

133   Lee, K. R., Ahn, K., Chung, Y. C., Lee, J. H. & Yoo, H. I. Lattice Distortion Effect on Electrical Properties of GDC Thin Films: Experimental Evidence and Computational Simulation. *Solid State Ionics* **229**, 45-53, (2012).

134   Dezanneau, G., Hermet, J. & Dupe, B. Effects of Biaxial Strain on Bulk 8% Yttria-stabilised Zirconia Ion Conduction through Molecular Dynamics. *Int J Hydrogen Energ* **37**, 8081-8086, (2012).

135   Hirschfeld, J. A. & Lustfeld, H. First-principles Study and Modeling of Strain-dependent Ionic Migration in ZrO_2. *Phys Rev B* **84**, (2011).

136   Kilner, J. A. Ionic Conductors: Feel the Strain. *Nat Mater* **7**, 838-839, (2008).

137   De Souza, R. A. & Ramadan, A. H. Ionic Conduction in the $SrTiO_3|YSZ|SrTiO_3$ Heterostructure. *Phys Chem Chem Phys* **15**, 4505-4509, (2013).

138   Rupp, J. L. M. Ionic Diffusion as a Matter of Lattice-strain for Electroceramic Thin Films. *Solid State Ionics* **207**, 1-13, (2012).

139   Rupp, J. L. M. *et al.* Scalable Oxygen- Ion Transport Kinetics in Metal- Oxide Films: Impact of Thermally Induced Lattice Compaction in Acceptor Doped Ceria Films. *Adv Funct Mater* **24**, 1562-1574, (2014).

140   Omar, S., Wachsman, E. & Nino, J. Higher Conductivity Sm^{3+} and Nd^{3+} Co-doped Ceria-based Electrolyte Materials. *Solid State Ionics* **178**, 1890-1897, (2008).

141   Rupp, J. L. M., Schweiger, S. & Messerschmitt, F. Strained Multilayer Resistive-Switching Memory Elements (WO/2014/170023). (2014).

142   Santiso, J. & Burriel, M. Deposition and Characterisation of Epitaxial Oxide Thin Films for SOFCs. *J Solid State Electr* **15**, 985-1006, (2011).

143   Chen, L. *et al.* Electrical Properties of a Highly Oriented, Textured Thin Film of the Ionic Conductor $Gd:CeO_{2-d}$ on (001) MgO. *Appl Phys Lett* **83**, 4737-4739, (2003).

144   Chen, L. *et al.* High Ttemperature Electrical Conductivity of Epitaxial Gd-doped CeO_2 Thin Films. *Solid State Ionics* **175**, 103-106, (2004).

145   Hytch, M. J., Snoeck, E. & Kilaas, R. Quantitative Measurement of Displacement and Strain Fields from HREM Micrographs. *Ultramicroscopy* **74**, 131-146, (1998).

146   Hong, W. T. *et al.* Tuning the Spin State in $LaCoO_3$ Thin Films for Enhanced High-Temperature Oxygen Electrocatalysis. *J Phys Chem Lett* **4**, 2493-2499, (2013).

147   Irmer, G. *et al.* Anisotropic Strain on Phonons in a-Plane GaN Layers studied by Raman Scattering. *J Mater Sci-Mater El* **19**, S51-S57, (2008).

148   Huang, M. *et al.* Phonon Softening and Crystallographic Orientation of Strained Graphene studied by Raman Spectroscopy. *Proc Natl Acad Sci U S A* **106**, 7304-7308, (2009).

149   Evans, A. *et al.* Micro-Solid Oxide Fuel Cells: Status, Challenges, and Chances. *Monatsh Chem* **140**, 975-983, (2009).

150   Strukov, D. B., Borghetti, J. L. & Williams, R. S. Coupled Ionic and Electronic Transport Model of Thin-film Semiconductor Memristive Behavior. *Small* **5**, 1058-1063, (2009).

151   International Technoloy Roadmap for Semiconductor Industry (ITRS) 2011 Edition, Emerging research devices http://www.itrs.net/ (2011).

152   Linn, E., Rosezin, R., Tappertzhofen, S., Bottger, U. & Waser, R. Beyond von Neumann - Logic Operations in Passive Crossbar Arrays alongside Memory Operations. *Nanotechnology* **23**, 305205, (2012).

153   Rosezin, R. *et al.* Integrated Complementary Resistive Switches for Passive High-Density Nanocrossbar Arrays. *Ieee Electr Device L* **32**, 191-193, (2011).

154   Dou, C. *et al.* Resistive Switching Behavior of a CeO_2 Based ReRAM Cell Incorporated with Si Buffer Layer. *Microelectron Reliab* **52**, 688-691, (2012).

155   Liao, Z. L. & Chen, D. M. A Metal Oxide Heterostructure for Resistive Random Access Memory Devices. *Chinese Phys Lett* **30**, (2013).

156   Liao, Z. L. *et al.* Electrode Engineering for Improving Resistive Switching Performance in Single Crystalline CeO_2 Thin Films. *Solid State Electron* **72**, 4-7, (2012).

157   Lin, C. Y., Lee, D. Y., Wang, S. Y., Lin, C. C. & Tseng, T. Y. Reproducible Resistive Switching Behavior in Sputtered CeO_2 Polycrystalline Films. *Surf Coat Tech* **203**, 480-483, (2008).

158   Zhu, Y. D. *et al.* Improved Bipolar Resistive Switching Properties in CeO_2/ZnO Stacked Heterostructures. *Semicond Sci Tech* **28**, (2013).

186

159   Sun, X. *et al.* Resistive Switching in CeO$_x$ Films for Nonvolatile Memory Application. *Ieee Electr Device L* **30**, 334-336, (2009).

160   Karageorgakis, N. I. *et al.* Properties of Flame Sprayed Ce$_{0.8}$Gd$_{0.2}$O$_{1.9-d}$ Electrolyte Thin Films. *Adv Funct Mater* **21**, 532-539, (2011).

161   Brauer, G. & Gradinger, H. Uber Heterotype Mischphasen Bei Seltenerdoxyden .2. Die Oxydsysteme Des Cers Und Des Praseodyms. *Z Anorg Allg Chem* **277**, 89-95, (1954).

162   Saiki, A., Ishizawa, N., Mizutani, N. & Kato, M. Structural Change of C-Rare Earth Sesquioxides Yb$_2$O$_3$ and Er$_2$O$_3$ as a Function of Temperature. *Journal of the Ceramic Assoc. of Japan* **93**, 649-654, (1985).

163   Le Marrec, F. *et al.* Ferroelectric PbTiO$_3$/BaTiO$_3$ Superlattices: Growth Anomalies and Confined Modes. *Phys Rev B* **61**, R6447-R6450, (2000).

164   Schuller, I. K. New Class of Layered Materials. *Phys Rev Lett* **44**, 1597-1600, (1980).

165   Dargis, R. *et al.* Structural and Thermal Properties of Single Crystalline Epitaxial Gd$_2$O$_3$ and Er$_2$O$_3$ Grown on Si(111). *Ecs J Solid State Sc* **1**, N24-N28, (2012).

166   Hong, S. J. & Virkar, A. V. Lattice-Parameters and Densities of Rare-Earth-Oxide Doped Ceria Electrolytes. *J Am Ceram Soc* **78**, 433-439, (1995).

167   Jang, H. W. *et al.* Domain Engineering for Enhanced Ferroelectric Properties of Epitaxial (001) BiFeO Thin Films. *Adv Mater* **21**, 817-+, (2009).

168   Gruber, J. B., Chirico, R. D. & Westrum, E. F. Correlation of Spectral and Heat-Capacity Schottky Contributions for Dy$_2$O$_3$, Er$_2$O$_3$, and Yb$_2$O$_3$. *J Chem Phys* **76**, 4600-4605, (1982).

169   Lejus, A. M. & Michel, D. Raman-Spectrum of Er_2O_3 Sesquioxide. *Physica Status Solidi B-Basic Research* **84**, K105-K108, (1977).

170   Kossoy, A. *et al.* Influence of Point-Defect Reaction Kinetics on the Lattice Parameter of $Ce_{0.8}Gd_{0.2}O_{1.9}$. *Adv Funct Mater* **19**, 634-641, (2009).

171   Muthukkumaran, K. *et al.* Microstructural Studies of Bulk and Thin Film GDC. *Ionics* **14**, 165-171, (2008).

172   Korobko, R. *et al.* Influence of Gd Content on the Room Temperature Mechanical Properties of Gd-doped Ceria. *Scripta Mater* **66**, 155-158, (2012).

173   Pikalova, E. Y. *et al.* CeO_2 based Materials doped with Lanthanides for Applications in Intermediate Temperature Electrochemical Devices. *Int J Hydrogen Energ* **36**, 6175-6183, (2011).

174   White, W. B. & Keramidas, V. G. Vibrational-Spectra of Oxides with C-Type Rare-Earth Oxide Structure. *Spectrochim Acta a-M* **A 28**, 501-509, (1972).

175   Mermoux, M. *et al.* Strain in Epitaxial Si/SiGe Graded Buffer Structures Grown on Si(100), Si(110), and Si(111) Optically Evaluated by Polarized Raman Spectroscopy and Imaging. *J Appl Phys* **107**, (2010).

176   Kourouklis, G. A., Jayaraman, A. & Espinosa, G. P. High-Pressure Raman Study of CeO_2 to 35 GPa and Pressure-induced Phase Transformation from the Fluorite Structure. *Phys Rev B Condens Matter* **37**, 4250-4253, (1988).

177   Fan, X. F., Case, E. D., Yang, Q. & Nicholas, J. D. Room Temperature Elastic Properties of Gadolinia-doped Ceria as a Function of Porosity. *Ceram Int* **39**, 6877-6886, (2013).

178   Swaminathan, N. & Qu, J. Evaluation of Thermomechanical Properties of Non-Stoichiometric Gadolinium doped Ceria using Atomistic Simulations. *Model Simul Mater Sc* **17**, (2009).

179   Kossoy, A., Feldman, Y., Wachtel, E., Lubomirsky, I. & Maier, J. Elasticity of Solids with a Large Concentration of Point Defects II. The Chemical Strain Effect in $Ce_{0.8}Gd_{0.2}O_{1.9}$. *Adv Funct Mater* **17**, 2393-2398, (2007).

180   Hohnke, D. K. Ionic-Conduction in Doped Oxides with the Fluorite Structure. *Solid State Ionics* **5**, 531-534, (1981).

181   Zhu, Y. Y. *et al.* Band Offsets of Er_2O_3 Films Epitaxially grown on Si Substrates. *Appl Phys Lett* **88**, (2006).

182   Rupp, J. L. M., Infortuna, A. & Gauckler, L. J. Thermodynamic Stability of Gadolinia-doped Ceria Thin Film Electrolytes for Micro-solid Oxide Fuel Cells. *J Am Ceram Soc* **90**, 1792-1797, (2007).

183   Minervini, L., Zacate, M. O. & Grimes, R. W. Defect Cluster Formation in M_2O_3-doped CeO_2. *Solid State Ionics* **116**, 339-349, (1999).

184   Andersson, D. A., Simak, S. I., Skorodumova, N. V., Abrikosov, I. A. & Johansson, B. Optimization of Ionic Conductivity in doped Ceria. *Proc Natl Acad Sci U S A* **103**, 3518-3521, (2006).

185   Hull, S. *et al.* Oxygen Vacancy Ordering within Anion-deficient Ceria. *J Solid State Chem* **182**, 2815-2821, (2009).

186   Pietrucci, F., Bernasconi, M., Laio, A. & Parrinello, M. Vacancy-Vacancy Interaction and Oxygen Diffusion in Stabilized Cubic ZrO_2 from First Principles. *Phys Rev B* **78**, (2008).

187   Burbano, M. *et al.* Oxygen Vacancy Ordering and the Conductivity Maximum in Y_2O_3-Doped CeO_2. *Chem Mater* **24**, 222-229, (2012).

188   Wang, B. & Cormack, A. N. Strain Modulation of Defect Structure in Gadolinia-Doped Ceria. *J Phys Chem C* **117**, 146-151, (2013).

189   Perkins, J. M. *et al.* Anomalous Oxidation States in Multilayers for Fuel Cell Applications. *Adv Funct Mater* **20**, 2664-2674, (2010).

190   Gao, Z., Mogni, L. V., Miller, E. C., Railsback, J. G. & Barnett, S. A. A Perspective on Low-Temperature Solid Oxide Fuel Cells. *Energ Environ Sci* **9**, 1602-1644, (2016).

191   Baure, G., Kasse, R. M., Rudawski, N. G. & Nino, J. C. Across Plane Ionic Conductivity of Highly Oriented Neodymium doped Ceria Thin Films. *Phys Chem Chem Phys* **17**, 12259-12264, (2015).

192   Sanna, S. *et al.* Enhancement of the Chemical Stability in Confined delta-Bi_2O_3. *Nat Mater* **14**, 500-504, (2015).

193   Yao, L., Liu, W., Ou, G., Nishijima, H. & Pan, W. Enhanced Ionic Conductivity in Magnetron-sputtered $Ce_{0.8}Sm_{0.2}O_{2-d}/Al_2O_3$ Multilayers. *Electrochim Acta* **158**, 196-201, (2015).

194   Mayeshiba, T. & Morgan, D. Strain Effects on Oxygen Migration in Perovskites. *Phys Chem Chem Phys* **17**, 2715-2721, (2015).

195   Lazovski, G., Kraynis, O., Korobko, R., Wachtel, E. & Lubomirsky, I. Optical investigation of oxygen diffusion in thin films of Gd-doped ceria. *Solid State Ionics* **277**, 30-37, (2015).

196   Pergolesi, D. *et al.* Probing the Bulk Ionic Conductivity by Thin Film Hetero-epitaxial Engineering. *Sci Technol Adv Mat* **16**, (2015).

197   Ackermann, S. *et al.* Kinetics of CO_2 Reduction over Nonstoichiometric Ceria. *J Phys Chem C Nanomater Interfaces* **119**, 16452-16461, (2015).

198   Shi, Y., Bork, A. H., Schweiger, S. & Rupp, J. L. M. The Effect of Mechanical Twisting on Oxygen Ionic Transport in Solid-state Energy Conversion Membranes. *Nat Mater* **14**, 721-727, (2015).

199   Tong, X., Thangadurai, V. & Wachsman, E. D. Highly Conductive Li Garnets by a Multielement Doping Strategy. *Inorg Chem* **54**, 3600-3607, (2015).

200   International Technoloy Roadmap for Semiconductor Industry (ITRS) 2014 Edition, Emerging research devices http://www.itrs2.net/ (2014).

201   Balatti, S., Ambrogio, S. & Ielmini, D. Normally-off Logic Based on Resistive Switches-Part II: Logic Circuits. *Ieee T Electron Dev* **62**, 1839-1847, (2015).

202   Balatti, S., Ambrogio, S. & Ielmini, D. Normally-off Logic Based on Resistive Switches-Part I: Logic Gates. *Ieee T Electron Dev* **62**, 1831-1838, (2015).

203   Sacchetto, D. *et al.* Applications of Multi-Terminal Memristive Devices: A Review. *Ieee Circ Syst Mag* **13**, 23-41, (2013).

204   Beck, A., Bednorz, J. G., Gerber, C., Rossel, C. & Widmer, D. Reproducible Switching Effect in Thin Oxide Films for Memory Applications. *Appl Phys Lett* **77**, 139-141, (2000).

205   Messerschmitt, F., Kubicek, M., Schweiger, S. & Rupp, J. L. M. Memristor Kinetics and Diffusion Characteristics for Mixed Anionic-Electronic $SrTiO3-delta$ Bits: The Memristor-Based Cottrell Analysis Connecting Material to Device Performance. *Adv Funct Mater* **24**, 7448-7460, (2014).

206   Wedig, A. *et al.* Nanoscale Cation Motion in TaO_x, HfO_x and TiO_x Memristive Systems. *Nat Nanotechnol* **11**, 67-74, (2016).

207   Schmitt, R. *et al.* Engineering Microstructural Defect Structures for Resistive Switching in $LaFeO_3$ Devices. *to-be-submitted*, (2016).

208   Kura, C., Aoki, Y., Tsuji, E., Habazaki, H. & Martin, M. Fabrication of a Resistive Switching Gallium Oxide Thin Film with a Tailored Gallium Valence State and Oxygen Deficiency by RF Cosputtering Process. *Rsc Adv* **6**, 8964-8970, (2016).

209   Schweiger, S., Kubicek, M., Messerschmitt, F., Murer, C. & Rupp, J. L. A Microdot Multilayer Oxide Device: Let us Tune the Strain-Ionic Transport Interaction. *Acs Nano* **8**, 5032-5048, (2014).

210   Kresse, G. Ab-Initio Molecular-Dynamics for Liquid-Metals. *J Non-Cryst Solids* **193**, 222-229, (1995).

211   Perdew, J. P. *et al.* Restoring the Density-Gradient Expansion for Exchange in Solids and Surfaces. *Phys Rev Lett* **100**, 136406, (2008).

212   Blochl, P. E. Projector Augmented-Wave Method. *Phys Rev B Condens Matter* **50**, 17953-17979, (1994).

213   Kresse, G. & Joubert, D. From Ultrasoft Pseudopotentials to the Projector Augmented-Wave Method. *Phys Rev B* **59**, 1758-1775, (1999).

214   Togo, A., Oba, F. & Tanaka, I. First-principles Calculations of the Ferroelastic Transition between Rutile-type and $CaCl_2$-type SiO_2 at High Pressures. *Phys Rev B* **78**, (2008).

215   Hsieh, C. C., Roy, A., Rai, A., Chang, Y. F. & Banerjee, S. K. Characteristics and Mechanism Study of Cerium Oxide based Random Access Memories. *Appl Phys Lett* **106**, (2015).

216   Younis, A., Zhang, L. P., Chu, D. W. & Li, S. Probing Complementary Memristive Characteristics in Oxide based Memory Device via Non-Conventional Chronoamperometry Approach. *Appl Phys Lett* **108**, 033506, (2016).

217   Crozier, P. A., Wang, R. & Sharma, R. In-situ Environmental TEM Studies of Dynamic Changes in Cerium-based Oxides

Nanoparticles during Redox Processes. *Ultramicroscopy* **108**, 1432-1440, (2008).

218   Usuda, K. *et al.* Strain Relaxation of Strained-Si Layers on SiGe-on-Insulator (SGOI) Structures after Mesa Isolation. *Appl Surf Sci* **224**, 113-116, (2004).

219   Williams, D. B. & Carter, C. B. *Transmission Electron Microscopy: a Textbook for Materials Science*. 2nd edn, (Springer, 2009).

220   Giannici, F. *et al.* Structure and Oxide Ion Conductivity: Local Order, Defect Interactions and Grain Boundary Effects in Acceptor-Doped Ceria. *Chem Mater* **26**, 5994-6006, (2014).

221   Weber, W. H., Hass, K. C. & Mcbride, J. R. Raman-Study of CeO_2 - 2nd-Order Scattering, Lattice-Dynamics, and Particle-Size Effects. *Phys Rev B* **48**, 178-185, (1993).

222   Loudon, R. Raman Effect in Crystals. *Adv Phys* **13**, 423-482, (1964).

223   Suess, M. J. *et al.* Power-Dependent Raman Analysis of Highly Strained Si Nanobridges. *Nano Lett* **14**, 1249-1254, (2014).

224   Narayanan, S., Kalidindi, S. R. & Schadler, L. S. Determination of Unknown Stress States in Silicon Wafers using Microlaser Raman Spectroscopy. *J Appl Phys* **82**, 2595-2602, (1997).

225   Yavo, N. *et al.* Elastic Moduli of Pure and Gadolinium doped Ceria revisited: Sound Velocity Measurements. *Scripta Mater* **123**, 86-89, (2016).

226   Sawa, A. Resistive Switching in Transition Metal Oxides. *Mater Today* **11**, 28-36, (2008).

227   Schweiger, S., Bowman, W. & Rupp, J. L. M. The role of symmetry and preforming in strained heterostructure memristive devices. *to-be-submitted*, (2016).

228   Gao, P. *et al.* In-situ TEM Studies of Oxygen Vacancy Migration for Electrically Induced Resistance Change Effect in cerium oxides. *Micron* **41**, 301-305, (2010).

229   Chueh, W. C. *et al.* Highly Enhanced Concentration and Stability of Reactive Ce^{3+} on Doped CeO_2 Surface Revealed In Operando. *Chem Mater* **24**, 1876-1882, (2012).

230   Skorodumova, N. V., Simak, S. I., Lundqvist, B. I., Abrikosov, I. A. & Johansson, B. Quantum Origin of the Oxygen Storage Capability of Ceria. *Phys Rev Lett* **89**, 166601, (2002).

231   Kubicek, M., Schmitt, R., Messerschmitt, F. & Rupp, J. L. M. Uncovering Two Competing Switching Mechanisms for Epitaxial and Ultrathin Strontium Titanate-Based Resistive Switching Bits. *Acs Nano* **9**, 10737-10748, (2015).

232   Messerschmitt, F., Kubicek, M. & Rupp, J. L. M. How Does Moisture Affect the Physical Property of Memristance for Anionic-Electronic Resistive Switching Memories? *Adv Funct Mater* **25**, 5117-5125, (2015).

233   Yin, Q. N. *et al.* Cathode Bubbles induced by Moisture Electrolysis in TiO_{2-x}-based Resistive Switching Cells. *J Phys D Appl Phys* **49**, (2016).

234   Plonczak, P. *et al.* Tailoring of $La_xSr_{1-x}Co_yFe_{1-y}O_{3-d}$ Nanostructure by Pulsed Laser Deposition. *Adv Funct Mater* **21**, 2764-2775, (2011).

235   Waser, R. *Nanoelectronics and Information Technology : Advanced Electronic Materials and Novel Devices*. 3rd, completely rev. and enlarged edn, (Wiley-VCH, 2012).

236   Kwon, D. H. *et al.* Atomic Structure of Conducting Nanofilaments in TiO_2 Resistive Switching Memory. *Nat Nanotechnol* **5**, 148-153, (2010).

237   Schweiger, S., Pfenninger, R., Bowman, W., Aschauer, U. & Rupp, J. L. M. Designing Strained Interface Heterostructures for Resistive Switching Devices. *To be submitted*, (2016).

238   Yang, J. J. *et al.* The Mechanism of Electroforming of Metal Oxide Memristive Switches. *Nanotechnology* **20**, 215201, (2009).

239   Muraoka, S. *et al.* Fast Switching and Long Retention Fe-O ReRAM and its Switching Mechanism. *2007 Ieee International Electron Devices Meeting, Vols 1 and 2*, 779-782, (2007).

240   Kuegeler, C., Meier, M., Rosezin, R., Gilles, S. & Waser, R. High density 3D memory architecture based on the resistive switching effect. *Solid State Electron* **53**, 1287-1292, (2009).

241   Jeong, H. Y., Lee, J. Y. & Choi, S. Y. Interface-Engineered Amorphous TiO$_2$-Based Resistive Memory Devices. *Adv Funct Mater* **20**, 3912-3917, (2010).

242   Minghao, W., Huaqiang, W., Xinyi, L., Ning, D. & He, Q. in *Proceedings of Technical Program - 2014 International Symposium on VLSI Technology, Systems and Application (VLSI-TSA).* 1-2.

243   Liu, K. C. *et al.* The resistive switching characteristics of a Ti/Gd2O3/Pt RRAM device. *Microelectron Reliab* **50**, 670-673, (2010).

244   Li, Z. W. *et al.* Three-state resistive switching in CoFe2O4/Pb(Zr0.52Ti0.48)O-3/ZnO heterostructure. *Appl Phys Lett* **100**, (2012).

245   Fukusima, M., Ohta, A., Makihara, K. & Miyazaki, S. Characterization of Resistive Switching of Pt/Si-Rich Oxide/TiN System. *Ieice T Electron* **E96c**, 708-713, (2013).

246   Lee, A. R., Bae, Y. C., Baek, G. H., Im, H. S. & Hong, J. P. Multi-level resistive switching observations in asymmetric

Pt/Ta2O5-x/TiOxNy/TiN/Ta2O5-x/Pt multilayer configurations. *Appl Phys Lett* **103**, (2013).

247 Messerschmitt, F., Schmitt, R., Nenning, A. & Rupp, J. L. M. Electrical Probing Techniques for Solid State Resistive Switches: an Electrochemist's Review. *to be submitted*, (2016).

248 Turner, S. *et al.* High resolution mapping of surface reduction in ceria nanoparticles. *Nanoscale* **3**, 3385-3390, (2011).

249 Kim, J. J., Bishop, S. R., Thompson, N. J., Chen, D. & Tuller, H. L. Investigation of Nonstoichiometry in Oxide Thin Films by Simultaneous in Situ Optical Absorption and Chemical Capacitance Measurements: Pr-Doped Ceria, a Case Study. *Chem Mater* **26**, 1374-1379, (2014).

250 Bowman, W. J., Zhu, J., Sharma, R. & Crozier, P. A. Electrical Conductivity and Grain Boundary Composition of Gd-doped and Gd/Pr co-doped Ceria. *Solid State Ionics* **272**, 9-17, (2015).

251 Egerton, R. F. *Electron Energy-loss Spectroscopy in the Electron Microscope*. Third edition. edn, (Springer, 2011).

252 Ganesan, S., Maradudi, A. A. & Oitmaa, J. A Lattice Theory of Morphic Effects in Crystals of Diamond Structure. *Ann Phys-New York* **56**, 556-&, (1970).

253 Abrashev, M. V., Todorov, N. D. & Geshev, J. Raman Spectra of R_2O_3 (R-Rare Earth) Sesquioxides with C-Type Bixbyite Crystal Structure: A Comparative Study. *J Appl Phys* **116**, (2014).

254 Dilawar, N. *et al.* A Raman Spectroscopic Study of C-type Rare Earth Sesquioxides. *Mater Charact* **59**, 462-467, (2008).

255 Schaack, G. & Koningstein, J. A. Phonon and Electronic Raman Spectra of Cubic Rare-Earth Oxides and Isomorphous Yttrium Oxide. *J Opt Soc Am* **60**, 1110-+, (1970).

256 Porto, S. P. S. & Krishnan, R. S. Raman Effect of Corundum. *J Chem Phys* **47**, 1009-1012, (1967).

30 Curriculum Vitae

Publications

1. Coating of glass substrates to prevent alkali ion diffusion into pharmaceutical solutions
Schweiger, S.; Neubauer, C.; Fraser, S.; Klein, T.; Schennach, R.; Reichmann, A.; Gruber-Woelfler, H.
Surface & Coatings Technology, 258, 1249 (2014)

2. A Micro-Dot Multilayer Oxide Device: Let's Tune the Strain-Ionic Transport Interaction
Schweiger, S.; Kubicek, M.; Messerschmitt, F.; Murer, C.; Rupp, J.L.M.
ACS Nano, 8, 5, 5032 (2014)

3. Memristor Kinetics and Diffusion Characteristics for Mixed Anionic-Electronic $SrTiO_{3-\delta}$: The Memristor-based Cottrell Analysis Connecting Material to Device Performance
Messerschmitt, F.; Kubicek, M.; Schweiger S.; Rupp, J.L.M.
Advanced Functional Materials, 24, 47, 7448 (2014)

4. The Effect of Mechanical Twisting on Oxygen Ionic Transport in Solid State Energy Conversion Membranes
Shi, Y.; Bork, A.H.; Schweiger, S.; Rupp, J.L.M.
Nature Materials, 14, 721 (2015)

5. Na^+-doped and Al_2O_3-stabilized CuO Oxygen Carriers for Chemical Looping Combustion and Chemical Looping with Oxygen Uncoupling
Imtiaz, Q.; Abdala, P.M.; Kierzkowska, A.; van Beek, W.; Schweiger, S.; Rupp, J.L.M.; Müller, C.R.
Physical Chemistry Chemical Physics, 18, 17, 12278-12288 (2016)

6. The role of associated defects in oxygen ion conduction and surface exchange reaction for high structural quality samaria doped ceria thin films as catalytic coatings
Yang, N.; Shi, Y.; Schweiger, S.; Strelcov, E.; Belianinov, A.; Foglietti, V.; Balestrino, G.; Kalinin, S.V.; Rupp, J.L.M.; Aruta C.
ACS Appl. Mater. Interfaces, 8, 23, 14613–14621 (2016)

7. Designing Strained Ionic Heterostructures for Resistive Switching Devices
Schweiger, S.; Pfenninger, R.; Bowman, W.; Aschauer, U.; Rupp, J.L.M.
Under Review at Advanced Materials (2016)

8. Influence of Electrode Symmetry and Electroforming on Resistive Switching of Structured Memristive Devices
Schweiger, S.; Bowman, W.; Crozier, P.; Rupp, J.L.M.
To be submitted to ACS Nano (2016)

9. Tensile Strain at Ambient Conditions in Multilayered Oxides: new Material Design Strategies for Memristive Devices
Bowman, W.; Schweiger, S.; Crozier, P.; Rupp, J.L.M.
To be submitted (2016)

10. Engineering Strain for Future Multilayer Architectures in new Resistive Switching Memory and Computing Devices – A review
Schweiger, S.; Rupp, J.L.M.
Review paper, to be submitted to ACS Nano (2016)

Book Chapters

1. Future Emerging Technologies based on MetOx Interfaces:
    MeO-Strain Interface Memristors
    Schweiger, S.; Rupp, J.L.M.
    Metal Oxide-based Thin Film Structures: Formation,
    Characterization and Application of Interface-based Phenomena
    edited by Nini Pryds for Elsevier Science & Technology Books,
    2017.

Patents

Patent WO2014170023: "Strained Multilayer Resistive-switching
Memory Elements" 23rd October 2014
Sebastian Schweiger, Felix Messerschmitt, Jennifer L. M. Rupp
The patent won the Spark Award 2014

Organization of events

Main organizer of the three days international workshop "Raman
Microscopy - A strong tool for chemical imaging." with over 70
participants. This event was organized solely by PhD students. Funding
was secured independently by the Doctoral students program of the
Schweizerische Universitätskonferenz (SUK).

Conference contributions

Schweiger, S.; Bowman W.J.; Aschauer, U.; Rupp J.L.M.
Strained Oxide Heterostructures for Modulating Memristance
Materials Research Society (MRS) Spring Meeting
Phoenix, USA   04/2016
Oral presentation

Schweiger, S.; Aschauer, U.; Pfenninger, R.; Rupp, J.L.M.
Resistive Switching Tuned by Interfacial Strain in Ionic Heterostructure Microdots
MRS Fall Meeting 2015
Boston, MA, USA   12/2015
Oral presentation

Schweiger S, Aschauer S, Pfenninger R, Rupp J.L.M.
Strained Oxide Heterostructures for Modulating Memristance
Advances in ReRAM: Materials & Interfaces,
Chania, Crete, Greece   10/2015
Oral presentation

Schweiger, S.; Aschauer, U.; Pfenninger, R.; Rupp, J.L.M.
Strained Heterolayers as Resistive Switching Oxide: Materials and Devices
Solid State Ionics 20
Keystone, CO, USA   06/2015
Oral presentation

Schweiger, S.; Kubicek, M.; Messerschmitt, F.; Rupp, J.L.M.
New Strained Memristive Oxide Switch Concepts: Materials and Devices Memristor Kinetics and Diffusion
IEEE Swiss CAS/ED workshop 2014, Zurich, Switzerland   11/2014
Poster presentation

Schweiger, S.; Kubicek, M.; Messerschmitt, F.; Rupp, J.L.M.
New Strained Memristor Devices
Industry Day 2014, Zurich, Switzerland   08/2014
Poster presentation

Schweiger, S.; Kubicek, M.; Messerschmitt, F.; Rupp, J.L.M.
New Strained Memristive Oxide Switch Concepts: Materials and Devices
Gordon Research Conference, Solid State Studies in Ceramics
Mt. Holyoke, MA, USA   07/2014
Poster presentation

Schweiger, S.; Kubicek, M.; Rupp, J.L.M.
Tuning the Ionic Conductivity of Er_2O_3-$Gd_{0.1}Ce_{0.9}O_{2-x}$ Multilayer Dot Micro-Devices by Lattice Strain: Implications for Fabrication and Oxide Near Order-Transport Interaction
E-MRS Spring Meeting
Lille, France   05/2014
Oral presentation

Schweiger, S.; Kubicek, M.; Rupp, J.L.M.
New Strained Memristive Oxide Switch Concepts: Materials and Devices
E-MRS Spring Meeting
Lille, France   05/2014
Oral presentation

Supervised students

Andre Schmidt
Electrical characterization of strained multilayer metal oxide thin films

Master's Thesis   11/2014

Reto Pfenninger
 Strained Metal Oxide Heterostructures for Resistive Switching Microdevices

Master's Thesis   09/2014

Christoph Murer
Growth and characterization of multilayered oxide structures for resistive switching applications

Master's Project 04/2014

Thomas Geldmacher
Epitaxial Growth of Multilayered Ceramic Films for Applications in Memristor-Type Storage Devices

Bachelor's Thesis   05/2013

31 Financial Support